



University  
of Glasgow

Maxwell, Graeme D. (1990) *Optical waveguide fabrication in silica using flame hydrolysis*. PhD thesis.

<http://theses.gla.ac.uk/5637/>

Copyright and moral rights for this thesis are retained by the author

A copy can be downloaded for personal non-commercial research or study, without prior permission or charge

This thesis cannot be reproduced or quoted extensively from without first obtaining permission in writing from the Author

The content must not be changed in any way or sold commercially in any format or medium without the formal permission of the Author

When referring to this work, full bibliographic details including the author, title, awarding institution and date of the thesis must be given

**Optical Waveguide Fabrication In Silica**

**Using Flame Hydrolysis**

**A thesis submitted for the degree of  
Doctor Of Philosophy in the Faculty  
of Engineering in the University Of  
Glasgow**

**by**

**Graeme D. Maxwell**

**February 1990**

**© Graeme D. Maxwell**

**(i)**

## IMAGING SERVICES NORTH

Boston Spa, Wetherby

West Yorkshire, LS23 7BQ

[www.bl.uk](http://www.bl.uk)

**PAGE NUMBERING AS  
ORIGINAL**



## **IMAGING SERVICES NORTH**

Boston Spa, Wetherby  
West Yorkshire, LS23 7BQ  
[www.bl.uk](http://www.bl.uk)

**BEST COPY AVAILABLE.**

**VARIABLE PRINT QUALITY**

To my father, who wondered why it was taking so long....

## ACKNOWLEDGEMENTS

I would like to acknowledge the help and assistance of all of those people who contributed (some by their presence, some by their absence) to the completion of this project, some of whom are mentioned below.

Firstly I would like to thank my supervisor, Dr. John Arnold for the interest he has shown in this project and for the help and encouragement he has given throughout my time at Glasgow.

For those who helped in the design, construction and assembly of the various pieces of equipment required in this work, I would like to acknowledge and thank; Roy Turnbull for his continual assistance in assembling and running the deposition kit; and, Harry Anderson and Jim Kelly in the workshop for building all of the bits needed.

Tom Watson and Lois Hobbs are to be thanked for their help in lithography and clean room practice. Thanks are also due to Dave Gourlay for his help and artistic flair with the electron microscope, and Kas Piechowiak for polishing the waveguides when they finally arrived.

Ray Hutchins gave a lot of help, especially early on when it was needed. Ken Thomas made the gratings and explained the theory. Chris Wilkinson and Kadhair Al-Hemyari are to be thanked for their discussions and help on loss measurement.

Also due a lot of thanks is Jim Ainslie, my supervisor at BTRL. He gave a lot of practical advice and encouragement all of the way through the project. Steve Hubbard, also at BTRL helped with measurements later on in the project when time was running out.

One should also acknowledge the financial assistance of the Science and Engineering Research Council, British Telecom for the CASE award sponsorship.

There are others who contributed with good natured banter (nay abuse), wine and thorny questions who shall remain (thankfully) anonymous.

And lastly but by no means least, I would like to thank my wife Clare for the typing, encouragement and hot dinners that were given free of charge (nearly).

## SUMMARY

This thesis is concerned with the fabrication, assessment and application of doped silica waveguides using Flame Hydrolysis Deposition.

Deposition apparatus has been designed and constructed. This equipment consists of a gas supply assembly, a bubbler cabinet, a deposition box and a chemical scrubber.

An optimum sintering regime for the low density silica soot has been established consisting of 60 minutes at 1250° C. This regime is dependent on the levels of P<sub>2</sub>O<sub>5</sub>, GeO<sub>2</sub> and/or TiO<sub>2</sub> doping in the silica host.

Independent control of layer thickness and index is achieved. Refractive index can be varied by changing the doping levels, and thickness, by increasing the number of traversals of the hydrolysing flame.

Film homogeneity in terms of layer thickness was found to be difficult to control and up to 30% variation in thickness was obtained in some samples. Thermophoretic effects were shown to play an important part in the deposition process.

Titanium and phosphorus doped films were found to suffer film degradation and aging. This led to the formation of titanium rich crystals and crystal agglomerates which produced Rayleigh/ Mie scatter in the sintered films. No such problem was found with Germanium, and all films were subsequently fabricated using Germanium and Phosphorus.

No out-of-plane scatter was observed in the sintered films.

Ridge waveguides were fabricated using lithography and Reactive Ion Etching in a CHF<sub>3</sub> plasma, giving waveguides with smooth side walls.

Loss assessment was carried out using two techniques, both of which were non-destructive. One involved a video camera to scan across the waveguide and detect the out-of-plane scatter. This technique was sensitive to scattering centres and was less accurate for short lengths of guide. Loss figure varied from 0.2 to over

5 dB/cm depending on the scan length. The second technique involved turning the waveguide into a Fabry-Perot resonator, by coating the end faces of the waveguide. Temperature induced cycles in the output intensity could be used to obtain the waveguide attenuation. This technique was sensitive to the facet angles of the guides which could contribute significantly to the loss measured. Such resonances were obtained in only one sample and gave a loss figure of over 9 dB/cm which is considered unreliable.

Films were doped with both  $\text{Nd}^{3+}$  and  $\text{Er}^{3+}$  using a solution doping technique and fluorescence spectra were obtained for both. Increased scatter was observed in the planar films with such doping.

Holographic gratings were fabricated on planar waveguides with a view to their incorporation as feedback elements in a laser structure.

Second Harmonic Generation was observed for the first time in planar rib waveguide structures doped with Phosphorus and Germanium. In a 'seeding' experiment where 1064nm radiation was launched at the same time as a second harmonic 'seed', a two-hundred fold increase was observed in generated second harmonic signal over the background level.

# TABLE OF CONTENTS

## ACKNOWLEDGEMENTS

## SUMMARY

## CHAPTER 1 INTRODUCTION

1.1 PERSPECTIVE .....	1
1.2 SYNOPSIS OF THESIS .....	1

## CHAPTER 2 FABRICATION TECHNIQUES - DESCRIPTION AND APPRAISAL

2.1 DESCRIPTION OF FABRICATION TECHNIQUES .....	3
2.1.1 Chemical Vapour Deposition .....	4
2.1.2 Electron-Beam Vapour Deposition .....	6
2.1.3 RF Sputtering .....	6
2.1.4 Thermal Oxidation .....	6
2.1.5 Sol-gel Processes .....	7
2.1.6 Thermal Nitridation .....	7
2.1.7 Ion Implantation .....	8
2.1.8 Flame Hydrolysis Deposition .....	8
2.2 MERITS AND DEMERITS .....	9
2.3 FLAME HYDROLYSIS DEPOSITION OF SILICA:	
APPARATUS DESIGN AND CONSTRUCTION .....	11
2.3.1 Gas Supply Assembly .....	12
2.3.2 Bubbler Cabinet .....	13
2.3.3 Deposition Chamber .....	16
2.3.4 Scrubber System .....	19
2.4 REFERENCES .....	20

## CHAPTER 3 THEORY AND PRACTICE OF SINTERING

3.1 THEORETICAL ASPECTS OF SINTERING .....	23
3.1.1 Atmospheric Effects .....	30
3.1.2 Collapse of Closed Pores .....	30
3.2 EXPERIMENTAL VERIFICATION .....	32
3.2.1 Surface Tension and Viscosity Effects .....	32

3.2.2	Effect of Atmospheres on Pore Closure	33
3.3	CONCLUSIONS	34
3.4	REFERENCES	35
CHAPTER 4 FLAME, PARTICLE AND CHEMICAL CONSIDERATIONS		
4.1	PHENOMENON OF PARTICLE FORMATION AND GROWTH IN THE FLAME	36
4.2	STRUCTURE OF UNSINTERED MATERIAL	37
4.3	CHEMICAL AND PHASE CONSIDERATIONS	40
4.3.1	SiO <sub>2</sub> / P <sub>2</sub> O <sub>5</sub>	41
4.3.2	SiO <sub>2</sub> / TiO <sub>2</sub>	43
4.3.3	SiO <sub>2</sub> / GeO <sub>2</sub>	44
4.4	CONCLUSIONS	45
4.5	REFERENCES	46
CHAPTER 5 FILM FABRICATION : ASSESSMENT AND APPRAISAL		
5.1	SUBSTRATE PREPARATION	48
5.2	DEPOSITION PROCEDURE	49
5.3	ASSESSMENT OF DEPOSITED MATERIAL: PROBLEMS AND SOLUTIONS	51
5.4	FURNACE CONSIDERATIONS	56
5.5	LAYER THICKNESS CHARACTERISATION	60
5.6	ASSESSMENT OF FUSING AND/ OR FUSED MATERIAL	63
5.6.1	The System SiO <sub>2</sub> / P <sub>2</sub> O <sub>5</sub> / TiO <sub>2</sub>	65
5.6.2	The System SiO <sub>2</sub> / P <sub>2</sub> O <sub>5</sub> / GeO <sub>2</sub>	72
5.7	EFFECT OF FURNACE ATMOSPHERES ON FUSING	73
5.8	CONCLUSIONS	77
5.9	REFERENCES	78
CHAPTER 6 CHARACTERISATION OF PLANAR OPTICAL PROPERTIES		
6.1	PLANAR WAVEGUIDING THEORY	80
6.1.1	Description Of The Problem And Basic Requirements	80
6.1.2	Derivation Of The Transverse Resonance Condition	83
6.2	THE PRISM COUPLER	86
6.2.1	Calculation Of Thin Film Parameters	88
6.3	PRISM COUPLING PRACTICE	89
6.3.1	Prism Design	90
6.3.2	Mode lines	92

6.3.3	Measurement Procedure	93
6.3.4	Accuracy Of Results	93
6.4	EXPERIMENTAL RESULTS	94
6.4.1	Sample Result	94
6.4.2	Comparison Of Film Index Results	97
6.4.3	Estimation Of Optical Loss	98
6.5	CONCLUSIONS	101
6.6	REFERENCES	102

## CHAPTER 7 RIDGE WAVEGUIDE FABRICATION AND ASSESSMENT

7.1	RIDGE WAVEGUIDE THEORY	104
7.1.1	Effective Index Method	105
7.2	PHOTOLITHOGRAPHY	107
7.2.1	Basic Concepts	107
7.2.2	Photolithographic Practice	110
7.3	REACTIVE ION ETCHING	113
7.4	LOSS MEASUREMENT	118
7.4.1	Video Camera Technique	119
7.4.2	Fabry-Perot Cavity Resonance Technique	125
7.4.2(1)	Derivation Of The Expression For Loss	125
7.4.2(2)	Effect of Non-parallel Facets	126
7.4.2(3)	Experimental Arrangement	128
7.4.2(4)	Results	128
7.4.2(5)	Discussion Of Results	130
7.5	CONCLUSIONS	131
7.6	APPENDIX A	133
7.7	REFERENCES	135

## CHAPTER 8 FILM DEVELOPMENT AND APPLICATIONS

8.1	DOPING OF PLANAR SILICA FILMS	137
8.1.1	Doping Method And Results	139
8.1.2	Discussion Of Results	143
8.2	HOLOGRAPHIC GRATING FABRICATION	144
8.2.1	Grating Couplers - Basic Theory	145
8.2.2	Fabrication Of Grating Couplers	146
8.2.3	Assessment Of Gratings	149
8.3	SECOND HARMONIC GENERATION (SHG) IN $\text{GeO}_2/\text{P}_2\text{O}_5$ WAVEGUIDES	151

8.3.1	Phenomenological Model of SHG in Doped Silica	....152
8.3.2	Method And Results Of SHG In Planar Ridge Waveguides	
8.3.2(1)	Waveguide Fabrication	.....154
8.3.2(2)	Experimental Arrangement for SHG	.....155
8.3.2(3)	Experimental Results	.....157
8.3.2(4)	Discussion Of Results	.....159
8.4	REFERENCES	.....161
CHAPTER 9 CONCLUSIONS AND FUTURE WORK		
9.1	CONCLUSIONS	.....163
9.2	MATERIAL ASPECTS FOR FUTURE WORK	.....163
9.3	OPTICAL ASPECTS FOR FUTURE STUDY	.....164

## CHAPTER 1    INTRODUCTION

### 1.1    PERSPECTIVE

In 1851, John Tyndall, as part of a lecture demonstration at the Royal Institution, 'piped' light down a jet of water and prophesied that one day this phenomenon would prove useful in communications. It has taken over a hundred years for technology to provide a means of fabricating suitable material in a suitable form to fulfill his prophesy. The material is fused silica, and the suitable form is a fibre. Such optical fibres provide the means by which optical signals can be transported over very great distances. However, in order to exploit the full potential of optical communications, there is a need for systems which are capable of optically processing the optical information. Such systems require 'optical chips' in which the generation, processing and detection of optical signals are performed. This field has become known generically as Integrated Optics.

Just as there was a need for a suitable material in fibre form for optical transmission, so too there is a need to provide suitable materials in the planar form required for optical circuits. There are a number of technologies available to fabricate suitable materials, and it is with a study of one such technology, namely Flame Hydrolysis, that this thesis is concerned.

### 1.2    SYNOPSIS OF THIS THESIS

This thesis describes the fabrication and application of doped silica films. The technique used for the film fabrication is Flame Hydrolysis Deposition. This technique will be described in chapter 2, where it will be compared and contrasted with competing technologies.

In the process of fabricating the waveguides (passive or active), a sintering stage is required. Chapter 3 will describe the theory involved in this process and will discuss the experimental verification that has been carried out by other authors.

Chapter 4 considers the formation and structure of the un-sintered material and will go on to discuss the structural relationships between the dopants used and the silica host glass in terms of their phase diagrams.

The practicalities of film fabrication are described in chapter 5. Here the methods adopted for deposition are presented, and the techniques used to assess the films are outlined. This assessment covers non-waveguiding aspects; that is it is concerned with producing a fully sintered, inclusion free layer of material.

Waveguiding aspects of the planar films are investigated in chapter 6, where the

prism coupler is used to measure the film index and thickness. Loss assessment of the planar films is also attempted.

In chapter 7 the method and results for ridge waveguide fabrication are described. This chapter also details optical loss assessment in the ridge waveguide structures.

Chapter 8 film development and application. Here one is considering doping of the films with rare-earth species to produce active waveguides. The goal of such work ultimately being the fabrication of a laser structure. As a further step towards such a goal holographic gratings for use as feedback elements are investigated, and results of grating fabrication are presented. The final part of chapter 8 looks at the novel phenomenon of second harmonic generation which had been observed in silica fibres but not previously seen in ridge waveguide structures.

The final chapter discusses areas where the author feels it would be profitable and in some cases essential to carry out future work.

The following section is concerned with a brief description of the main techniques used to fabricate silica based films suitable for integrated optics. The techniques discussed deal with the deposition of a film on a suitable substrate, as well as the modification of the substrate surface itself to produce waveguiding films.

It is in no way intended to include every technique available, merely to outline the more common techniques which have provided the main results published in the literature.

Each technique will be briefly described and in section 2.2 an attempt will be made to compare each deposition system, outlining the advantages and disadvantages.

The technique of ion exchange in multicomponent silicate glasses is not included, for two main reasons. First, for waveguide applications, one is limited to the diffusion properties in the multicomponent glass and subsequent processing is limited to those which will not cause unwanted diffusion; and second, multicomponent glasses have lower melting points than silica, because of which the use of fusion splicing to fibres is unavailable. This means that splicing of such films to fibres must be done using techniques such as epoxy bonding which is less durable and more labour intensive.

Following such an appraisal, the deposition technique of Flame Hydrolysis will be described and will include details of the equipment designed and constructed by the author to implement film fabrication.

### 2.1 DESCRIPTION OF FABRICATION TECHNIQUES

There are a number of techniques available for the production of silica films suitable as optical waveguides. These techniques generally can be separated into: chemical methods, such as Chemical Vapour Deposition (CVD), Sol-gel, oxidation and nitridation; physical methods, such as sputtering and ion implantation; or they may be a combination of the two, such as Thermal Oxidation and Flame Hydrolysis where a heterogeneous chemical reaction is followed by a physical deposition.

The chemical techniques, such as Low pressure Chemical Vapour Deposition (LPCVD)<sup>1</sup> and Plasma Enhanced Chemical Vapour Deposition (PECVD)<sup>2</sup> are, essentially, one-step processes in which the layer of material deposited needs no further fabrication stages to form a planar low loss film. In these processes, the initial reagents are transported as vapours to a deposition chamber. Here they undergo a chemical reaction on the substrates used. The reaction can be initiated using temperature, plasma and a host of other techniques. The means used to

promote reaction will depend on the chemistry involved in the reaction. These techniques were developed initially for passivation of electronic circuits<sup>3</sup>, so they are as a result, more mature. The physical techniques such as Electron Beam Vapour Deposition<sup>4</sup>, R.F.Sputtering<sup>5</sup> and Ion Implantation<sup>6</sup> are also generally one step affairs. Other techniques such as Oxidation<sup>7</sup>, Flame Hydrolysis<sup>8</sup> and Sol-gel<sup>9</sup> are more recent, initially having been developed for fibre optic fabrication and have been modified to suit the planar geometries involved.

The techniques used to fabricate the doped silica are of seven main types –

- (1) Chemical Vapour Deposition – including variations such as LPCVD, and PECVD
- (2) Electron-Beam Vapour Deposition
- (3) Radio Frequency Sputtering
- (4) Thermal Oxidation
- (5) Sol-Gel Process
- (6) Nitridation
- (7) Ion Implantation
- (8) Flame Hydrolysis

### 2.1.1 CHEMICAL VAPOUR DEPOSITION (CVD)

This technique involves the transport of the chemical vapours required to a suitable deposition chamber, where *heterogeneous* chemical reactions are initiated on the substrates. Deposition is limited by the transport of the vapours to the reaction zone and the diffusion of reagents and reaction products across the boundary layer above the substrates. All such techniques have the advantage of added purification of the reagents as a carrier gas transports the necessary vapours and contaminants present in the reagents, such as Fe which causes absorption, are generally much less volatile (see Figure 2.1). The initiation of the reactions can be accomplished in a number of ways, including the use of temperature, the use of the substrate itself, of electron beams etc. There are a number of general references to CVD <sup>10,11</sup> which provide more detailed information. In general such techniques allow independent control of refractive index by varying the compositional flow rates of the reagents, and of thickness by varying the deposition time.

The CVD technique encompasses a number of deposition configurations and those that apply to the task in hand will be mentioned. It should be pointed out that those techniques in which the reactions do not take place on the substrate, but in the gas phase above the substrate have not been included in the CVD section, although strictly speaking they are still CVD systems.

Verbeek et al<sup>1</sup> have used Low Pressure CVD (LPCVD) to fabricate films of phosphorus doped silica. In this technique, the pressures in the reaction chamber are typically 30 to 250 Pa<sup>7</sup>, hence the term "low pressure". The benefit of this technique lies in the fact that conventional silicon integrated circuit technology is used and is therefore capable of mass production. Furthermore, the use of low pressures reduces contamination due to particles in the air in the deposition chamber.

Another example of a LPCVD technique is the pyrolytic oxidation of Arsine with silane to form Arsenic Oxide doped silica<sup>12</sup>. Such films have application in the semiconductor industry as passivation layers and have recently found application as optical waveguides<sup>13</sup>. Such films have also been investigated by the author and reference will be made to this work in later chapters where such films are compared with those produced by the Flame Hydrolysis technique.

A further refinement to vapour deposition is used by Nourshargh<sup>2</sup> et al in which a plasma is used to activate the chemical reactions. This technique also offers the possibility of doping of active materials by introducing such materials into the plasma. This too is a low pressure technique but is generally referred to as "plasma enhanced CVD" (PECVD). This technique has the advantage of fabricating films where the substrate temperature is very low – room temperature deposition having been reported<sup>3</sup>. This is an advantage for deposition on to III-V semiconductor materials or Multiple Quantum Wells (MQW's) where high temperatures are undesirable as substrate degradation and decomposition would occur.

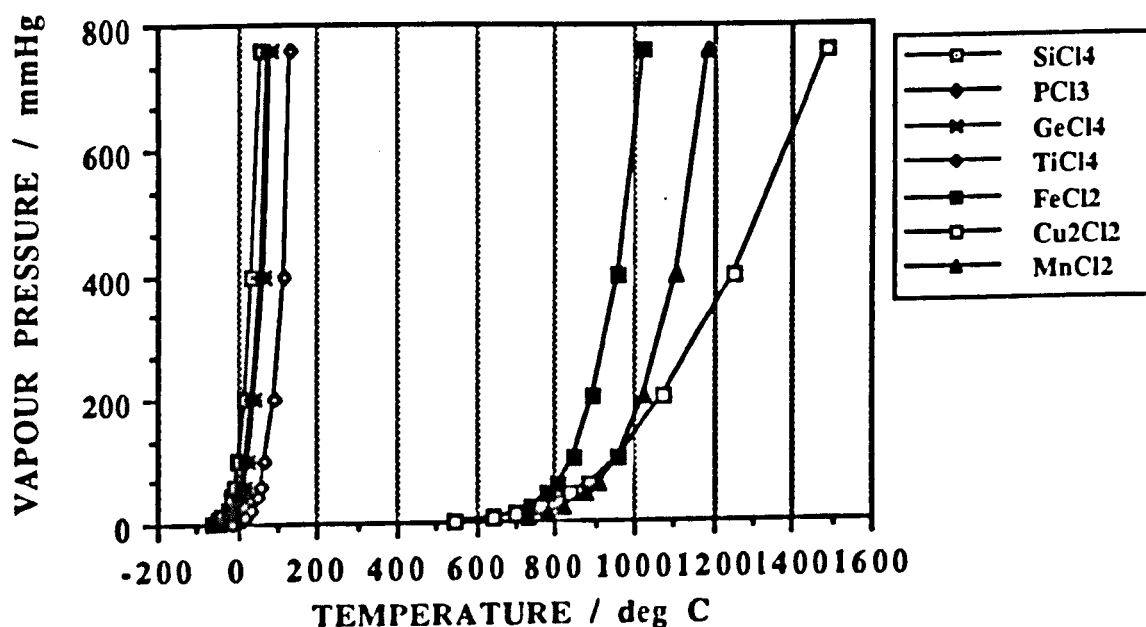


Figure 2.1 Comparison of vapour pressures of various chlorides.

## 2.1.2 ELECTRON-BEAM VAPOUR DEPOSITION

An alternative technique is used by Imoto et al<sup>4</sup> in which Electron-Beam Vapour Deposition is used to fabricate the core region consisting of titanium doped silica. The technique offers good control of layer thickness and refractive index (< 0.3% and < 0.02 % respectively).

In this type of deposition configuration<sup>32</sup>, a resistive heater provides a source of electrons. Magnetic fields are used to guide and focus the electrons, resulting in an electron beam. The beam is directed into a crucible containing the material to be evaporated. Absorption of the electron energy results in material vaporisation which then condenses on the substrate placed above the crucible. This type of system operates at low pressure which reduces particle contamination. Furthermore this type of deposition system is useful for involatile species such as SiO<sub>2</sub> by virtue of the very high temperatures which can be generated by the electron-beam.

## 2.1.3 RADIO FREQUENCY (RF) SPUTTERING

Radio frequency sputtering<sup>15</sup> involves the acceleration of ions such as Ar<sup>+</sup> through a potential gradient. These energetic ions bombard a suitable target of the material to be deposited. Surface atoms of the target are ejected by the transfer of momentum from the ions and are deposited on to a suitably positioned substrate.

Huang et al<sup>5</sup> used this technique in preference to vapour deposition methods when they studied the effect of increasing the GeO<sub>2</sub> concentration in SiO<sub>2</sub> on the refractive index of the resulting film. More recently, Jerominek et al<sup>17</sup> have used this technique to deposit semiconductor microcrystallites into Corning 7059 glass. As for E-beam deposition, this technique does not depend on the volatility of the reagents and as such is suitable for most materials.

## 2.1.4 THERMAL OXIDATION

This technique is in essence a CVD technique. The vapours are transported using a carrier gas as before into the deposition chamber. The chamber used is a furnace in which the chemicals are thermally oxidised. However the homogenous reaction takes place in the gas phase and oxidised particles deposit on the heated substrates. This process then requires a second stage to consolidate the oxide particles into a transparent film. This technique is in contrast with the oxidation of a silicon substrate to form silica, and care should be taken not to confuse the two.

Izawa et al<sup>7</sup> developed this technique which is similar to that used for VAD fibre fabrication<sup>16</sup>. The deposition technique requires a thermal gradient inside the deposition furnace in order for deposition to take place<sup>17</sup>. However a relatively lossy film is produced, apparently due to scattering in the deposited glass layer.

### 2.1.5 SOL-GEL PROCESSES

It is possible to produce silica glass using solutions of suitable silicon compounds, as for example silicon tetra-methoxide  $\text{Si}(\text{OCH}_3)_4$ , or silicon tetra-ethoxide  $\text{Si}(\text{OEt}_3)_4$ , which are hydrolysed and converted to a homogeneous solution or sol, (which is essentially a colloid of silica particles) with an appropriate solvent such as methanol. This sol is then converted to a gel as the hydrolysis reaction proceeds and the colloid particles join to produce an interconnected network. Once gelling is complete, the solvent can be evaporated off to leave a 'dry gel' at which point a porous 'blank' is obtained. This can then be sintered to produce the transparent silica.

Optical fibres formed in this way used a silica core formed from a sol and a lower index cladding deposited by standard CVD techniques<sup>18</sup>.

Planar optical waveguides have been formed by partially sintering the resulting dry gels. The refractive index of the glass is a function of the porosity or pore size, and as long as the pores are sufficiently small to avoid scattering the light used, then a local increase in the sintering of the preform will result in a refractive index increase. This can then be used as an optical waveguide. Ramaswamy et al<sup>9</sup> have used this technique to produce waveguides, although no loss figures have been quoted. They have also outlined a method of diffusion of dopant species into the porous glass to produce the desired index increment. Doping of active materials into sol-gels has been carried out and seems to show considerable promise<sup>19</sup>.

### 2.1.6 THERMAL NITRIDATION

This technique uses the fact that amorphous silica is capable of dissolving significant amounts of nitrogen, and since silicon nitride  $\text{Si}_3\text{N}_4$  has a refractive index of 2.00, incorporating even a few wt% of nitrogen in the silica can produce a waveguide.

Using this method, Zelmon et al<sup>20</sup> produced waveguides in a silica layer formed on a silicon substrate on whose surface an oxide layer had been grown. A number of wafers were exposed to ammonia in a furnace at 1,000 °C for times

ranging from 24 hours to ten days. Reduction of waveguide loss between samples was reported with increasing nitridation time and a loss of 0.06 dB/cm was quoted for an exposure time of eight days. The reason for this relationship was attributed to slight increases in the guiding layer thickness which reduced coupling into the silicon substrate.

### 2.1.7 ION IMPLANTATION

The process of ion implantation involves the acceleration of ionised atoms to sufficiently high speeds to enable them to penetrate beyond the surface of a suitable target. The ion source is generally from a gas of the required species which is converted into a plasma. An analysing magnet selects the desired ion species which are then accelerated to the target<sup>11</sup>.

The first report of such a technique being used to provide waveguides was by Schineller et al<sup>21</sup>, in 1967. Here, protons were used to increase the refractive index of fused silica. Light guidance was observed, but no loss figures were quoted.

Standley et al<sup>22</sup>, studied the optical effects induced after bombardment using a range of different ion sources. They found lithium ions gave the best results and quoted a loss of 0.2 dB/cm in a sample which had been annealed after bombardment.

Naik<sup>6</sup>, appears to be the most recent worker in this technique (1983). Nitrogen ions ( $N^+$ ), are used as the ion source and fused silica is the target. The resulting silicon oxy-nitride film has a higher refractive index than the silica and acts as a waveguide. Annealing the implanted sample reduced the defects produced by the technique and resulted in a film having loss of 0.1 dB/cm at 632 nm.

### 2.1.8 FLAME HYDROLYSIS DEPOSITION

The description of this technique and its application will be the subject of the rest of the chapter. However, a brief description will be included here for completeness. Kawachi et al<sup>8</sup> were first to report on the use of flame hydrolysis to produce planar films of titanium dioxide doped silica. It is, as are most of these techniques, basically a CVD system in which the required reagents are transported to the deposition chamber using a carrier gas. Here, an oxy-hydrogen flame is used to hydrolyse the metal chlorides to provide the desired oxides. The reaction takes place in the gas phase, and solid particles of material called "soot" are deposited on the substrates in the chamber. Once the required amount of material has been deposited, the coated substrates are placed in a sintering furnace to consolidate the

"soot" into a transparent film. Consolidation using CO<sub>2</sub> laser processing has also been reported<sup>23</sup>.

Layer thickness is controlled by varying the rate at which the torch traverses across the substrates and by the number of times such traversal takes place. Refractive index can be controlled by varying the carrier gas flow through the dopants used. A number of workers have used this technique<sup>24</sup> to fabricate a range of passive devices.

## 2.2 MERITS AND DEMERITS

In order to assess the relative merits and demerits of the techniques it is necessary to have particular criteria which can be used as a measure of the worthiness of a particular system. The most important criterion is the production of low loss optical films. However, equally important are film homogeneity in terms of thickness and refractive index, as well as repeatability of results. Furthermore, a reasonably fast technique which offers flexibility in film type is required if the process is to be a commercial reality. It should also be kept in mind that planar optical circuits will mainly be used in telecommunications applications and as such, film thickness and refractive index should be tailored to match typical values found in fibres. In this way field overlap between fibre and film can be optimised, typical values for a single mode fibre being 8 $\mu$ m core diameter with a core refractive index lying between 1.46 and 1.48. Once these criteria are satisfied we can then consider the systems in terms of flexibility of dopant materials used, more specifically in the doping of active materials into the silica. Finally, the most suitable system is one which can realise selective doping of both active and passive materials onto a single substrate and in this way realise true integrated optics.

Comparison of the techniques using the criteria outlined poses rather a problem since much of the necessary information has not yet been published, due in part to the recent nature of the techniques. Also, the published information is in such a form as to make comparisons difficult; for example, measurement of loss in etched waveguides cannot be directly compared with measured loss in the slab waveguide since the loss in an etched waveguide depends on parameters such as etch quality and waveguide type. However, some techniques can be shown to be less suitable than others in fulfilling the criteria already outlined.

The sol-gel process has some inherent drawbacks which make it less attractive. The gels require slow drying to avoid cracking<sup>25</sup>, often of the order of several days. This process often leaves adsorbed hydrocarbon residues and water in the porous preform and during the sintering stages can produce contamination, and

often the gel can crack<sup>26</sup>. Supercritical drying<sup>27</sup> can dramatically reduce the drying time but the problem of organic residues is not totally eliminated.

Furthermore, this technique yields bulk material. Control over waveguide dimensions would therefore have to come at the later stage of processing such as local heating or diffusion. The accuracy with which such control can be exercised has yet to be demonstrated.

All of the techniques offer reasonably low loss films. Loss in the slab waveguides are generally less than 0.3 dB/cm<sup>4</sup> and loss in etched waveguides range from 6.4 dB/cm<sup>7</sup> to 0.05 dB/cm<sup>2</sup> although the norm is of the order of 0.1 dB/cm<sup>8</sup>.

Insufficient information is available for a comparison of homogeneity of film thicknesses and refractive indices. Imoto et al<sup>4</sup> is one of the few references to quote figures, giving 0.3 % deviation in film thickness and 0.02 % deviation in refractive index using electron-beam CVD. Aarnio<sup>28</sup> chose LPCVD over PECVD as it gave more uniform layers but no specific information was mentioned. However, generally speaking, the standard CVD techniques produce thin films (<5 $\mu$ m) having relatively high refractive indices (1.5+). This is also true of the nitridation technique and ion implantation.

All of the deposition techniques have realistic deposition times, generally of the order of minutes to a few hours, with the exception of the nitridation technique<sup>20</sup> - several days are quoted as required to produce a film. This makes the technique less suitable for commercial application. Furthermore, the technique is restricted to only one film type.

When it comes to doping to achieve nonlinear optical properties, the range of suitable techniques narrows. The general CVD techniques - LPCVD and straight CVD as well as ion implantation do not readily lend themselves to the fabrication of active materials, by virtue of the non-volatile nature of suitable dopants such as the rare-earth elements<sup>29</sup>. Ion implantation can implant rare earth ions, but such implantation is unsuitable for thick films due to the film damage produced by implantation with ions having the high energies required for the film penetration. PECVD does offer some promise, in that a suitable dopant species may be introduced into the reacting plasma in a non-vapour form. Jerominek et al have produced microcrystals of cadmium sulphide in Corning 7059 glass as well as microscope slides<sup>15</sup> using RF sputtering, and the technique used could possibly be extended to coat silica. Of the remaining three techniques, sol-gel, oxidation and flame hydrolysis, all could be used for non-linear doping by virtue of the porosity of the films produced, although flame hydrolysis would be taken in preference to oxidation by virtue of the ease of deposition and lower loss films produced by the

technique. Furthermore, film index and thickness can readily be tailored to match those encountered in fibres. One possible drawback common to each of the aforementioned techniques is the high processing temperature required to sinter the porous films. For substrate materials such as silica or silicon, this does not present insurmountable difficulties. The use of silicon as a substrate material is desirable because of the flat surface on which to coat films, and also because of the logical extension of optical and electronic integration possible with such a substrate material.

With regard to both active and passive materials on a single substrate the three techniques mentioned offer the greatest potential for the least work. Carbon dioxide laser processing<sup>23</sup>, can be used to delineate an area by localised pore closure and it should then be possible to solution dope<sup>29,30</sup>, the enclosed area. By far the simplest of the three is the flame hydrolysis technique since the sol-gel films require slow drying and aging prior to use. It would therefore appear that the technique offering the greatest flexibility *at this moment in time*, for the fabrication of low-loss passive films, active films, and the potential for both on a single substrate is the Flame Hydrolysis technique.

The remainder of the chapter will discuss the Flame Hydrolysis technique in detail and will describe the deposition apparatus designed and fabricated by the author.

### 2.3 FLAME HYDROLYSIS DEPOSITION OF SILICA APPARATUS DESIGN AND CONSTRUCTION.

Flame Hydrolysis Deposition of silica is not a new technique. The idea was patented in 1942 by J F Hyde<sup>31</sup> whilst working at Corning Glass, New York. In his patent he describes the technique of vapour transport using a water bath to vaporize the silicon tetrachloride and the subsequent hydrolysis in an oxy-hydrogen torch. The fine silica particles - or "soot" - could be sintered during deposition using the same torch or alternatively the material could be subsequently fused in a furnace.

In essence, the technique now used remains unaltered. The volatile reagents are transported to an oxy-hydrogen torch where they are hydrolysed to produce a soot as before. The vapour pressures of the reagents are controlled by a low viscosity oil circulating the halide containers (or bubblers) whose temperature is precisely controlled. The vapour is transported by means of an inert carrier gas, the precise amounts of vapour transported being controlled by adjusting the flow of this gas through the bubblers. The resulting soot is subsequently sintered - with or

without a fusing atmosphere – to produce the transparent silica film. The Hydrogen Chloride waste gas produced is extracted during deposition and neutralised.

The refinements to the technique involve more sophisticated vapour control allowing precise quantities of the required halide, along with the introduction of vapour mixtures used to change the optical properties of the resulting silica glass. The movement of the oxy–hydrogen torch is now computer controlled, as is the rotation of the turntable on which the substrates to be coated are placed. This then allows accurate and repeatable layer thickness control of the silica soot, and subsequently of the resulting film.

The vapour mixtures generally used include Titanium Tetrachloride ( $\text{TiCl}_4$ ) or Germanium Tetrachloride ( $\text{GeCl}_4$ ) to raise the refractive index of the silica and Phosphorus Trichloride ( $\text{PCl}_3$ ) and/or Boron Trichloride ( $\text{BCl}_3$ ) to lower the required fusing temperature of the soot. Subsequent fusing takes place in a sintering furnace at temperatures of around twelve hundred to thirteen hundred degrees centigrade.

The deposition apparatus constructed consists of four units which will be discussed separately. They are as follows:–

- (1) GAS SUPPLY ASSEMBLY
- (2) BUBBLER CABINET
- (3) DEPOSITION CHAMBER
- (4) SCRUBBER SYSTEM

### 2.3.1 THE GAS SUPPLY ASSEMBLY

A gas supply system has been designed to support the bottled gases, valving and regulators used, and to pipe the gases necessary for the vapour transport and the hydrolysing flame. The assembly is also designed to support the necessary filters and driers associated with the carrier gas.

The gas used to transport the vapour is zero Grade Nitrogen. The "zero grade" refers to the purity of the gas such that the water content is below 10 ppm. It has been considered necessary to incorporate further nitrogen driers in the assembly to ensure that the gas is sufficiently dry (a dewpoint of  $-70\text{ }^\circ\text{C}$  being required to ensure no reaction of the halides in the pipelines). A  $2\text{ }\mu\text{m}$  particulate filter is incorporated to remove any particulate contaminants in the gas.

As well as being used for vapour transport, the nitrogen acts as a control gas for the pneumatic bellows valves (PBV's) which direct the path of the carrier gas

through the bubblers. The gas also purges the bubbler cabinet to maintain a dry atmosphere around the bubblers.

The pipework on the nitrogen line is designed to allow reverse purging of the nitrogen driers to regenerate the drying material, while maintaining the required flow of gas.

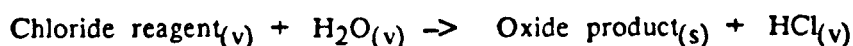
The hydrogen and oxygen lines are simpler in design. Both lines incorporate flowmeters to allow accurate settings of the gases to be used and the hydrogen line includes a flash arrester as a safety precaution. Stainless steel piping is used throughout the supply rack, as this material is more resistant to accidental damage by being knocked with the gas bottles. Once into the bubbler cabinet, Polytetrafluoroethane (PTFE) piping takes over, allowing flexibility and resistance to corrosion from the halide reagents. Similarly the H<sub>2</sub> and O<sub>2</sub> lines use PTFE inside the deposition chamber, allowing the flexibility required for the torch traversal. A schematic of the rack is shown in Figure 2.2.

### 2.3.2 THE BUBBLER CABINET

The bubbler cabinet constructed consists of a sealed glove box which is constantly purged with dry nitrogen to prevent hydrolysis of starting materials whilst loading the bubblers. The cabinet contains the bubblers in which are the starting materials in their liquid form. Four bubblers are used, containing the following:-

- 1 Silicon tetrachloride, (SiCl<sub>4</sub>). This produces silicon dioxide which acts as a host for the dopant materials.
- 2 Titanium tetrachloride, (TiCl<sub>4</sub>). Hydrolises to give titanium dioxide and is used to raise the refractive index of the silica glass
- 3 Phosphorus Trichloride (PCl<sub>3</sub>). Reacts to form phosphorus pentoxide incorporated to reduce the fusing temperature of the soot
- 4 Germanium Tetrachloride (GeCl<sub>4</sub>). This yields germanium dioxide, which serves the same purpose as the titanium dioxide in raising the refractive index

All of the reactions are of the form :-



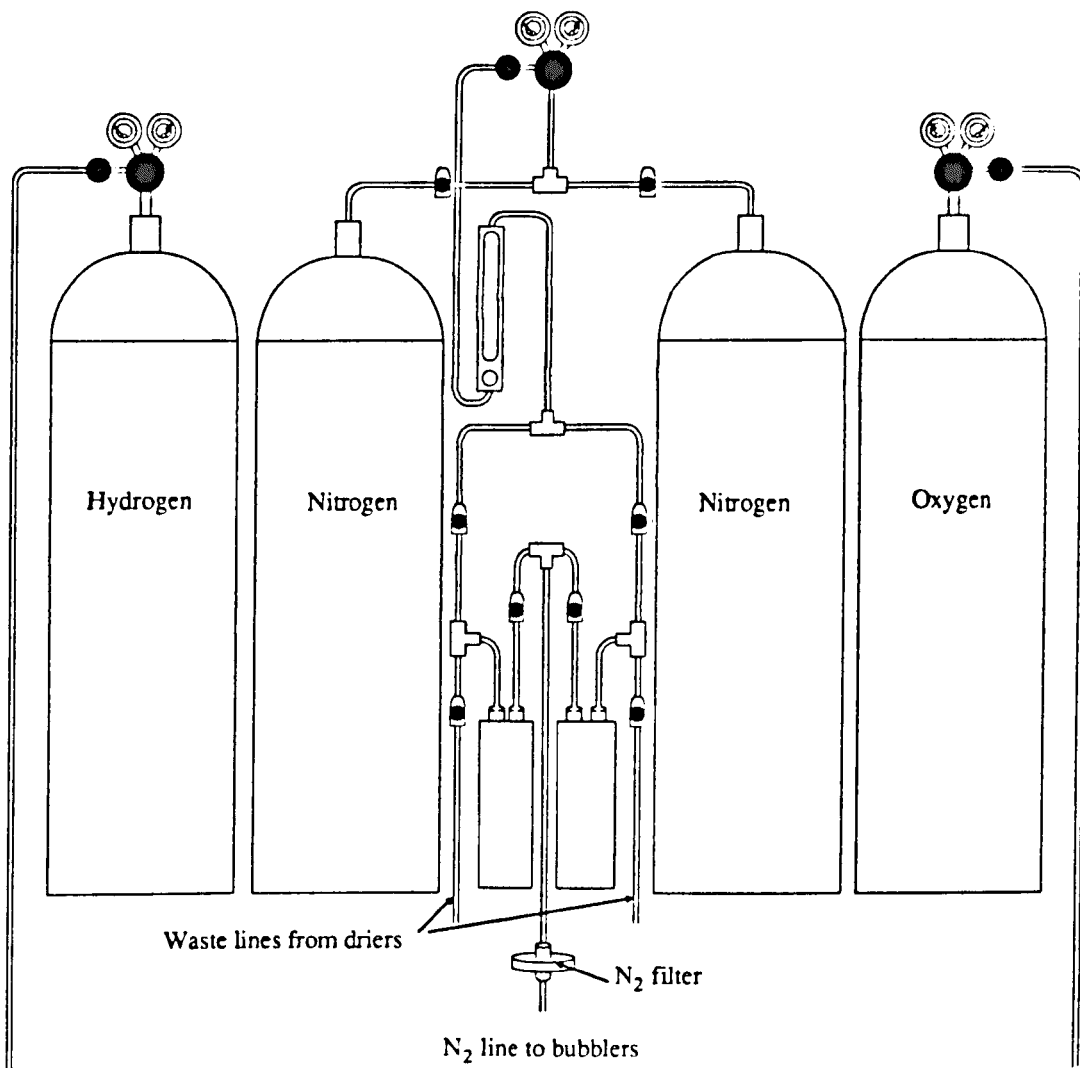


Figure 2.2 Schematic of gas supply rack

The vapour pressures of the chlorides are controlled by fixing the temperature of the liquids in the bubblers. This is achieved by circulating a low viscosity oil in the outer jackets of the bubblers, the temperature of which is controlled by a refrigeration/heater unit.

The nitrogen used is warmed to a temperature a few degrees above the oil temperature which then keeps the piping a few degrees warmer than the vapour and prevents any condensation in the pipework.

Pneumatic bellows valves (PBV's) control the path of the carrier gas. This allows the required flow rates to be set up while the gas flows to waste. The PBV's can then be opened to allow the gas flow through the bubblers.

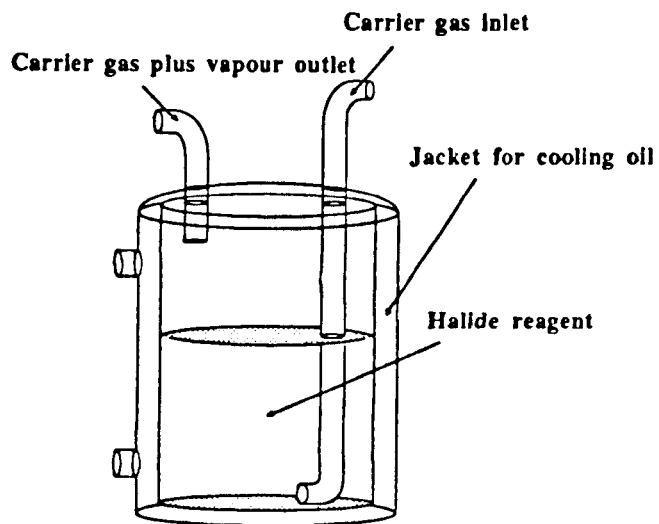


Figure 2.3 Schematic of bubbler

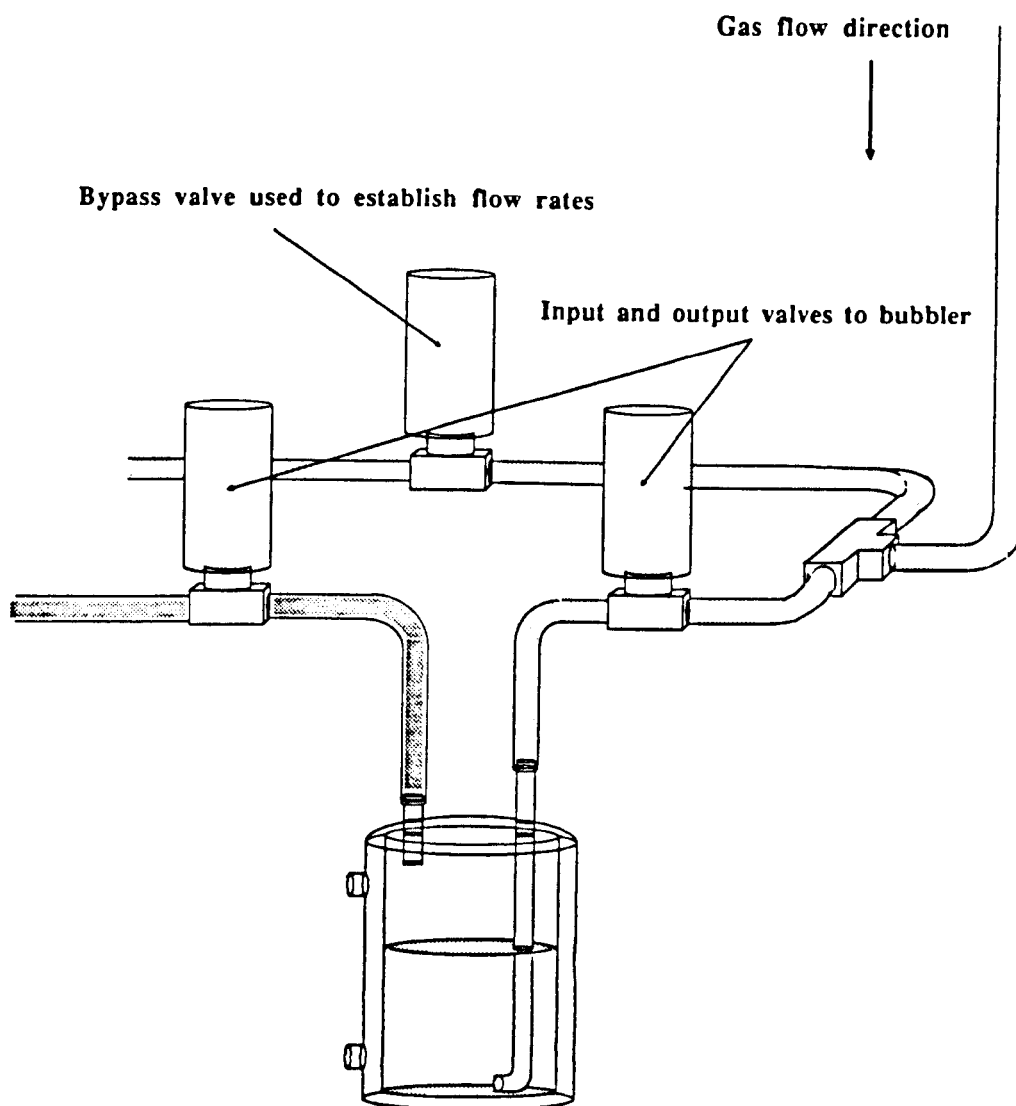


Figure 2.4 Schematic of bubbler complete with  
Pneumatic Bellows Valves (P.B.V.'s)

The control electronics are mounted in another cabinet directly above the

glove box. This cabinet contains the necessary mass flow controllers (MFC's), digital voltmeters and potentiometers required to set and monitor the gas flows for the bubblers. The cabinet also contains the solenoid valves and switchgear used to operate the PBV's. A single power supply is used for all of the electronic components.

### 2.3.3 THE DEPOSITION CHAMBER

It is within this chamber that the chloride vapours are hydrolysed using the oxy-hydrogen flame, the substrates are coated with the resulting soot and the waste gases are extracted to the scrubber system.

The chamber consists of a free standing rectangular box with a hinged opening to allow access to the interior. One of the remaining sides is made of a transparent perspex to allow the operator to observe the deposition. Waste gases are extracted from a large diameter opening opposite the hinged section, which is connected to an extraction fan.

The chamber houses the linear drive mechanism consisting of a long threaded screw connected to a stepper motor. The screw supports the platform to which the hydrolysing torch is mounted. The torch platform is so designed as to allow precise positioning of the torch with respect to the turntable. The torch itself is a modified silica Wickbold burner, consisting of three concentric tubes down which the combustion gases of hydrogen and oxygen and the reacting gases of the chlorides are channelled.

The turntable is interchangeable and two turntables designs are used. A larger diameter turntable is used for large, irregularly shaped substrates and a smaller turntable having machined disc recesses is used for the standard substrate discs. Both turntables are made of Aluminium which has been hard anodised to protect them from the corrosive  $\text{HCl}_{(v)}$ .

The stepper motor controlling the turntable is housed beneath the deposition chamber alongside the Digiplan stepper motors controller. This controller is connected to an IBM PC XT computer, a General Purpose Interface Bus being required to link the computer and controller.

The program used to control the stepper motors, and hence the soot deposition, is written in BASIC. The program allows independent variation of the traversal length and traversal rate of the torch as well as the rotation rate of the turntable.

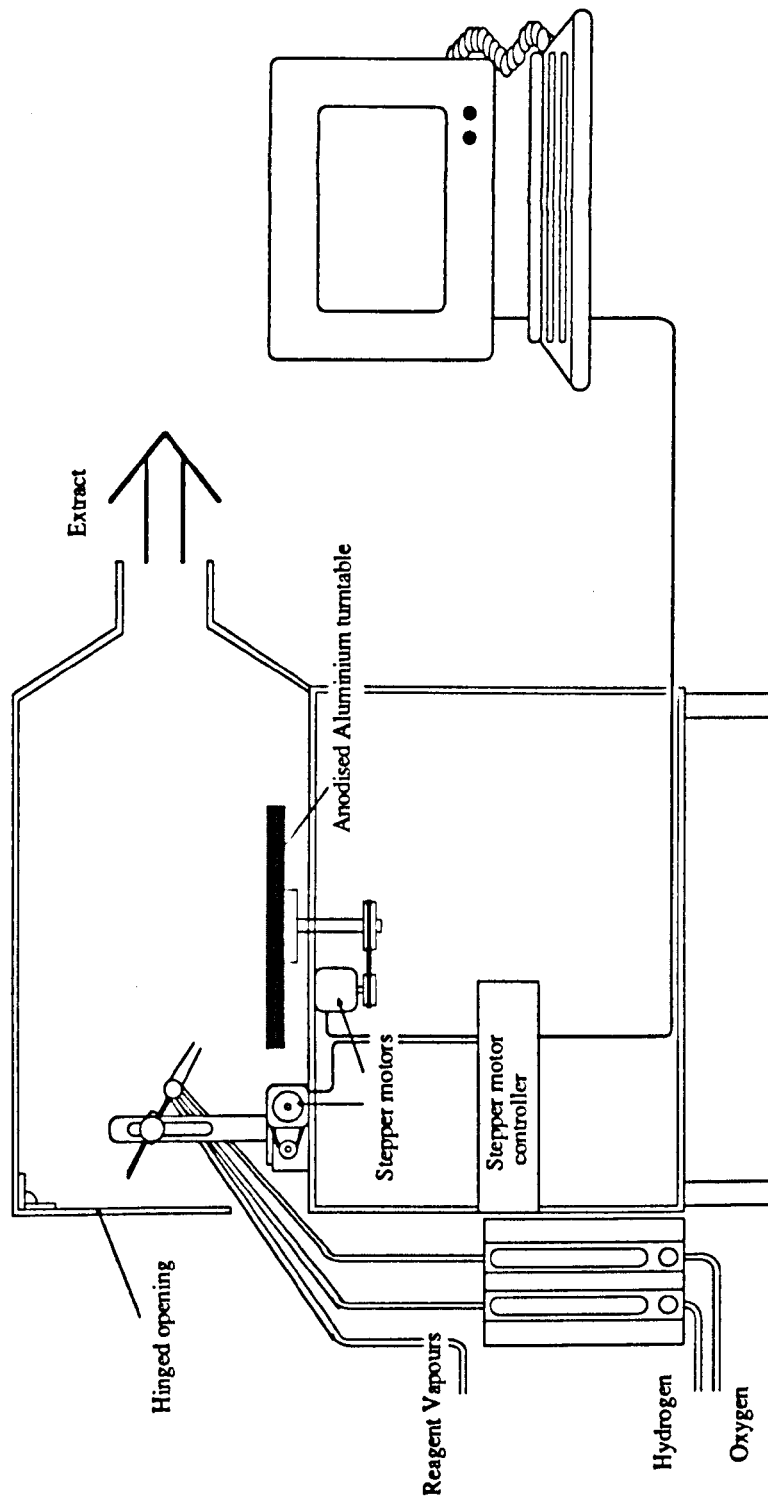


Figure 2.5 Schematic of deposition chamber and computer.

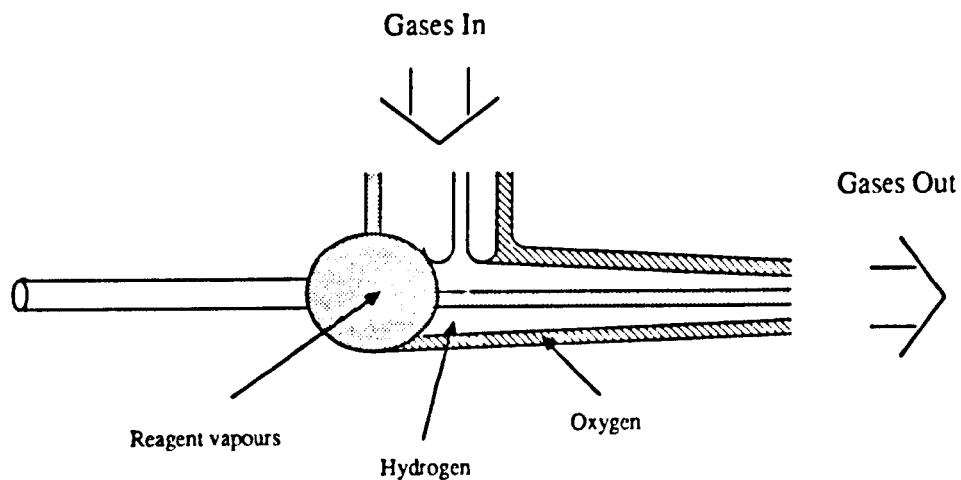
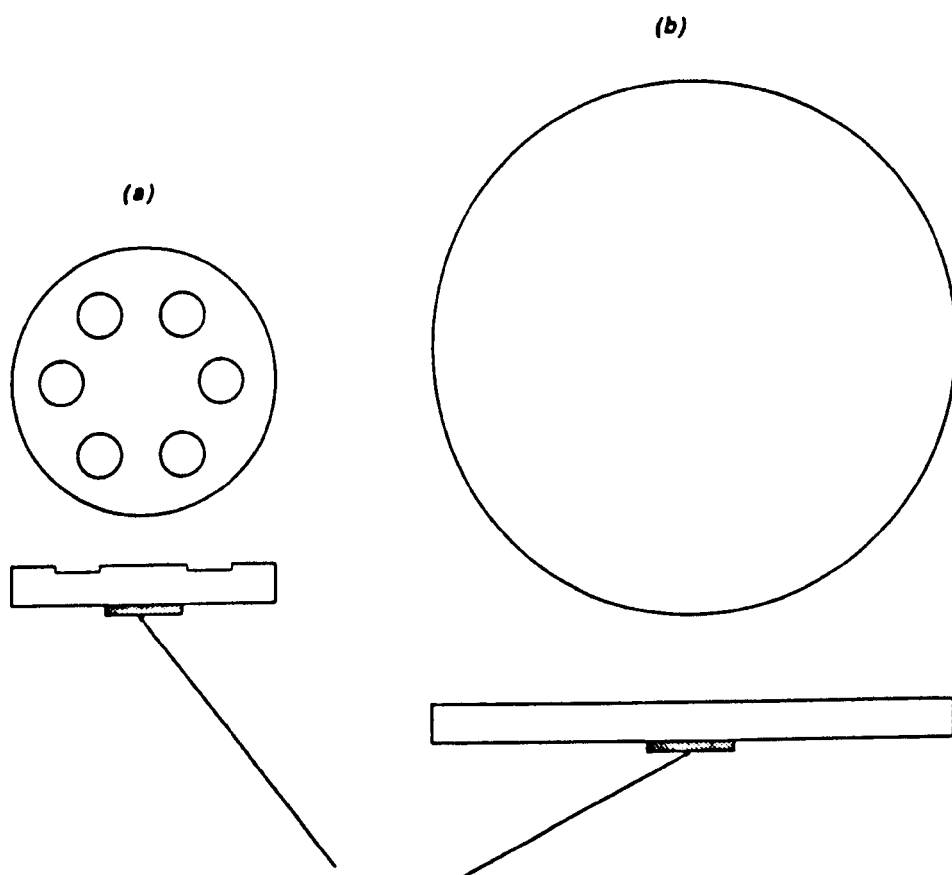


Figure 2.6 Modified silica Wickbold burner torch used for deposition



*Threaded brass base plate for fitting and removal of turntable from deposition chamber.*

Figure 2.7 Schematic of turntable designs

### 2.3.4 THE SCRUBBER SYSTEM

The scrubber system extracts the waste gases from the deposition chamber. These consist of  $\text{HCl}_{(v)}$  producing in the hydrolysis of the chlorides, and unreacted reagents. The gases are dissolved in water and pass into a settling tank where they are neutralised.

The system is constructed from stainless steel and consists of a series of baffles over which the gases are drawn. Spray bars are mounted between each successive baffle and provide 'curtains' of water through which the gases pass and in which they dissolve. The water containing the residues is passed into a separate storage tank directly below the scrubber. Here the acidic solution is neutralised before being disposed of.

Once the soot has been deposited the samples are fused into a transparent glass in a sintering furnace. The sintering theory and practice will be discussed in the next chapter.

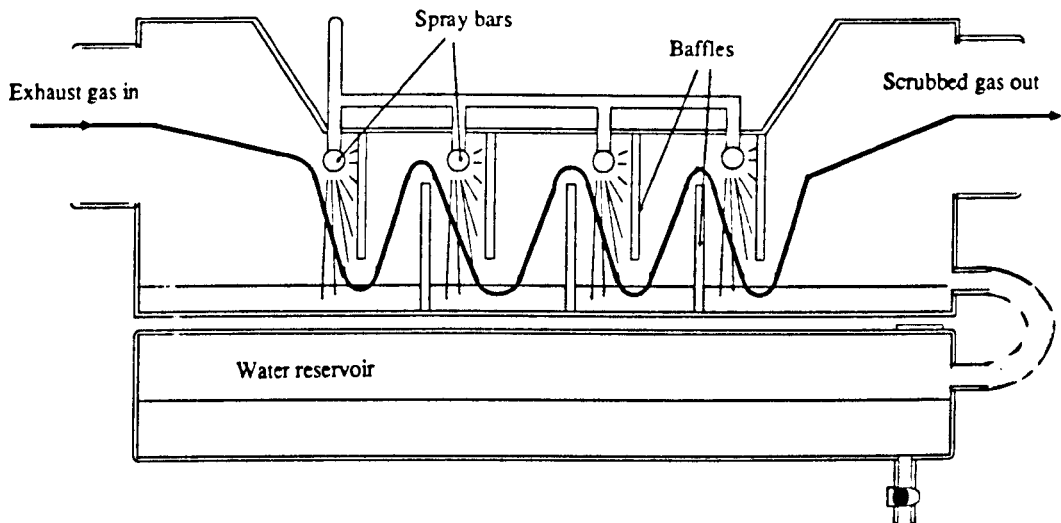


Figure 2.8 Schematic of scrubber system

## 2.4 REFERENCES

1. B.H. VERBEEK, C.H. HENRY, N.A. OLSSON, K.J. ORLOWSKY, R.F. KAZARINOV, B.H. JOHNSON  
J. Lightwave Tech., Vol. 6, No. 6, June 1988, pp1011–1015  
Integrated four-channel Mach-Zehnder multi/demultiplexer fabricated with Phosphorus doped Silica on silicon.
2. N. NOURSHARGH, E.M. STARR, J.S. McCORMACK  
SPIE, Vol. 578, Integrated Optical Circuit Engineering II, 1985, pp95–99  
Plasma deposition of integrated optical waveguides.
3. W. KERN, R.S. ROSIER  
J. Vac. Sci. Technol., Vol. 14, No. 5, Sept./Oct., 1977, pp1082–1099  
Advances in deposition processes for passivation films.
4. K. IMOTO, I. ASAI, H. SANO, M. MAEDA  
E.C.O.C. '88  
Silica glass waveguiding structure and its application to a multi/demultiplexer.
5. A.S. HUANG, Y. ARIE, C.C. NEIL, J.M. HAMMER  
Appl. Opt., Vol. 24, No. 24, 15th Dec. 1985, pp4404–4407  
Study of refractive index of  $\text{GeO}_2:\text{SiO}_2$  mixtures using deposited thin-film Optical waveguides.
6. I.K. NAIK  
Appl. Phys. Lett., Vol. 43, No. 6, 15th Sept. 1983, pp519–520  
Low-loss optical waveguides fabricated by nitrogen ion implantation.
7. T. IZAWA, H. MORI, Y. MURAKAMI, N. SHIMIZU  
Appl. Phys. Lett., Vol. 38, No. 7, 1st April 1981, pp483–485  
Deposited silica waveguide for integrated optical circuits.
8. M. KAWACHI, M. YASU, T. EDAHIRO  
Electronics Lett., Vol. 19, No. 15, 21st July 1983, pp583–584  
Fabrication of  $\text{SiO}_2/\text{TiO}_2$  glass planar optical waveguides by flame hydrolysis Deposition.
9. R.V. RAMASWAMY, T. CHIA, R. SRIVASTAVA, A. MILIOU, J. WEST  
Proc. SPIE Symp. on Innovative Science and Technology, Los Angeles, June 10–15th 1988  
Gel-Silica Waveguides.
10. W.A. PLISKIN  
J. Vac. Sci. Technol., Vol. 14, No. 5, Sept/Oct 1977, pp1064–1081  
Comparison of properties of dielectric films deposited by various methods.
11. S.M. SZE  
VLSI Technology, McGraw-Hill, 1983

- 12.G.W.B. ASHWELL, S.J. WRIGHT  
Semiconductor International, Vol. 134, Jan. 1985
- 13.S.D. HUBBARD, B.J. AINSLIE, S.A. BAILEY, G.D. MAXWELL  
Proc. SPIE, Vol. 1125, April 1989, pp85–92  
Arsenic doped silica as a passive waveguiding material.
- 14.Z.Y. YIN, B.K. GARSIDE  
Appl. Opt., Vol. 21, No. 23, 1st Dec. 1982, pp4324–4328  
Low-loss GeO<sub>2</sub> optical waveguide fabrication using low deposition rate R.F. Sputtering.
- 15.H. JEROMINEK, S. PATELA, M. PIGEON, Z. JAKUBCZYK, C. DELISLE, R. TREMBLAY  
J. Opt. Soc. Am. B, Vol. 5, No. 2, Feb. 1988, pp496–506  
Non-linear optical waveguides made of thin films of glass doped with Semiconductor microcrystals.
- 16.P.C. SCHULTZ  
Appl. Opt., Vol. 18, No. 21, 1st Nov. 1979, pp3684–3693  
Progress in optical waveguide processes and materials.
- 17.H. MORI, N. SHIMIZU  
IEEE J. Quant. Electron., Vol. QE-18, No. 4, April 1982, pp776–781  
Multimode deposited silica waveguide and its application to an optical Branching circuit.
- 18.K. SUSU, I. MATSUYAMA, S. SATOH, T. SUGANUMA  
Electronics Lett., Vol. 18, No. 12, 10th June 1982, pp499–450  
New optical fibre fabrication method.
- 19.D. AVNIR, V.R. KAUFMAN, R. REISFELD  
J. Non-Cryst. Solids, Vol. 74, 1985, pp395–406  
Organic fluorescent dyes trapped in silica and silica/titania thin films  
By the Sol-gel method.
- 20.D.E. ZELMON, H.E. JACKSON, J.T. BOYD  
SPIE, Vol. 578, Integrated Optical Circuit Engineering II, 1985, pp100–102  
Use of thermal nitridation to fabricate low-loss planar optical waveguides in SiO<sub>2</sub>.
- 21.E.R. SCHINELLER, R.P. FLAM, D.W. WILMOT  
J. Opt. Soc. Am., Vol. 58, Sept. 1968, pp1171–1176  
Optical waveguides formed by proton irradiation of fused silica.
- 22.R.D. STANDLEY, W.M. GIBSON, J.W. RODGERS  
Appl. Opt., Vol. 11, June 1972, pp1313–1316  
Properties of ion-bombarded fused quartz for integrated optics.
- 23.Y.YAMADA, M. KAWACHI, M. YASU, M. KOBAYASHI  
Appl. Opt., Vol. 24, No. 4, 15th Feb. 1985, pp454–455

Carbon dioxide laser processing of porous glass layers for optical waveguides.

24.M. KOBAYASHI

Second Optoelectronics Conf., (OEC '88), Tech. Dig., Oct. 1988, Tokyo,  
Paper 2C2-1

Integrated optics based on glass materials.

25.G.W. SCHERER, J.C. LUONG

J. Non-Cryst. Solids, Vol. 63, 1984, pp163-172

Glasses from Colloids

26.M. YAMANE, S. ASO, S. OKANO, T. SAKAINO

J. Mater. Sci., Vol. 14, 1979, pp607-611

Low temperature synthesis of a monolithic silica glass by the pyrolysis of a  
Silica gel.

27.J. ZARZYCYCKI, M. PRASSAS, J. PHALIPPOU

J. Mat. Sci., Vol. 17, 1982, pp3371-3379

Synthesis of glasses from gels: the problem of monolithic gels.

28.AARNIO

ECOC '88

An integrated optic polarization splitter on silicon substrate

29.J. STONE, C.A. BURRUS

Appl. Phys. Lett., Vol. 23, No. 7, 1st Oct. 1973, pp388-389

Neodymium-doped silica lasers in end-pumped fibre geometry

30.N.F. BORELLI, M.D. COTTER, J.C. LUONG

IEEE J. Quant. Electronics, Vol. QE-22, No. 6, June 1986, pp896-901

Photochemical method to produce waveguiding in glass.

31.J.F. HYDE

U.S. PATENT No. 2,272,342, Feb. 10th, 1942

Method of making a transparent article of silica.

32.J.A. AMICK, G.L. SCHNABLE, J.L. VOSSEN

J. Vac. Sci. Technol., Vol. 14, No. 5, Sept./Oct. 1977, pp1053-1063

Deposition Techniques for dielectric films on semiconductor devices.

## CHAPTER 3    THEORY AND PRACTICE OF SINTERING

Sintering occurs when powders, in this case, silica, are heated to, or near their melting point. The following chapter is concerned with a general review in essentially phenomenological terms of the theory behind this effect and the experimental verification of the theoretical models.

The theoretical framework developed to describe the process will be traced from the early work of Frenkel<sup>1</sup> in which the assumption underpinning the sintering theory is outlined. Developments in the theory as applied to glasses rather than metals and crystals, by authors such as Kingery and Berg<sup>2</sup>, Mackenzie and Shuttleworth<sup>3</sup> and Scherer<sup>4</sup> will be discussed.

The effect of the presence of sintering atmospheres on densification rates will be included, the work on such effects being traced from the behaviour of silica microspheres<sup>5,6</sup>, through to experiments on preforms fabricated using flame hydrolysis<sup>7</sup>.

Analysis of sintering was not carried out by the author beyond the level necessary for a general understanding of the mechanisms involved in, and the factors affecting the process, the main aim being to produce bubble free, homogeneous films. It was felt that while further investigation would be interesting, it lay outwith the scope of this work.

The various stages of sintering will be pictorially represented using Scanning Electron Micrographs of films prepared by the author. Other experimental work will be described in the following chapters.

### 3.1 THEORETICAL ASPECTS OF SINTERING

Much of the early work on sintering was concerned with the consolidation of metal powders and crystals and the calculation of the rates of such consolidation. Frenkel's model<sup>1</sup> was no exception. In his treatment of the problem of calculating rates of densification, he assumed that crystals behaved in the same way as amorphous materials at high temperature. Using this assumption he set up an energy balance equation in which the driving force of sintering was viscous flow. The energy dissipated in such flow came from the surface energy liberated by the reduction in surface area of the compact.

This view was later proved to be mistaken<sup>2</sup>, concerning the behaviour of crystals and amorphous materials in sintering. However, the viscous flow mechanism was found to be applicable to Newtonian solids, such as glass, in which the viscosity is independent of the strain rate.

In the model used by Mackenzie and Shuttleworth<sup>2</sup>, a compact of closely packed glass spheres was considered. Two such spheres are in contact with each other at only one point. The initial stage of sintering is the development of a "neck" between the spheres at this point of contact, followed by the reduction of the centre-to-centre separation of the spheres. Both effects are attributed to surface tension. See Fig 3.1.

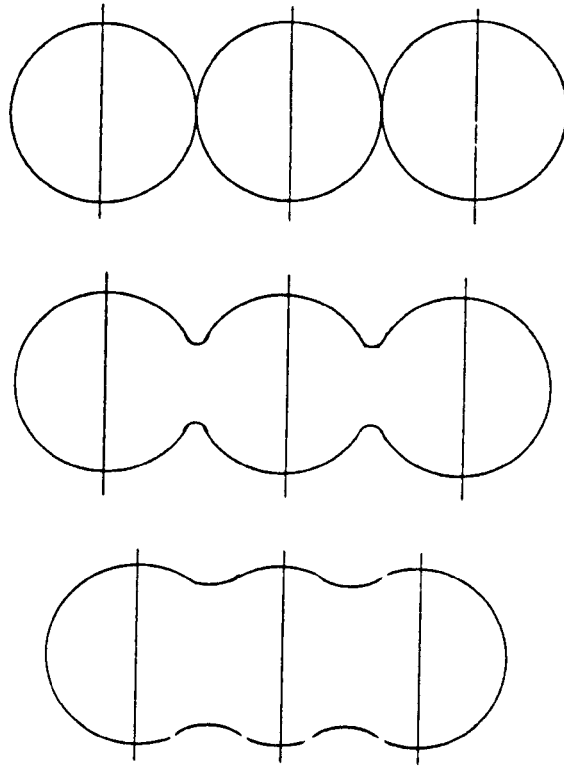


Figure 3.1 Schematic of 'necking' in spheres.

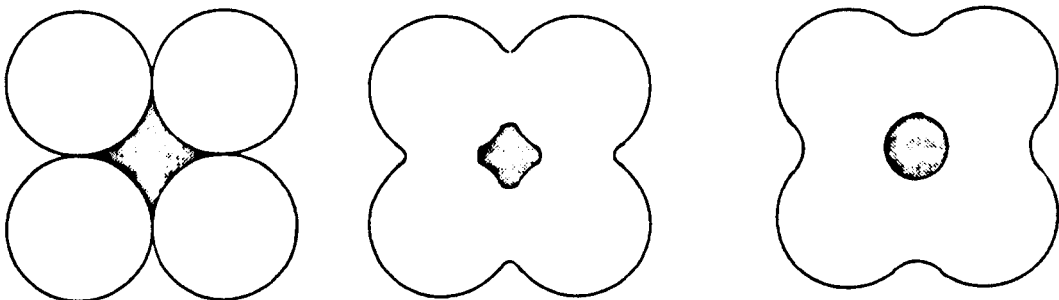


Figure 3.2 Schematic of pore shape changes during sintering

In a compact, such necking between all of the nearest neighbours results in a gradual closure of the open structure between spheres and the formation of voids or pores. Once closed, the pore shape becomes spherical, due to macroscopic viscous flow and surface tension effects. The analysis of sintering then is concerned with modelling the closure of such spherical cavities due to capillary pressure. Mackenzie and Shuttleworth considered the shrinkage of an isolated, closed, spherical cavity, assuming in their model the volume of surrounding material to be much greater than the pore volume. They considered the cases of empty cavities; cavities containing a fixed volume of gas; and cavities containing a fixed pressure of gas.

Such a model, however, is unsuited to the description of the behaviour of the densification of preforms fabricated by (a) flame hydrolysis, (b) sol-gel process and (c) leached, phase separated glasses. Figure 3.3 (a), shows the type of structure produced by flame hydrolysis. In it, one sees a very open structure made up of silica particles joined together forming a network of randomly connected bridges. In this structure, the pores are open and the pore volume is much larger than the volume of surrounding solid material.

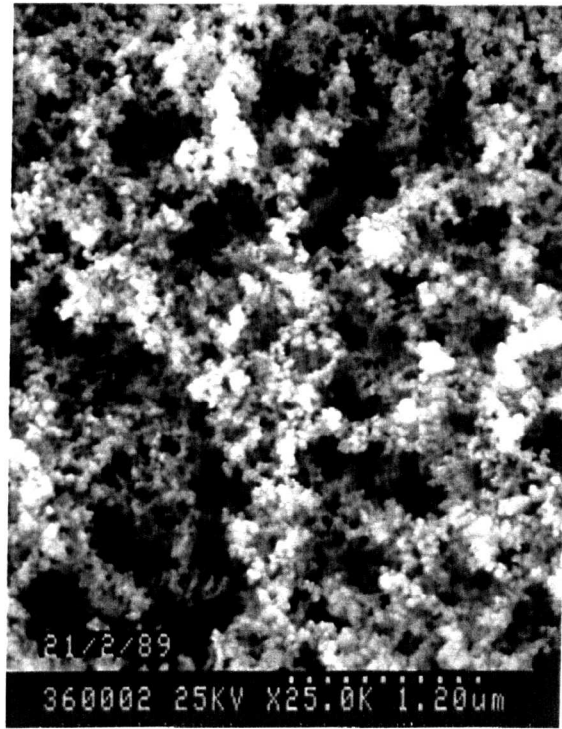
In the very early stages of sintering, the behaviour of necking and inter-particle distance reduction is observed, fig 3.3(b). This serves the purpose of consolidating the bridge network and strengthening the structure.

It was Scherer<sup>4</sup> who provided a model suitable for such systems. This model consists of a unit cell made up of a cubic array of intersecting cylinders, fig 3.4. As densification continues the height of the cylinder is reduced and its radius increase. The same energy balance concept is used and the same viscous flow mechanism proposed.

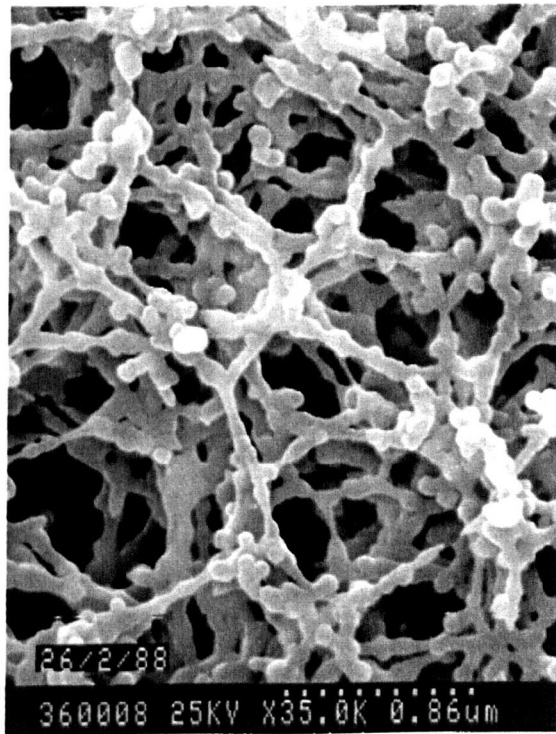
Eventually, when the size of the radius exceeds half of the cylinder height, the pores become closed. At this point the earlier analysis of Mackenzie and Shuttleworth applies and the densification kinetics follow the rate of collapse of the pore.

The basic steps used by all of the workers in this area involve the calculation of an expression for the rate of energy dissipated in viscous flow (such an expression is geometry-dependent). This is equated to the rate of energy released from the reduction in surface area. Integration of the resulting equation with respect to time yields an expression which describes the rate of densification of the compact.

It should be pointed out that the volume of solid material remains unchanged, but because of shear stresses its shape changes and the material flows into pores resulting in the observed density increase. Figs.3.5 (a-d).



(a)



(b)

Figure 3.3 SEM photographs of Flame Hydrolysis preforms  
(a) Un-sintered material, (b) Initial stage of sintering

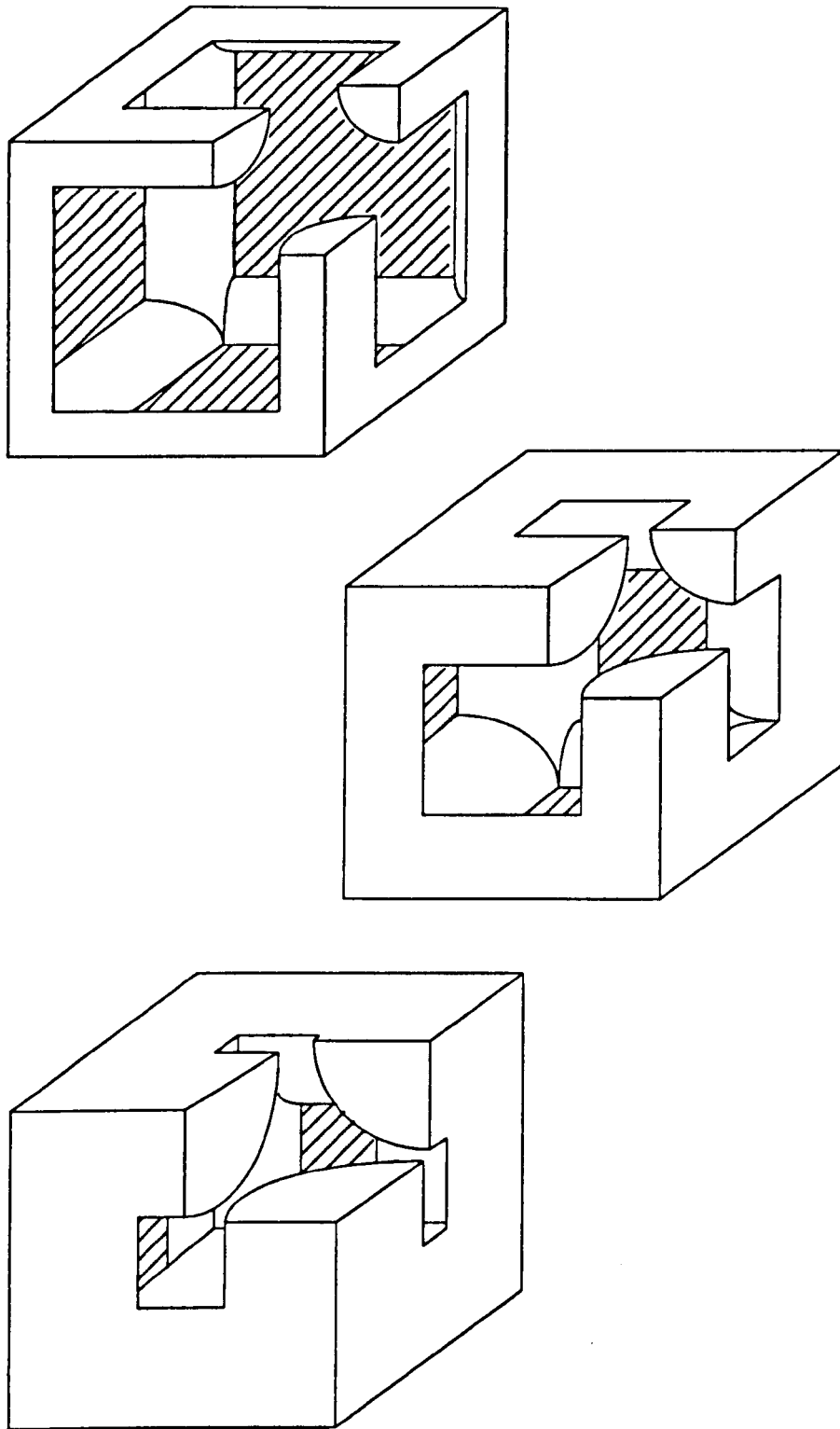
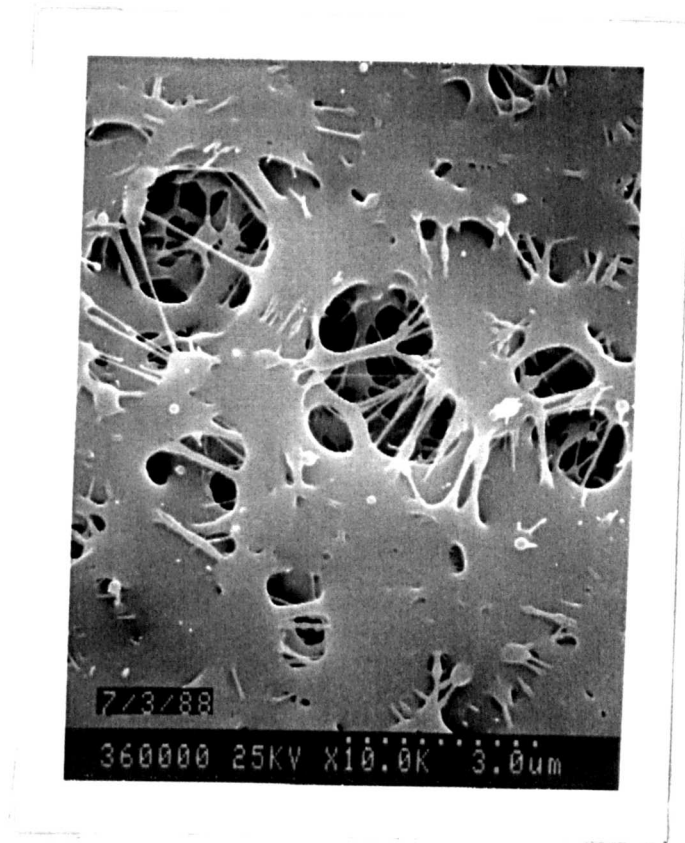
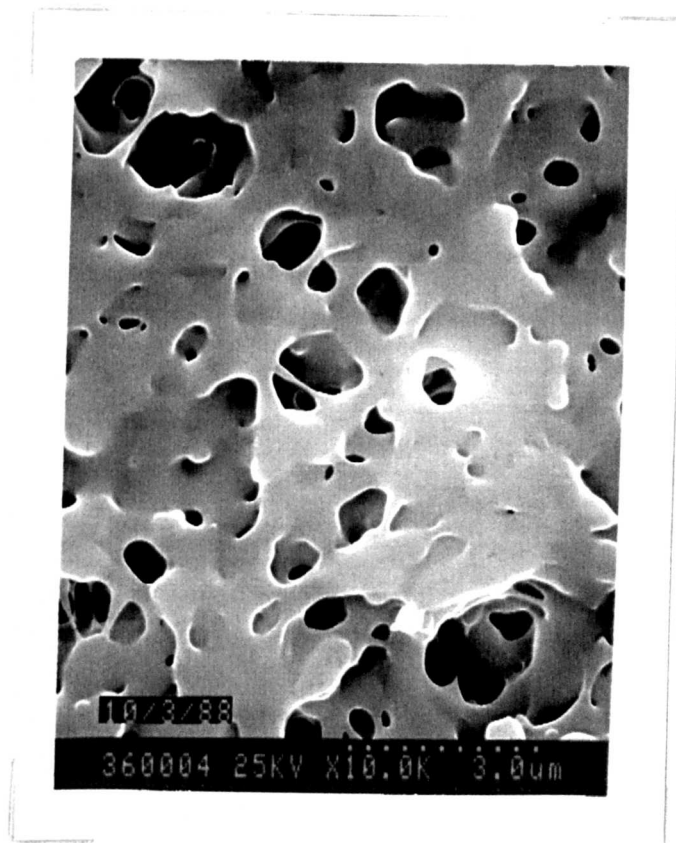


**Figure 3.4 Schematic detailing unit cell structure from Scherer's model**  
Depicts cubic array collapse in which cylinder height decreases and radius increases. Pore closure results when radius exceeds height/2.

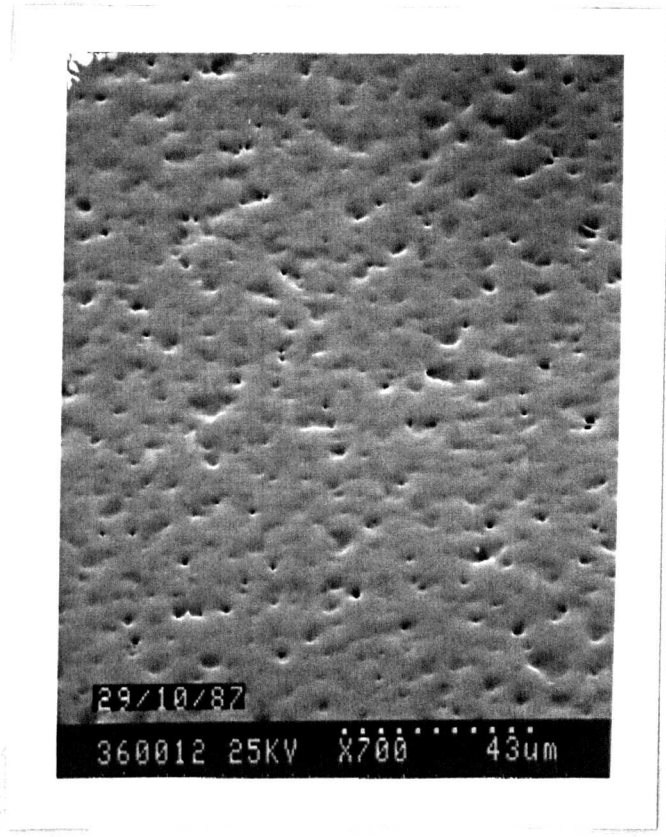


(a)

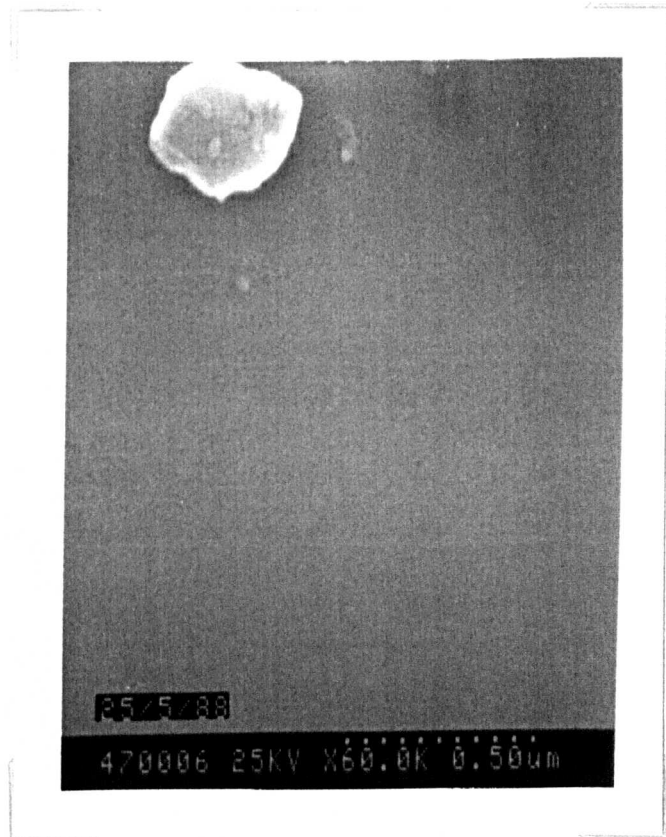


(b)

Figure 3.5 SEM photographs showing increasing degrees of sintering



(c)



(d)

Figure 3.5 SEM photographs showing increasing degrees of sintering

### 3.1.1 ATMOSPHERIC EFFECTS

So far, we have neglected the effect of gas on the properties of the material, as well as the effect of the presence of gas in the pores. Using the concepts already outlined such effects can be considered. The presence of an atmosphere during sintering can affect the glass sinter in a number of ways. Most important for our purposes are the effect of a sintering atmosphere on:-

- (1) surface tension and viscosity of the solid material, and
- (2) pore closure

A number of authors have studied the areas outlined, both theoretically and experimentally. Compositional factors such as doping levels of, for example, boron oxide ( $B_2O_3$ ) in silica which effect both sintering rates and bubble formation<sup>8</sup> are not included in this section but will be considered later.

### 3.1.2 COLLAPSE OF CLOSED PORES

All of the porous preform types so far considered — no matter how they are fabricated — go through the final stage of sintering which involves the collapse of closed pores. This final stage is strongly atmosphere dependent and the type of gas present inside the pore will determine the quality of the resulting glass.

The results of the theoretical analysis will be described, following the analysis of Mackenzie and Shuttleworth, and experimental verification by Sudo et al<sup>11</sup> and Scherer<sup>7</sup> will be used to complete the picture.

If we initially consider a model of a compact of arbitrary size and shape which contains spherical pores of equal size. Further, if the radius is small compared with the surrounding homogeneous material, and the pores contain no gas, then the effect of surface tension is to produce a pressure between the surrounding material and the pores. This has the effect of closing the pores.

Such a pressure is even throughout the compact and hence the increase in density will be uniform. The pores decrease in size and separation, but not in number. Therefore the sintering will be independent of the size and shape of the compact. If the pores are not equal in size, then it is obvious that the small pores will disappear more rapidly than the larger ones.

It is worth mentioning at this point that this analysis is concerned with pores completely surrounded by a homogeneous continuum, and as such the reduction in

sintering rate at a boundary, observed in the sintering of microspheres, will not be encountered.

By introducing a gas into the pores, we can drastically alter the rate of sintering and even cause the pores to expand. Such behaviour depends on the type of gas present, the amount of such gas and on its pressure.

We can consider two types of behaviour:—

- 1 Constant mass of gas inside the pore. This situation applies if the gas is non-diffusing and does not dissolve in the material
- 2 Constant pressure of gas inside the pore. This is the case for gas which dissolves in the material and has a sufficiently large rate of diffusion to maintain an equilibrium pressure between pore and material

If the pore contains a non-diffusing gas, then there will be negligible change in the mass of gas present during sintering. As a consequence, the pore radius will reach an equilibrium position at which the pressure due to the surface tension is balanced by the pressure exerted on the material by the gas. This results in an equilibrium density of the consolidated material. Whether such bubbles will impair the optical transparency of glass sintered under such a situation would depend on the equilibrium pore radius and the wavelength of light used to probe the glass.

With a diffusing gas, the situation is different. If the rate of diffusion is low, then this will be the rate determining step in sintering and the analysis above will apply. If, however, large quantities of gas can dissolve in the material with an appreciable rate then there will be an equilibrium between the pressure of the gas inside the pore and the pressure exerted by surface tension. This pressure will be maintained as sintering proceeds. While it will reduce the sintering rate, it will not inhibit it.

It is interesting to consider such a situation where there is a range of pore sizes. The dissolving gas exerts a constant pressure ( $P$ ) inside the pores. Where this pressure is greater than that due to surface tension, ( $\gamma$ ), the pores will expand, whilst smaller pores will collapse.

$$\begin{array}{ll} P = 2\gamma/R & \text{— equilibrium} \\ P > 2\gamma/R & \text{— pore expansion} \\ P < 2\gamma/R & \text{— pore contraction} \end{array}$$

— where  $R$  is the pore radius.

This suggests that in such a material, the small pores shrink at the expense of

the larger pores, and the sintering rate will be determined by the rate of closure of the larger pores.

## 3.2 EXPERIMENTAL VERIFICATION

### 3.2.1 SURFACE TENSION AND VISCOSITY EFFECTS

Parikh, in 1958,<sup>9</sup> studied the effect on *surface tension* of various atmospheres for soda-lime silicate glasses, fused silica and lead disilicate glass, paying most attention to the first glass type. The surface tension was determined by a fibre elongation method in which a heated fibre extends until its weight is balanced by the contracting force due to surface tension.

Fused silica was studied in the temperature range 1100°C – 1300°C using water and dry nitrogen as atmospheres. In both cases the surface tension appeared unaffected.

This work was extended by Tseng and Yu<sup>5</sup> when studying the effect of H<sub>2</sub>O(g), N<sub>2</sub>, air and HCl(g) on the sintering of such compacts. The H<sub>2</sub>O(g) atmosphere resulted in fully sintered compacts in less than 90 mins. This was regarded as being a consequence of the reduction of both viscosity, ( $\eta$ ), and surface tension, ( $\gamma$ ), of SiO<sub>2</sub>. The increased densification rate suggested that viscosity had been reduced more, since fractional linear shrinkage ( $\Delta F/F$ ) is proportional to surface tension divided by viscosity.

$$\Delta F/F \propto \gamma/\eta$$

where F is length.

The air and N<sub>2</sub> atmospheres used required much longer sintering times to produce the same density of material, 11hrs and 100hrs respectively, whereas the HCl(g) was found to inhibit sintering.

Tseng and Yu further demonstrated the co-operative effect of the surface tension as applied to the sintering of such compacts. A sample fused for 45mins in an N<sub>2</sub> + H<sub>2</sub>O(g) atmosphere exhibited a reduced degree of sintering at the compact surface as compared with the interior.

Hetherington et al<sup>10</sup> studied the effect on the viscosity of vitreous silica of hydroxyl content and metallic impurities. The temperature range studied lay between 900°C and 1400°C. Their results showed that the viscosity was reduced for increasing hydroxyl content. Similar results were obtained for increasing amount or metal impurities or effectively any impurity which broke the Si-O-Si bonds.

### 3.2.2 EFFECT OF ATMOSPHERES ON PORE CLOSURE

Sudo et al<sup>11</sup>, studied the effect of Helium/Argon mixtures as a sintering atmosphere in the production of bubble free glass. The fabrication technique used to produce the porous glass is very similar to the Flame Hydrolysis deposition technique used by the author. The Vapour phase Axial Deposition (VAD) technique produces preforms which are sintered and pulled into glass optical fibres and as a consequence of this application, highly transparent, bubble free glasses are required. The sintering is achieved by pulling the porous preform through a furnace with a particular thermal gradient, reaching a maximum temperature of around 1600°C. This produces a sintered preform ready to be pulled into a fibre. In their analysis they concentrated on the final stages of sintering involving the collapse of closed pores.

Since both gases can diffuse through the bulk material<sup>12</sup>, the problem is that of a fixed pressure inside the pore. However, in this case, since the rod is being pulled through a temperature gradient, there is an additional term involved due to the expansion of the gas trapped in the pore, with increasing temperature. This has the effect of changing the pore volume. From this analysis and using the gas diffusion data from Perkins and Begeal<sup>12</sup>, critical pore diameters – being the values of diameter at which the volume expansion is balanced by the surface tension – were calculated. For Helium,  $d_c = 500 \mu\text{m}$ , indicating that pores having diameters larger than this value would expand during heating. The value for argon is  $d_c = 0.6 \mu\text{m}$ , reflecting the much lower diffusivity of argon in silica. The value for argon is in reasonable agreement with the experimental value obtained by sintering in this atmosphere. It is clear from this analysis that He atmospheres will assist pore closure, since in practice, in the latter stages of sintering, 500  $\mu\text{m}$  diameter pores are not encountered.

Whilst the experimental arrangement used by Sudo et al differs from the theoretical model of Mackenzie and Shuttleworth, the results show how gases with different diffusivities inside closed pores can markedly effect the behaviour of the pores during sintering.

Scherer<sup>7</sup> carried out experimental work on the sintering of three types of porous glass preforms made using different techniques. They were:–

- (a) Flame Hydrolysis
- (b) Sol–gel
- (c) Leached phase–separated glass

All preforms were fired in a Helium atmosphere. The Flame Hydrolysis preform also being fired in a moisturised He atmosphere. Whilst his work was

concerned with the experimental verification of his theoretical model and not on atmospheric effects, he did report an interesting result. The Flame Hydrolysis preforms were very heavily hydrated during fabrication, and even a moist He atmosphere had the effect of drying the preform during sintering. Furthermore the preforms were very sensitive to ambient humidity and as a result yielded a range of viscosity values.

### 3.3 CONCLUSIONS

The theoretical framework behind the sintering of silica powders has been presented and experimental verification of such models described. The effect on fusing of the presence of particular atmospheres has been discussed and is found to strongly effect the quality of the sintered glass. The presence of water vapour appears to reduce the viscosity, allowing greater rates of densification. However, with heavily hydrated preforms such as those encountered in the Flame Hydrolysis technique, even a moist fusing atmosphere can dry the sample and reduce the sintering rate.

### 3.4 REFERENCES

1. J. FRENKEL  
J. Phys. (Moscow), Vol. 9, No. 5, 1945, pp385-391  
Viscous flow of crystalline bodies under the action of surface tension.
2. W.D. KINGERY AND M. BERG  
J. Appl. Phys., Vol. 26, No. 10, Oct. 1955, pp1205-1212  
Study of the initial stages of sintering solids by Viscous flow, Evaporation-Condensation, and Self-diffusion.
3. J.K. MACKENZIE AND R. SHUTTLEWORTH  
Proc. Phys. Soc. London, Vol. 62, No. 12-B, 1949, pp833-852  
Phenomenological theory of sintering.
4. G.W. SCHERER  
J. Am. Ceram. Soc., Vol. 60, No. 5-6, May-June 1977, pp236-239  
Sintering of low density glasses: I, Theory.
5. T.Y. TSENG AND J.J.YU  
J. Materials Sci., Vol. 21, 1986, pp3615-3624  
Various atmosphere effects on sintering of compacts of SiO<sub>2</sub> microspheres.
6. G.C. KUCZYNSKI  
J. Appl. Phys., Vol. 20, Dec. 1949, pp1160-1163  
Study of the sintering of glass.
7. G.W. SCHERER  
J. Am. Ceram. Soc., Vol. 60, No. 5-6, May-June 1977, pp239-243  
Sintering of low-density glasses:II, Experimental study.
8. M.F. YAN, J.B. MACCHESNEY, S.R. NAGEL, W.W.RHODES  
J. Mater. Sci., Vol. 15, 1980, pp1371-1378  
Sintering of optical waveguide glasses.
9. N.M. PARIKH  
J. Am. Ceram. Soc., Vol. 41, No. 1, Jan. 1958, pp18-22  
Effects of atmosphere on surface tension of glass.
10. G. HETHERINGTON, K.H. JACK, J.C. KENNEDY  
Phys. Chem. Glasses, Vol. 5, No. 5, Oct. 1964, pp130-137  
The viscosity of vitreous silica.
11. S. SUDO, T. EDAHIRO, M. KAWACHI  
Trans. IECE Jpn., Vol. E63, No. 10, Oct.1980, pp731-737  
Sintering processes of porous preforms made by VAD method for optical Fibre fabrication.
12. W.G. PERKINS AND D.R. BEGEAL  
J. Chem. Phys., Vol. 54, No.4, 15th Feb. 1971, pp1683-1694  
Diffusion & permeation of He,Ne,Ar,Kr,& D<sub>2</sub> through silicon dioxide thin films.

## CHAPTER 4 FLAME, PARTICLE & CHEMICAL CONSIDERATIONS

The following chapter is concerned with a discussion of aspects of the film deposition, and structure of the resulting material. Particle nucleation and growth in the oxy-hydrogen flame will be outlined, following the work of Ulrich<sup>1</sup>, Juillet et al<sup>2</sup> and George et al<sup>3</sup>. Chemical and structural aspects of the deposited soot will be considered drawing on the results of workers such as Edahiro et al<sup>4</sup> and Potkay et al<sup>5</sup> on Flame Hydrolysis systems (more specifically VAD fibre systems). Substrate temperature effects will be mentioned, with reference to the changes which result in the structure of deposited soot. Phase considerations concerning the consolidated soot will be discussed with reference to the phase diagrams of the binary systems SiO<sub>2</sub>/P<sub>2</sub>O<sub>5</sub><sup>6</sup>, SiO<sub>2</sub>/TiO<sub>2</sub><sup>7</sup> and SiO<sub>2</sub>/GeO<sub>2</sub><sup>8</sup>.

### 4.1 PHENOMENON OF PARTICLE FORMATION AND GROWTH IN THE FLAME.

The flame consists of a turbulent stream of hydrogen, oxygen and halide saturated nitrogen. The hydrogen and oxygen combust, producing a flame with a particular temperature profile, generally with  $T_{\max} > 2000^{\circ}\text{K}$ .

Ulrich<sup>1</sup> carried out experiments on silica produced from the hydrolysis of silicon tetrachloride in a hydrogen and air flame. He was able to show, theoretically, that the microscopic zones in which the chemical reactions and initial nucleation took place were very much smaller than the macroscopic turbulent eddies encountered. As such, only gradual concentration and thermal gradients occurred in the particle environment. The rate of particle growth is therefore unaffected by the macroscopic turbulence and the microscopic zones could be regarded as quasi-quiescent.

The factors which were found to affect particle growth were chemical reaction, nucleation and Brownian motion. The potential for nucleation requires that a particle must exceed a minimum radius in order to be stable. The value for this radius can be determined from the balance between the driving force from the free energy of condensation and the opposing force from the surface energy. Ulrich expressed this critical radius,  $R_c$  as:-

$$R_c = \frac{2\sigma}{\rho\Delta F}$$

- where  $\sigma$  is the surface tension,  $\rho$  the particle density, and  $\Delta F$  the free

energy of condensation. Particles of radius greater than  $R_c$  will grow whilst particles with smaller radii will evaporate. Using suitable values for the particles, the stable radius is calculated to be smaller than the size of an individual molecule. This result reflects the large free energy of condensation at the temperatures encountered (typically 2000°K). Thus nucleation does not present a barrier to particle formation. Experimental measurements by Ulrich established that chemical reaction occurred within the first 35  $\mu$ s, (this time being less than typical particle residence times of milliseconds to seconds). Hence, chemical reaction similarly does not present a barrier to the growth of particles.

Such small particles or droplets when initially formed behave as large gas molecules, assuming translational velocities determined by the flame temperature. Furthermore when the reaction times are short compared to the total formation period (as is typically the case<sup>3</sup>), growth becomes independent of the early history of the system and is determined by the frequency of Brownian motion collisions<sup>1,3</sup>. This frequency is in turn determined by the concentration of initial reactants and the flame temperature. The particles collide and fuse together forming one single larger 'particle' in the process. As the gas carries the particles downstream, they cool and are quenched. Collisions in regions of lower temperature can result in clusters of spherical particles, where the particles have partially fused together. See Fig. 4.1

Two criteria are found to be required to produce spherical particles<sup>2</sup>:-

- (1) The flame temperature must be greater than the melting point of the species involved (lower than for bulk material)
- (2) Relatively large mass flow rate is required ( $25 \times 10^{-5}$  mol/s), lower flow rates producing polyhedral particles

Both of the aforementioned conditions are satisfied in the deposition system constructed by the author, and observation of the deposited material verifies the spherical nature of the particles.

## 4.2 STRUCTURE OF UNSINTERED MATERIAL

In analysing the structure of the deposited material, one is concerned with the physical and chemical nature of the particles comprising the 'soot'. Such analysis relies on techniques such as x-ray diffraction, gas adsorption, infra-red (I-R) Spectroscopy, wet chemical analysis and direct particle observation using Scanning Electron Microscopy, (SEM) or Transmission Electron Microscopy, (TEM).

Edahiro et al<sup>4</sup> considered the deposition properties of the binary systems

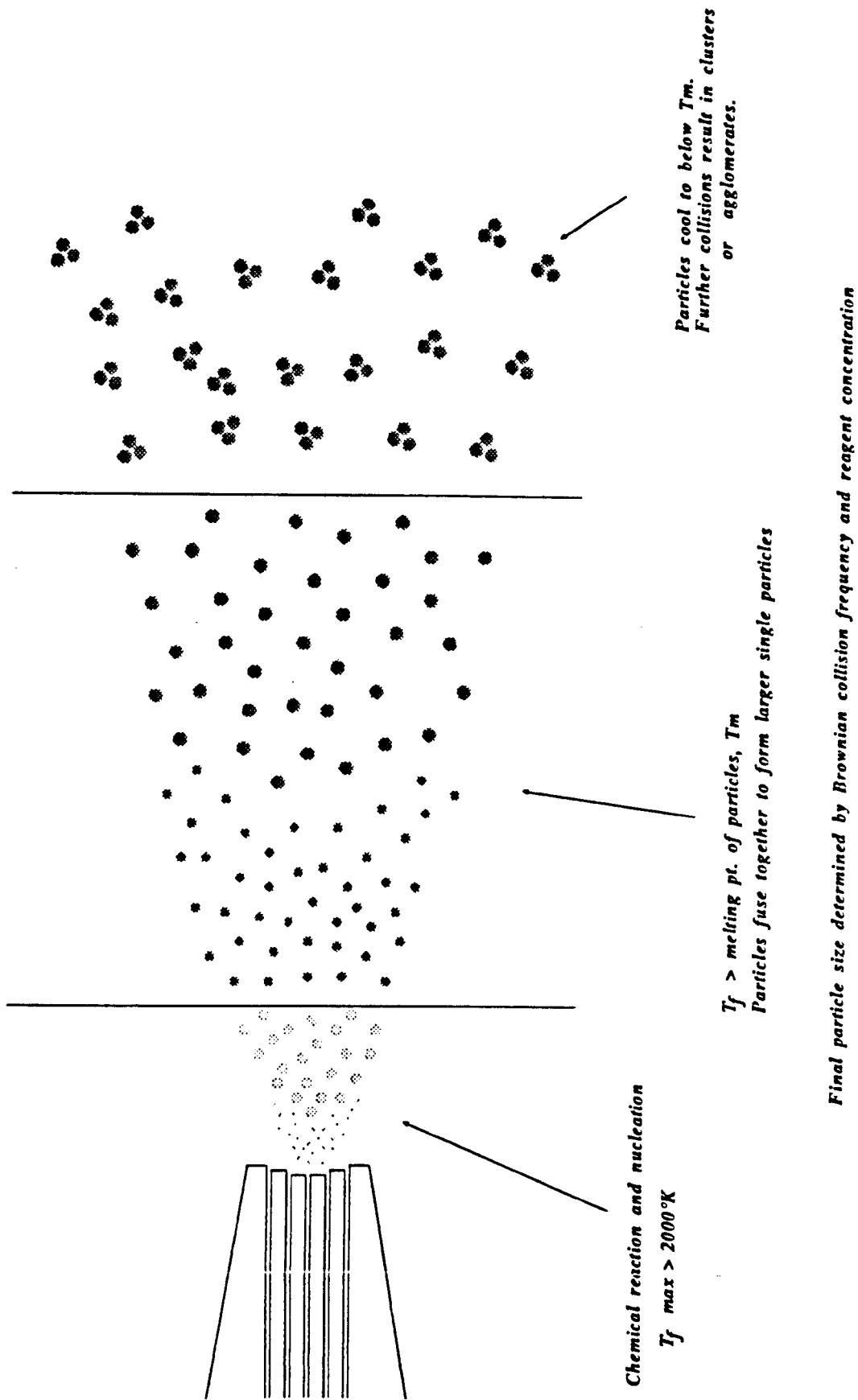


Figure 4.1 Schematic of torch indicating zones of interest.

$\text{SiO}_2/\text{GeO}_2$  and  $\text{SiO}_2/\text{TiO}_2$ , with emphasis on substrate temperature effects on particle morphology. Deposition was carried out on the exterior of a hollow tube, inside of which flowed a cooling gas to control the temperature of the tube. Analysis of the deposited material involved infra-red spectroscopy and X-ray diffraction. The substrate temperature ( $T_s$ ) was varied between  $200^\circ\text{C}$  and  $800^\circ\text{C}$ .

Non-crystalline  $\text{TiO}_2$  was produced for all substrate temperatures considered, chemically incorporated into the silica, and no dependence of dissolved  $\text{TiO}_2$  concentration on  $T_s$  was reported.

The  $\text{SiO}_2/\text{GeO}_2$ <sup>9</sup> system, showed a distinctive difference in behaviour. For substrate temperature below about  $400^\circ\text{C}$  the germanium component was deposited as a crystalline phase. Above  $500^\circ\text{C}$ ,  $\text{GeO}_2$  assumed an amorphous form dissolved in the silica, the concentration increasing for increasing  $T_s$ . Etching experiments carried out on the amorphous  $\text{GeO}_2/\text{SiO}_2$  mixtures suggested a structural model consisting of a silica particle covered with an amorphous  $\text{SiO}_2/\text{GeO}_2$  phase.

The difference in particle morphology between the two binary systems is attributed to the large difference in saturated vapour pressure of  $\text{TiO}_2$  and  $\text{GeO}_2$  at high temperatures<sup>11</sup>. This effect is also felt to be responsible for substrate temperature dependence of the  $\text{GeO}_2$  phase, the  $\text{GeO}_2$  vapour being transported to the substrate where it condenses, forming a crystalline phase. At higher substrate temperatures, there is insufficient cooling to allow such crystallisation.

More recently Potkay et al<sup>5</sup>, analysed the soot from VAD preforms produced from a standard system - ie one not modified to facilitate experiments. In this case, only the binary system  $\text{SiO}_2/\text{GeO}_2$  was studied. Soot analysis was carried out using techniques including x-ray diffraction and TEM.

In contrast to the earlier results by Edahiro, the presence of  $\text{GeO}_2$  crystallites was observed throughout the sample over regions having surface temperatures from  $300^\circ\text{C}$  to  $800^\circ\text{C}$ . Results also revealed  $\text{GeO}_2$  was not chemically combined with the  $\text{SiO}_2$  but was clearly segregated. The particle morphology proposed consists of  $\text{GeO}_2$  existing as both hexagonal microcrystals and as a shell of material covering a single  $\text{SiO}_2$  core. It was also reported that the exposure of the soot to water could alter the  $\text{GeO}_2$  concentration and even remove the germanium entirely.

However, excellent refractive index profiles are reported from consolidated VAD preforms and it can therefore be concluded that the presence of crystallites in the unsintered material does not signify poor fabrication. The hazard presented lies in the sensitivity of such crystals to humidity, which can result in preform degradation and opacity in fused boules.

The author has not uncovered results of studies on soot characterization on ternary systems such as  $\text{SiO}_2/\text{TiO}_2/\text{P}_2\text{O}_5$  or  $\text{SiO}_2/\text{GeO}_2/\text{P}_2\text{O}_5$  from VAD or flame hydrolysis which would apply specifically to this thesis. Work has been carried out by Wood et al<sup>10</sup> on the system  $\text{SiO}_2/\text{P}_2\text{O}_5/\text{GeO}_2$  produced by oxidation in an

MCVD process, however this study was concerned with the effluent gas composition and the characterisation of the soot has not yet been reported to the best of the authors knowledge. Further, since differences are reported between individual VAD systems<sup>4,5</sup>, it is not entirely clear whether the study of soot from a different process would clarify the situation.

### 4.3 CHEMICAL & PHASE CONSIDERATION

Up until now, the chemical aspects of the deposited, un-fused material have been considered. It is the aim of the following section to discuss the phase and chemical nature of the fused glass. This will be in terms of the physical states of the metal oxide dopants in the silica with reference to the phase diagrams of the metal oxide systems.

One should keep in mind that the inclusion of dopant species serves two distinct purposes:—

- (1) Raising the refractive index of the silica host glass, and
- (2) Lowering the temperature required to consolidate the soot

It is generally the case that the phosphorus pentoxide is used predominantly for the latter purpose whilst the other metal oxides considered (Ge and Ti) are used for the former. It is worth pointing out that while all of the dopant species used raise the refractive index of the glass (see Fig 4.2), the rates of change of index with doping level differ.

Since the refractive index change obtainable ultimately determines the dimensions of optical devices, and such index change depends on doping levels, it is instructive to consider the limits imposed by the solubility of dopants in the glass. Furthermore structural changes occur, such as changes in thermal expansivity, which can also impose doping level restrictions.

The information required can be obtained by studying the phase diagrams of the systems in question. Unfortunately to the best of the author's knowledge, no results have been published of work detailing the phase relations of the ternary systems  $\text{SiO}_2/\text{P}_2\text{O}_5/\text{GeO}_2$  or  $\text{SiO}_2/\text{P}_2\text{O}_5/\text{TiO}_2$  which are of interest. However, analysis of the binary systems  $\text{SiO}_2/\text{P}_2\text{O}_5$ ,  $\text{SiO}_2/\text{TiO}_2$  and  $\text{SiO}_2/\text{GeO}_2$ , on which information is available, can be used to gain some insight into the qualitative behaviour of the ternary systems. The desired result is to obtain mixed oxides existing as a single phase at the temperatures of interest.

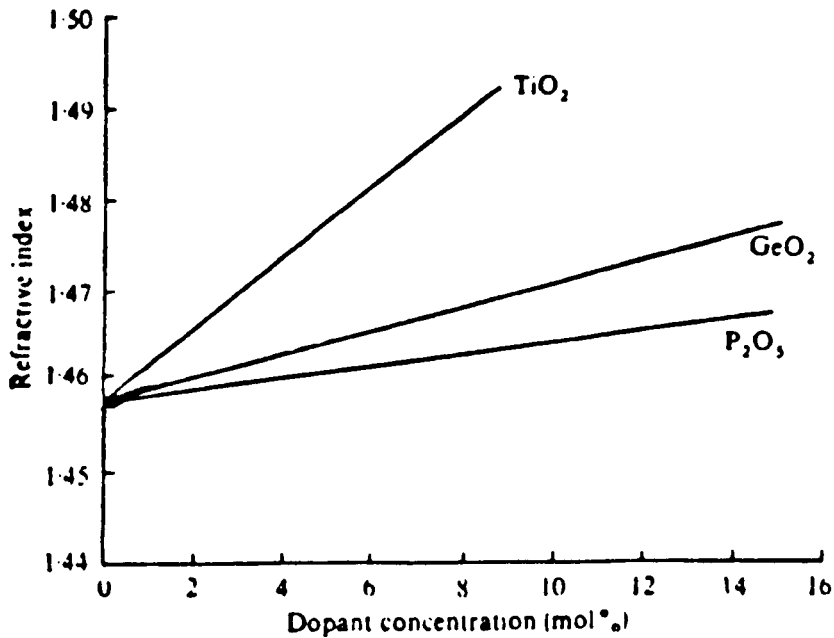


Figure 4.2 Variation of refractive index with dopants. After ref. 12

#### 4.3.1 SiO<sub>2</sub>/P<sub>2</sub>O<sub>5</sub>

As already outlined, phosphorus pentoxide primarily serves as a flux in the mixed oxide glass. The inclusion of P<sub>2</sub>O<sub>5</sub> reduces the temperature required to produce a single phase liquid solution. The phase diagram of this system is therefore considered in terms of the temperature required with increasing doping to produce the single liquid phase. This is clearly reflected in the behaviour of the *liquidus* line, being the boundary on a phase diagram between the solid and liquid phases. The lowest temperature at which a single liquid phase can be produced occurs at the *eutectic* point. See Fig 4.3. It should be stressed that the liquidus line represents the transition between solid *crystal* and liquid, and as such may not strictly apply to the glasses encountered. However it serves as a useful guide to describe the behaviour of the glasses.

Early work of Tien & Hummel<sup>13</sup>, studied the phase relations for this system. For our purposes it is sufficient to observe the behaviour of the liquidus line with increasing phosphorus pentoxide (P<sub>2</sub>O<sub>5</sub>) concentration. The inclusion of modest amounts of P<sub>2</sub>O<sub>5</sub> dramatically reduces the temperature required to liquify the material. The fabrication technique involved the mixing of diammonium orthophosphate acid, and acetone and heating in a silica crucible over long periods to allow equilibration between the silica from the crucible and the P<sub>2</sub>O<sub>5</sub>, followed by rapid quenching.

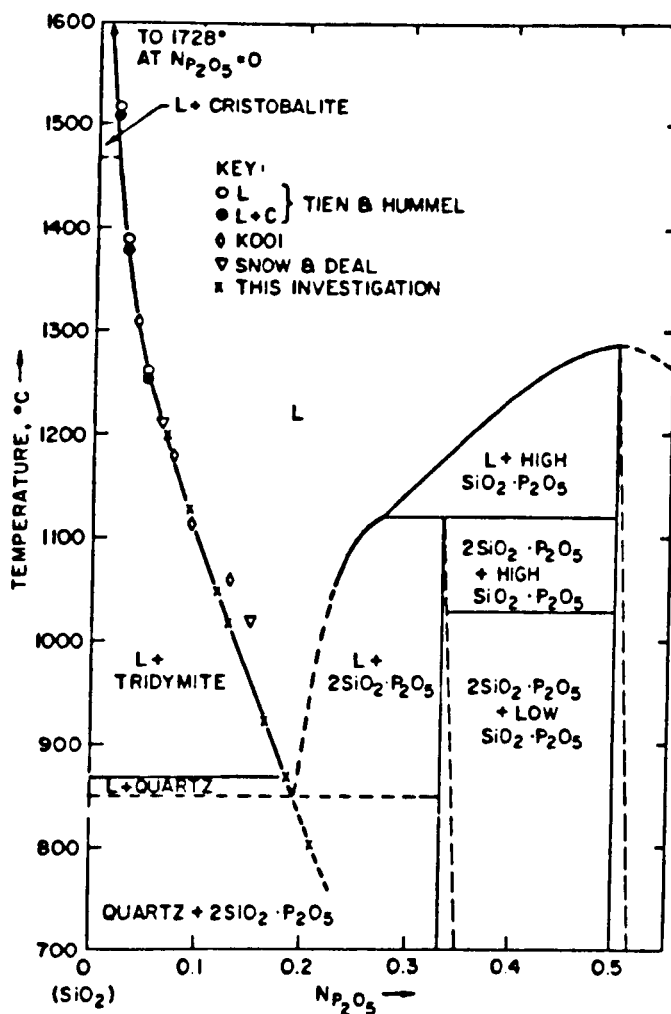


Figure 4.3 Phase diagram of  $SiO_2/P_2O_5$ . After ref 6.

Eldridge and Balk<sup>6</sup> used a different technique to study this system. Reaction of gaseous  $P_2O_5$  over silica for a wide range of temperatures and gas compositions produced results which generally corresponded to the liquidus curve of Tien and Hummel. The  $P_2O_5$  was produced by the oxidation of  $POCl_3$  vapour. Using this technique, the liquidus curve was extended to the lower temperature regions ( $<1100^\circ C$ ), extending Tien & Hummel's results

Much more than this need not be said. It is sufficient to say that even modest amounts of phosphorus pentoxide can dramatically lower the liquidus curve and for our purposes this translates into a lowering of the temperature required to consolidate the soot<sup>14</sup>.

The recipe used by the author gave  $P_2O_5$  concentrations of approximately 8 mol % . Using a fusing temperature of between  $1250^\circ$  and  $1300^\circ C$  it is clear that a single phase will result by rapidly quenching the melt.

### 4.3.2 SiO<sub>2</sub>/TiO<sub>2</sub>

DeVries, Roy and Osborne<sup>7</sup> studied the binary system SiO<sub>2</sub>/TiO<sub>2</sub> in an effort to clarify discrepancies in previous published reports. The equilibrium/quench technique was used in which the sample is held at a fixed temperature until equilibrium between constituents was achieved then rapidly quenched. A eutectic point (being the point to which the liquidus line converges) was found to occur at approximately 1550°C with 10.5 mol % TiO<sub>2</sub>.

Their results suggested that Ti<sup>4+</sup>, had a co-ordination of less than 6 in the glass. This result was later verified by Sandstrom et al<sup>15</sup> when studying the x-ray absorption spectrum of SiO<sub>2</sub> - TiO<sub>2</sub> mixtures prepared by flame hydrolysis.

Study of this phase diagram reveals a much narrower glass forming region lying between 0 % and 20 % of TiO<sub>2</sub>, see Figure 4.4. The precipitation of anatase (a crystalline form of TiO<sub>2</sub>) has been observed in glass samples prepared by flame hydrolysis<sup>16</sup> and sol-gel<sup>17</sup> at much lower levels than the phase diagram would suggest - 16.5 % and 10 % respectively for processing temperatures > 1450°C. Both authors concluded that the Ti<sup>4+</sup> ion was present as a network former in the low doping level range.

Such precipitation of solid material in the glass which leads to opacity, results in an upper bound on the doping level available.

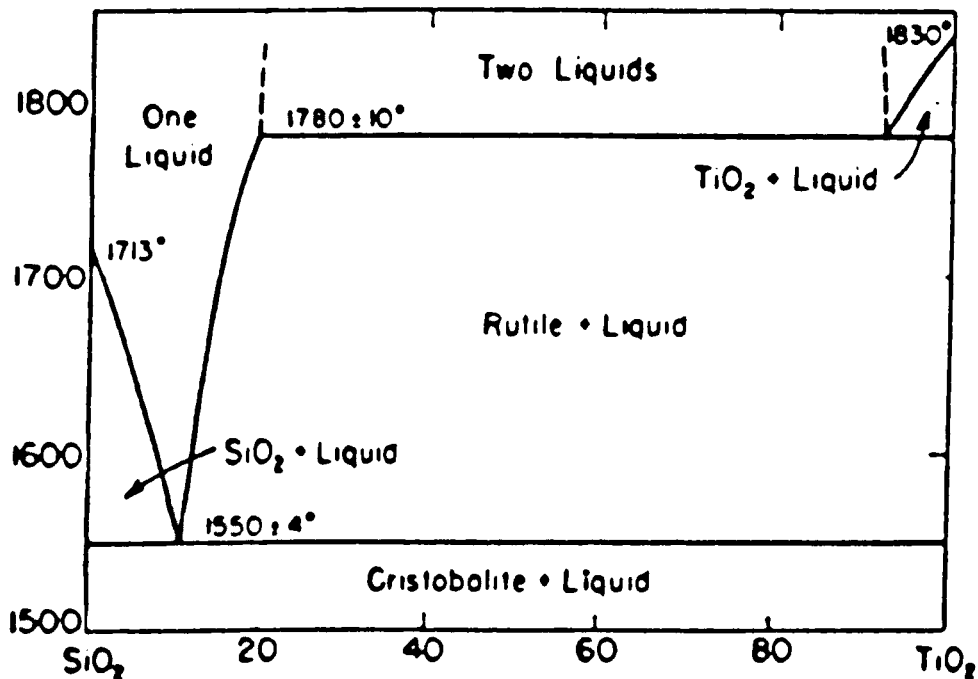


Figure 4.4 SiO<sub>2</sub>/TiO<sub>2</sub> Binary phase diagram. After ref. 7.

### 4.3.3 SiO<sub>2</sub>/GeO<sub>2</sub>

Analysis of the phase diagram<sup>8</sup> of this system reveals that a glass forming region exists for all doping levels of GeO<sub>2</sub>. In general the temperatures required for a single phase solution are lower than those for the SiO<sub>2</sub>/TiO<sub>2</sub> system. The structure of the binary glass is considered to consist of interconnected SiO<sub>2</sub>-GeO<sub>2</sub> tetrahedra<sup>18</sup> implying that Ge<sup>4+</sup> is a network former in the glass.

Huang, Sarkar & Schultz<sup>19</sup> studied this system using flame hydrolysis to fabricate VAD preforms of the mixed oxide glass. Their results indicated the reduction of fusing temperature required from 1450°C to 1000°C. Also reported was the reduction in viscosity with increased GeO<sub>2</sub> content, and more importantly, the order of magnitude increase in the thermal expansion coefficient. It is this increase which limits the doping levels available for planar optical waveguide films, formed by flame hydrolysis. This is due to the stresses generated by the mismatch in thermal expansivities between film and substrate upon quenching from the high temperatures encountered in sintering. Such stresses lead to cracking of the films<sup>20</sup>. This problem is not encountered in SiO<sub>2</sub>/GeO<sub>2</sub> films fabricated using techniques which do not involve such high temperature processing<sup>21</sup>.

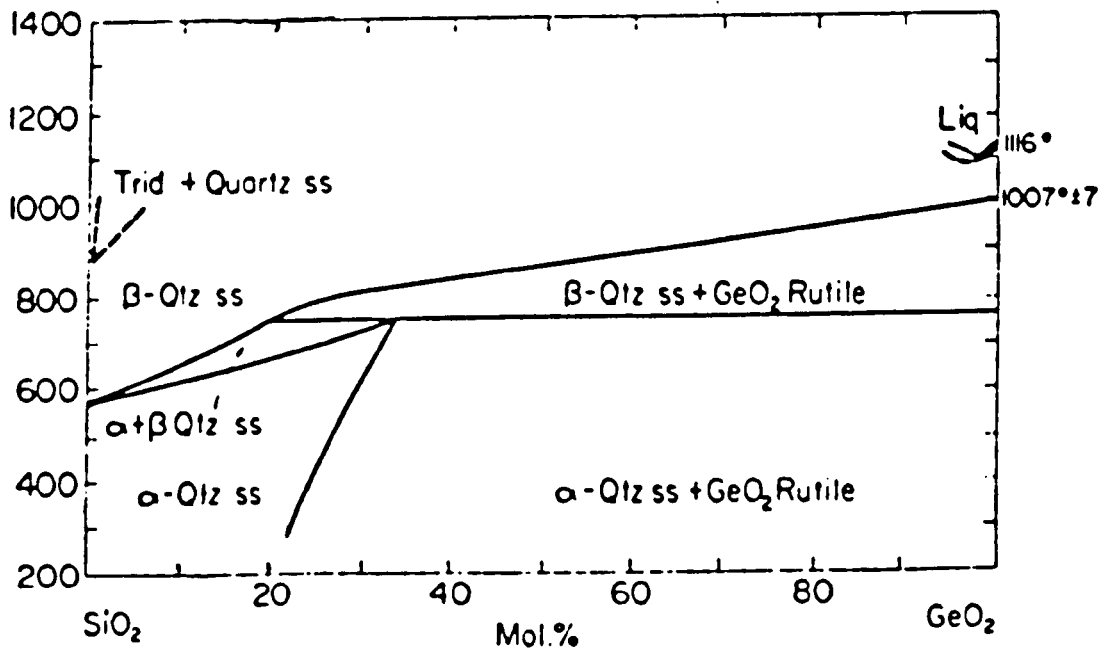


Figure 4.5 Phase diagram for SiO<sub>2</sub>/GeO<sub>2</sub>. After ref. 8.

#### 4.4 CONCLUSIONS

This chapter has discussed the synthesis of oxide particles in flames, detailing the mechanisms involved in nucleation and growth. The resulting particle size is found to depend on concentration of reagents present and on residence time in the flame, while particle shape is similarly dependent on reagent concentration and flame temperature.

The chemical nature of the deposited soot has been considered prior to consolidation. Such analysis is based on VAD fibre systems, in which particle production occurs by the same mechanism as for Flame Hydrolysis. The analysis involves the binary species  $\text{SiO}_2/\text{TiO}_2$  and  $\text{SiO}_2/\text{GeO}_2$ . The titanium is found to be chemically bonded to the silica in the particle; however a different structure is evident for  $\text{SiO}_2/\text{GeO}_2$  mixtures in which the silica particle is covered with a  $\text{GeO}_2$  shell which may contain microcrystals. No chemical analysis on particles from ternary systems has been reported to the author's knowledge.

Phase relations in the binary systems have been considered with a view to assessing limits on the doping of silica for  $\text{TiO}_2$  and  $\text{GeO}_2$ , and with regard to depression of the fusing temperature of the soot with  $\text{P}_2\text{O}_5$ . Doping in the binary system  $\text{SiO}_2/\text{TiO}_2$  is limited to levels of  $\text{TiO}_2$  below 10 wt % above which anatase precipitation occurs. Doping levels of  $\text{GeO}_2$  in planar  $\text{SiO}_2/\text{GeO}_2$  films are limited to levels dictated by the thermal expansion differences between film and substrate which causes film cracking when Flame Hydrolysis deposition is used. Modest levels of  $\text{P}_2\text{O}_5$  are found to dramatically reduce the required fusing temperature of the soot.

No analysis has been carried out on the ternary systems  $\text{SiO}_2/\text{GeO}_2/\text{P}_2\text{O}_5$  and  $\text{SiO}_2/\text{TiO}_2/\text{P}_2\text{O}_5$  due to the absence of literature on this subject. As a consequence of this, the quoted values of doping levels should only be regarded as indicative of a trend, and may differ in behaviour in the ternary system.

#### 4.5 REFERENCES

1. G.D. ULRICH  
Combust. Sci. and Technol., Vol. 4, 1971, pp47-57  
Theory of Particle Formation and Growth in Oxide Synthesis Flames
2. F. JULLET, F. LECOMTE, H. MOZZANEGA, S.J. TEICHNER,  
A. THEVENET, P. VERNON  
Faraday Symposia of the Chem. Soc., Nos. 6-8, 1972-3, pp57-62  
Inorganic Oxide Aerosols of Controlled Submicronic Dimensions
3. A.P. GEORGE, R.D. MURLEY, E.R. PLACE  
Ibid, pp63-77  
Formation of  $TiO_2$  Aerosols from the combustion supported reaction  
Of  $TiO_2$  and  $O_2$
4. T. EDAHIRO, M. KAWACHI, S. SUDO, S. TOMARU  
Jpn. J. Appl. Phys., Vol. 19, No. 11, Nov. 1988, pp2047-2054  
Deposition Properties of high silica particles in the flame hydrolysis  
For optical fibre fabrication
5. E. POTKAY, H.R. CLARK, I.P. SMYTH, T.Y. KOMETANI, D.L. WOOD  
J. Lightwave Tech., Vol. 6, No. 8, Aug. 1988, pp1338-1347  
Characterisation of soot from multimode Vapour Phase Axial Deposition (VAD)  
Optical fibre preforms
6. J.M. ELDRIDGE, P. BALK  
Trans. Metall. Soc. AIME, Vol. 242, Mar. 1968, pp539-545  
Formation of Phosphosilicate glass film on silicon dioxide
7. R.C. DEVRIES, R. ROY, E.F. OSBORN  
Trans. Brit. ceram. Soc., Vol. 53, 1954, pp525-540  
The system  $TiO_2/SiO_2$
8. E.C. SCHAFER, R. ROY  
Phase Diagrams for Ceramists, Ed. E.M. LEVINE, 1964, p140
9. M. KAWACHI, S. SUDO, N. SHIBITA, T. EDAHIRO  
Jpn. J. Appl. Phys., Vol.19, No. 2, Feb. 1980, ppL69-L71  
Deposition Properties of  $SiO_2-GeO_2$  particles in the Flame Hydrolysis Reaction  
For optical fibre fabrication
10. D.L. WOOD, K.L. WALKER, J.B. MACCHESNEY, J.R. SIMPSON,  
R. CSENCISITS  
J. Lightwave Tech., Vol. LT-5, No. 2, Feb. 1987, pp277-285  
Germanium chemistry in MCVD Process for optical fibre fabrication
11. G. V. SAMSONOV  
The Oxide Handbook, IFI PLENUM PRESS, N.Y.

- 12.K.J. BEALES, C.R. DAY  
 Phys. and Chem. Glasses, Vol. 21, No. 1, Feb. 1980, pp5–21  
 A review of glass fibres for optical fibre communications
- 13.T.Y. TIEN, F.A. HUMMEL  
 J. Am. Ceram. Soc., Vol. 45, No. 9, 1962, pp422–424  
 The system  $\text{SiO}_2\text{-P}_2\text{O}_5$
- 14.C.R. HAMMOND  
 Phys. and Chem. Glasses, Vol. 19, No. 3, 3rd June 1978, pp41–42  
 Fusion temperatures of  $\text{SiO}_2\text{-P}_2\text{O}_5$  binary glasses
- 15.D.R. SANDSTROM, F.W. LYTLE, P.S.P. WEI, R.B. GREGOR, J. WONG,  
 P.C. SCHULTZ  
 J. Non-Cryst. Solids, Vol. 14, 1980, pp201–207  
 Co-ordination of Ti in  $\text{TiO}_2\text{-SiO}_2$  glass by X-ray absorption spectroscopy
- 16.P.C. SCHULTZ  
 J. Am. Ceram. Soc., Vol. 59, No. 5–6, May–June 1976, pp214–219  
 Binary Silica–titania glasses containing 10 to 20 wt%  $\text{TiO}_2$
- 17.T. HAYASHI, T. YAMADA, H. SAITO  
 J. Mater. Sci., Vol. 18, 1983, pp3137–3142  
 Preparation of titania–silica glasses by the gel method
- 18.N. F. BORELLI  
 Phys. and Chem. Glasses, Vol. 10, No. 2, April 1969, pp43–45  
 The Infra-red spectra of  $\text{SiO}_2\text{-GeO}_2$  glasses.
- 19.Y.Y. HUANG, A. SARKAR, P.C. SCHULTZ  
 J. Non-Cryst. Solids, Vol. 27, 1978, pp29–37  
 Relationship between composition, density and refractive index for  
 Germania silica glasses
- 20.M. KAWACHI, M. YASU, T. EDAHIRO  
 Electron. Lett., Vol. 19, No. 15, 21st July 1983, pp583–584  
 Fabrication of  $\text{SiO}_2\text{-TiO}_2$  glass planar optical waveguides by flame hydrolysis
- 21.A.S. HUANG, Y. ARIE, C.C. NEIL, J.M. HAMMER  
 Appl. Opt., Vol. 24, No. 24, 15th Dec. 1985, pp4404–4407

The following chapter details the experimental techniques developed in the Flame Hydrolysis deposition of the doped silica films. Procedures adopted for the substrate preparation and techniques used for the assessment of the deposited material will be discussed, and factors affecting the homogeneity of the deposited films will be highlighted. The methods used for film fusing will be mentioned, including details of equipment designed for this purpose. Appraisal of the film fusing and of fused films will be presented using pictures taken with a Hitachi S600 Scanning Electron Microscope (SEM) and investigation into the effects of fusing atmospheres will be included. Characterisation of films in terms of fused film thickness with torch traversal will be examined and doping levels achieved for various halide flow rates will be given.

It should be stressed at this point that the main aim of the author was to find a suitable 'recipe' which yielded inclusion free (bubbles etc), homogeneous films of the desired thickness, which would fuse at a target temperature of 1250°C – 1300°C, such a temperature having been chosen to minimise substrate bowing and warping. Once such a recipe had been empirically determined, primarily involving SiCl<sub>4</sub>/PCl<sub>3</sub> ratios, it remained reasonably fixed while other factors, such as TiCl<sub>4</sub>/GeCl<sub>4</sub>, doping levels were varied. The effects of such secondary doping of silica will be discussed in terms of the limitations on doping levels imposed by film degradation for both TiO<sub>2</sub> and GeO<sub>2</sub> species.

Many of the results are described in general terms, indicating observations made during deposition and on deposited films. The techniques adopted to minimise or solve the problems encountered also may appear general. This reflects the aim of producing films which could be used for further processing. As a consequence, detailed investigation into the causes of the observed phenomena was not carried out beyond the level necessary to surmount the problems encountered.

The effects on refractive index of such doping will be detailed in chapter 6, along with an assessment of the optical waveguiding properties of the planar films.

### 5.1 SUBSTRATE PREPARATION

The substrate type most often used was a 30 mm diameter, 1mm thick disc. The disc type was polished 'Homosil' grade silica, which is a high purity natural fused quartz

Substrate preparation fell into two categories, depending on the nature of the experiment being performed. If characteristics of the deposited soot and sintering

stages were being investigated, or aspects where the optical quality of the resulting film were not being considered, then no substrate cleaning was necessary. If however, experiments were being performed involving the optical quality of the film, then the following cleaning procedure was employed:-

- 1 Wash substrates individually with soap and water using a sponge
- 2 Five minutes in soapy water in the ultrasonic bath (u.b.)
- 3 Rinse in de-ionised water
- 4 Five minutes in de-ionised water in u.b.
- 5 Rinse in ACETONE
- 6 Five minutes in ACETONE in u.b.
- 7 Rinse in METHANOL
- 8 Five minutes in METHANOL in u.b.
- 9 Final rinse in methanol
- 10 Blow dry with nitrogen
- 11 Dry on hotplate

A silica basket, purloined from a soxhlet set, capable of holding six such discs at a time was used throughout the cleaning procedure, and all such cleaning was carried out in a class 100 cleanroom environment. Visual inspection of one cleaned sample from each batch was carried out using a Differential Interferometer on a Nikon microscope which would highlight any particulate contaminants remaining.

## 5.2 DEPOSITION PROCEDURE

The deposition procedure used was developed to ensure the safe operation of the fabrication system while providing a flexible method of film production. The procedure is as follows:-

- 1 Switch on stepper motor control unit
- 2 Switch on computer and load fabrication program
- 3 Input the pertinent data; ie starting position of torch, number of traversals, traversal rate and turntable rotation rate used to warm up the turntable
- 4 Set the desired flow conditions for the halide reagents using the potentiometers and digital voltmeter readings on the control panel
- 5 Switch on the gas scrubber water supply
- 6 Open the hydrogen and oxygen valves on the gas bottles
- 7 Open the valve on the hydrogen flowmeter slowly and ignite the torch,

- and close the hatch on the deposition chamber
- 8 Open the valve on the oxygen flowmeter and set both flow rates to the desired levels
  - 9 Set the turntable and torch in motion by pressing the relevant computer keys, and thus warm up the turntable
  - 10 Once complete, turn down the H<sub>2</sub> and O<sub>2</sub> flow rates, extinguishing the torch by closing the H<sub>2</sub> flowmeter valve first
  - 11 Input deposition data
  - 12 Place substrates on warmed turntable
  - 13 Ignite the torch as before and set flowrates for H<sub>2</sub> and O<sub>2</sub>
  - 14 Throw the toggle switches controlling the valving for the carrier gas flows through the halide bubblers. The relevant chlorides are thus transported to the flame in the predetermined quantities. The flame colour changes when the hydrolysis begins, and the flame grows in length. Once equilibrium is obtained (usually <1 minute), the turntable and torch can be set in motion. The torch moves to the pre-set starting position and begins the traversal/deposition. Once complete:–
  - 15 Switch off halide vapour transport and allow flame to return to original colour (again generally <1 minute) to ensure reaction of any halides left in the pipeline
  - 16 Close the H<sub>2</sub> and O<sub>2</sub> valves on the flowmeters, switching off the hydrogen first
  - 17 Close the H<sub>2</sub> and O<sub>2</sub> valves on the gas bottles
  - 18 Switch off scrubber water supply, computer and stopper motor controllers
  - 19 Allow the turntable time to cool (approx 5 minutes)
  - 20 Remove substrates for fusing

Typical deposition parameters used are:–

(1) Turntable warm up:–

H<sub>2</sub>/O<sub>2</sub> flowrates at 50mm/50mm on flowmeters, corresponding to 16 litres/minute and 8 l/min respectively.

Traversal data:–

25mm to starting position for the torch

65mm traversal length at 65mm/min with turntable rotation at 30 revs/min, carried out for two layers (traversal to turntable centre and back to starting position).

**(2)Deposition:-**

H<sub>2</sub>/O<sub>2</sub> flowrates as before.

Halide flowrates (for Germanium as an example):-

SiCl <sub>4</sub>	75mV	on the DVM	corresponding to	150 sccm's
PCl <sub>3</sub>	400mV	"	"	160 sccm's
GeCl <sub>4</sub>	250mV	"	"	100 sccm's

— the quoted values being for the flow rate of carrier gas through the bubblers.

Traversal data as for turntable warm up with the appropriate number of layers to give the desired film thickness.

**5.3 ASSESSMENT OF DEPOSITED MATERIAL:  
PROBLEMS & SOLUTIONS**

Once the substrates are removed from the turntable after deposition, the surface coating is visually inspected to assess the homogeneity of the deposited film. This is carried out by looking perpendicularly through the film and substrate with the sample lit from behind. Such inspection is useful for thin films (<8 layers), and reveals any shadowing or darker areas, indicative of an inhomogeneous layer.

Such shadowing is felt to be a consequence of local temperature variations leading to thermophoretic<sup>1,2</sup> effects, and a simple experiment was attempted to test this hypothesis. This involved a long substrate ( a 20mm wide, 3' long section from a 3' silica disc) which was placed on the turntable in such a way as to overhang the disc recesses (see Fig. 5.1). This would result in a temperature difference during deposition over the substrate, with the areas overhanging the disc recesses being at a higher temperature than that in contact with the turntable, due to the greater thermal conductivity of the aluminium turntable as compared with the air below the overhanging regions.

A standard deposition was carried out, the observed result, of which was a dramatic demarkation of the boundaries between the turntable top and the disc recesses (see Fig. 5.2), in which more material was deposited on the part of the substrate in contact with the aluminium turntable.

Whilst such an effect, indicating a temperature dependence on the amount of material deposited, may be exploited as a secondary means of layer thickness control by using a separate turntable heater, it was felt at this stage that the minimisation

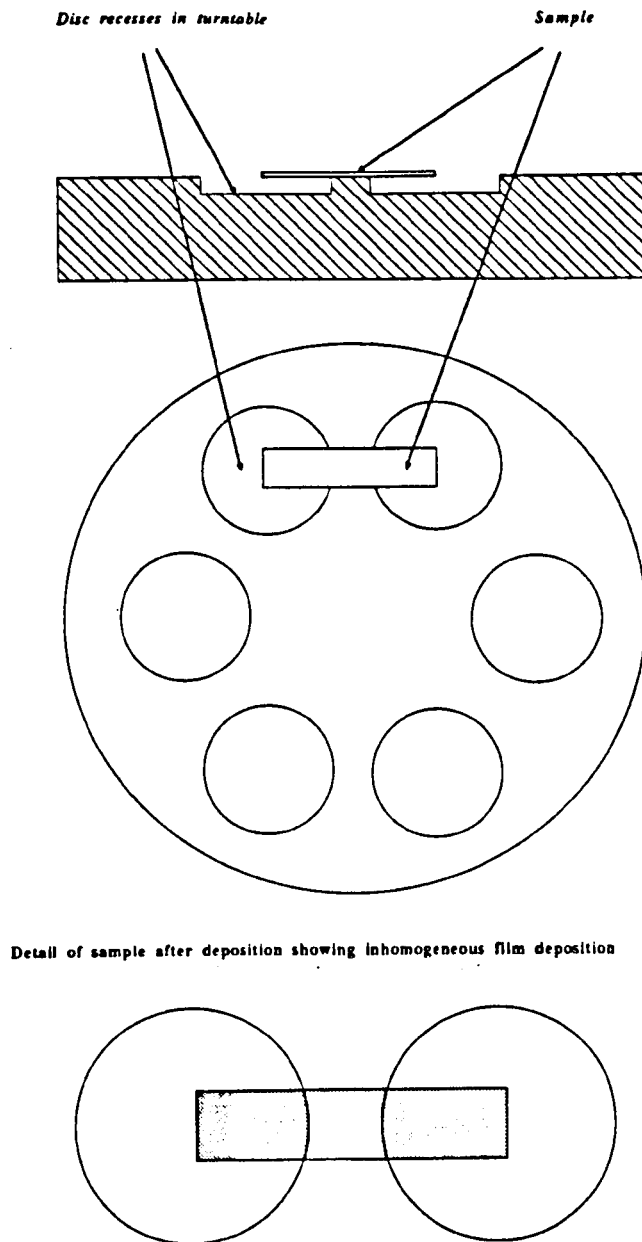


Figure 5.1 Schematic detailing sample position on turntable

of this effect was the desired aim. In order to solve this problem, two possibilities were considered: one, increase the torch/substrate temperature separation ( $\Delta T_S$ ), resulting in a cooler substrate, or, decrease the torch/substrate separation to produce a higher substrate temperature. See figure 5.3. Both possibilities were attempted. With greater  $\Delta T_S$ , shadowing was still evident and film degradation occurred, sometimes within minutes of removing the sample from the turntable for  $P_2O_5$  and  $P_2O_5 / TiO_2$  doped films. A more detailed discussion of the film degradation will be included in the section on  $SiO_2/P_2O_5/TiO_2$ . Reduced  $\Delta T_S$  resulted in more stable films with less shadowing. Figure 5.4 gives some examples of the torch positions used and the results obtained, and figure 5.5 illustrates the film degradation.

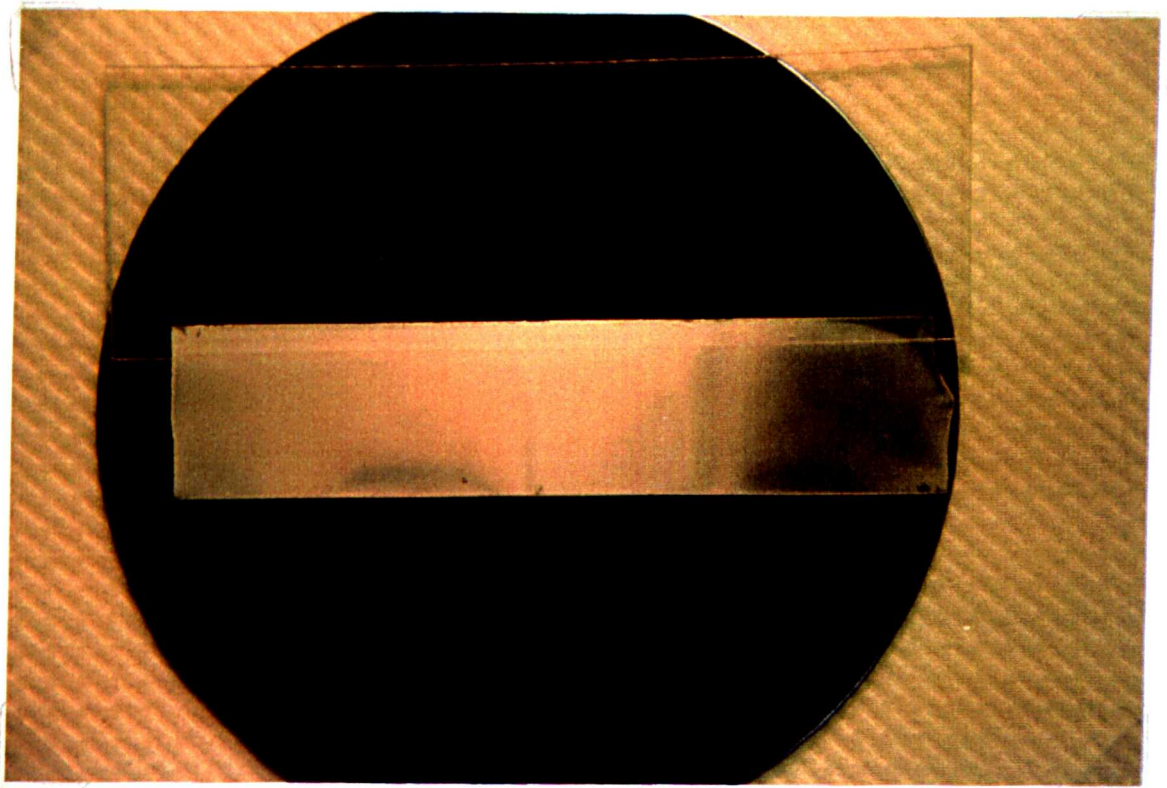


Figure 5.2 Photograph illustrating inhomogeneous deposition

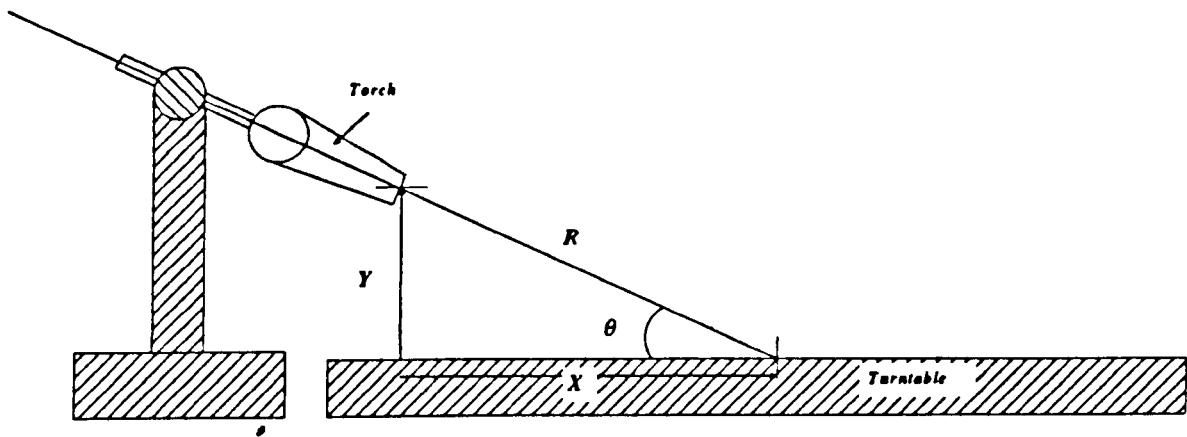


Figure 5.3 Schematic of torch position.

Torch Position			H <sub>2</sub> /O <sub>2</sub> Flow rates l/min		Traversal Rates mm/min	Film Shadowing		Film Deg		Comments
X mm	Y mm	θ °	H <sub>2</sub>	O <sub>2</sub>		Yes	No	Yes	No	
80	21	25	43	43	60	/		/		Greatest degradation
80	21	25	50	50	60	/		/		Less deg. than above
56	25	18½	50	50	60		/	/		No buffer layer
50	22	18½	43	40	45		/		/	Slower traversal
52	20	18½	50	50	60	/			/	Buffer layer

Figure 5.4 Table giving values of X, Y, and θ with sample degradation

It should be pointed out that the film degradation occurred for P and Ti/P doped films and no such degradation<sub>34</sub> was observed with Ge/P doped films.

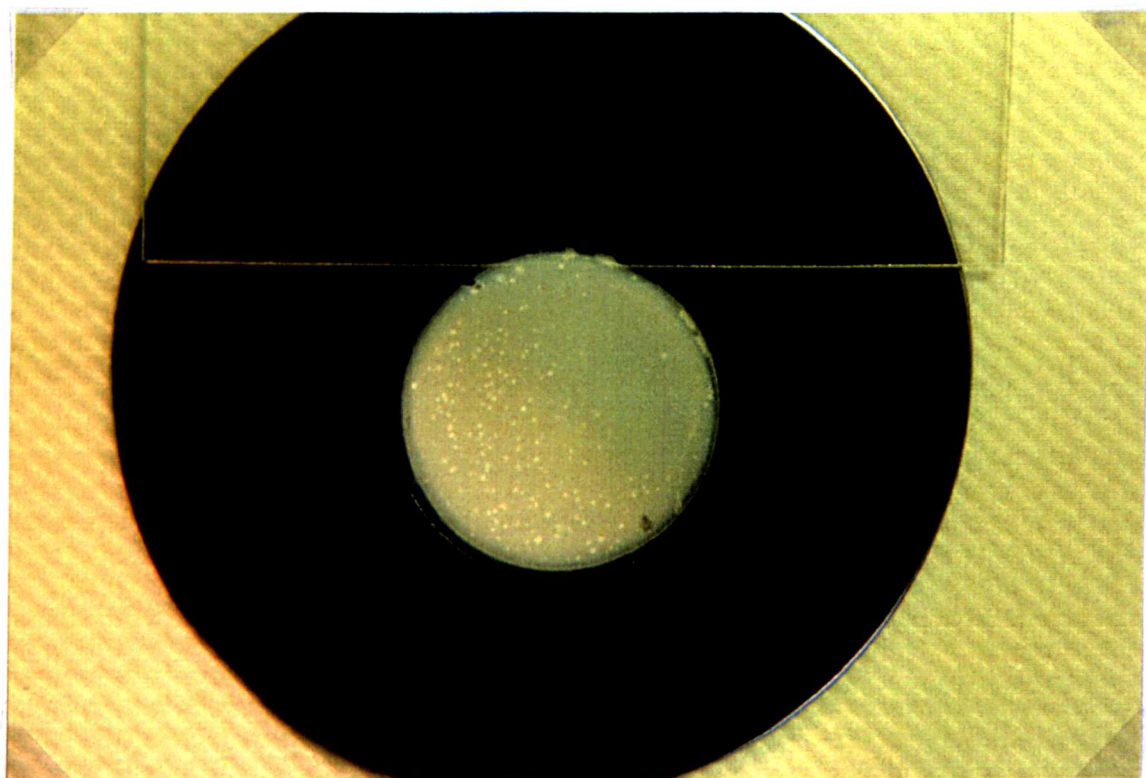


Figure 5.5 Photographs illustrating film degradation

Once a suitable torch position was found no further reduction in  $\Delta T_S$  was carried out. It was felt that any further reduction may lead to loss of phosphorus pentoxide through over heating of the substrate. Furthermore, a temperature could be reached which would lead to in-situ fusing, which would then not allow accurate control over the fusing stage.

#### 5.4 FURNACE CONSIDERATIONS

The furnace employed for the consolidation of the deposited soot was a Severn Science Limited (SSL) Model SC 105/4.5/1600, the quoted temperature range being up to 1600°C and the working tube diameter being 105 mm. A silica liner was used inside a  $\text{SiO}_2:\text{Al}_2\text{O}_3$  ceramic furnace tube. This reduced the working tube diameter to 90 mm. The furnace was profiled using a Platinum/Platinum 13 % Rhodium thermocouple encased in an alumina sheath. Profiling was carried out for three set temperatures values - 1300°C, 1400°C and 1450°C. See Figure (5.8). The results indicate a hot zone of > 10 cm in which there is less than a 5°C variation in temperature. It is also evident that there is > 120°C drop between the set point temperature on the controller and the value of measured temperature. This temperature difference increased to 150°C with a set temperature of 1450°C.

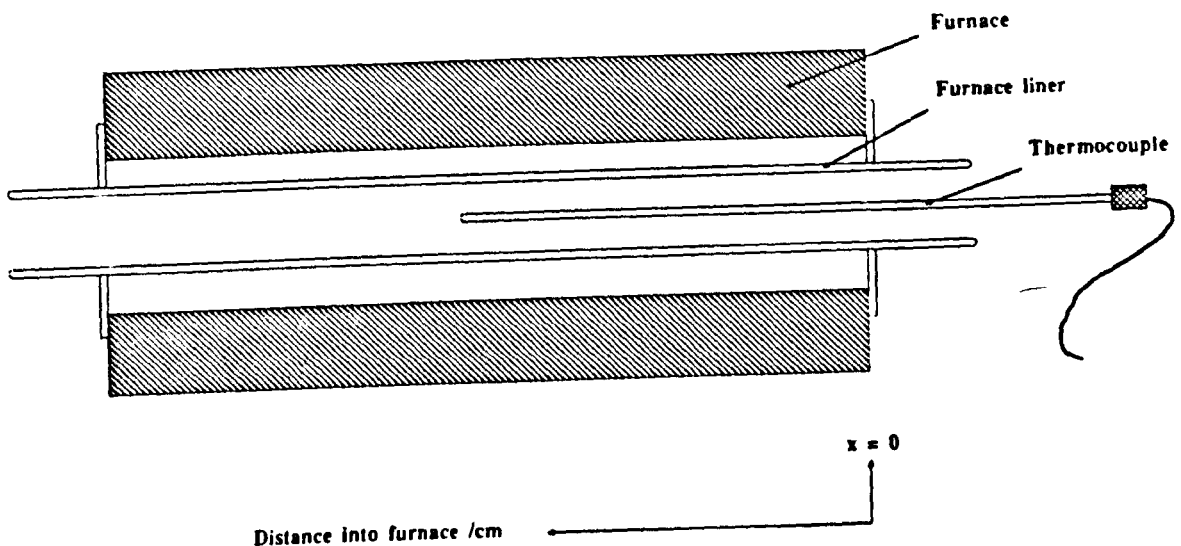


Figure 5.6 Schematic of furnace & profiling arrangement

Distance into Furnace/cm	Set Point Temperature/°C		
	1300	1400	1450
0	518	409	418
5	623	641	626
10	757	774	780
15	888	944	929
20	1006	1085	1085
25	1061	1168	1174
30	1124	1216	1232
35	1160	1243	1273
40	1169	1261	1292
45	1174	1264	1299
46	1174	1263	1297
47	—	1263	1298
48	—	1262	1293
49	—	1260	1290
50	—	1254	1290

Figure 5.7 Thermal profiling data

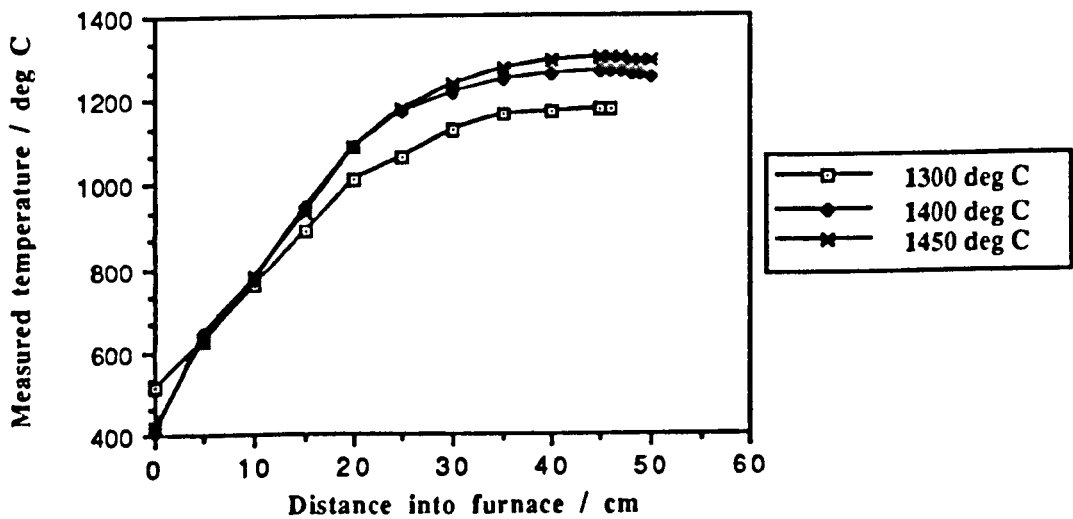


Figure 5.8 Graphed thermal profiling data

Profiling was also carried out to assess the effect of a gas flow through the furnace. The set point temperature was 1400°C, and profiling measurements were carried out for the case of no atmosphere (other than static air) and for a typical fusing atmosphere of 1l/min of He through water, (Fig. 5.9).

Distance into furnace/cm	Furnace Atmosphere	
	Air	He
0	409	502
5	641	611
10	774	767
15	944	941
20	1085	1070
25	1168	1143
30	1216	1203
35	1243	1231
40	1261	1252
45	1264	1261

Figure 5.9 Thermal profiling data with furnace atmosphere

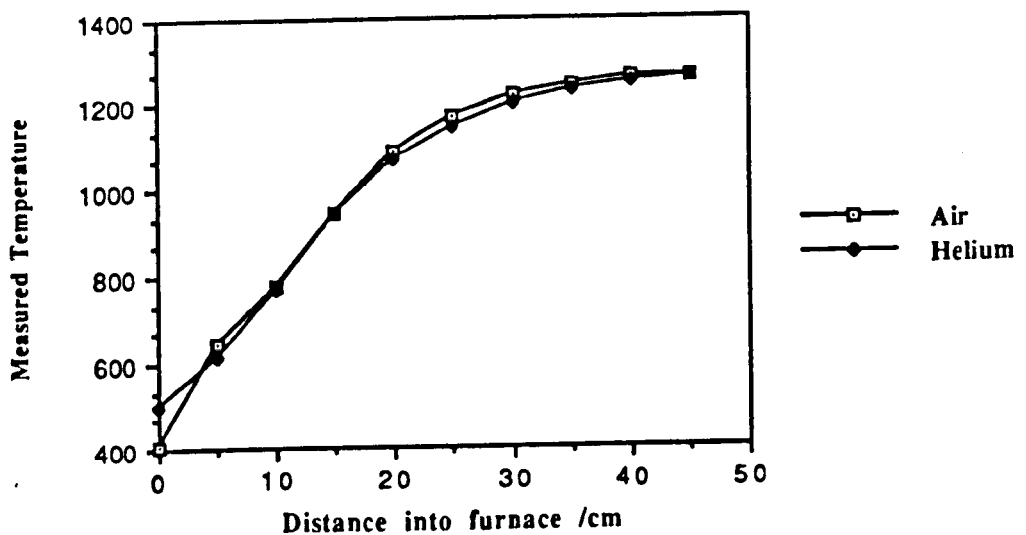


Figure 5.10 Graph of profiling data with a furnace atmosphere

It would appear from this result that a fusing atmosphere makes little difference to the hot zone temperature for the gas flow rate used.

The standard fusing procedure adopted consisted of ramping up the furnace and allowing equilibrium to be reached over a period of four to five hours. The hot zone temperature was measured for every fusing attempt.

A silica 'table' was designed as a substrate support during fusing. This consisted of a 3" diameter x 5mm thick silica disc into which was machined three 32 mm diameter recesses to hold the samples during loading and unloading into the furnace. Silica legs joined to the machined disc were used to complete the table and hold the table top at the level of the furnace centre.

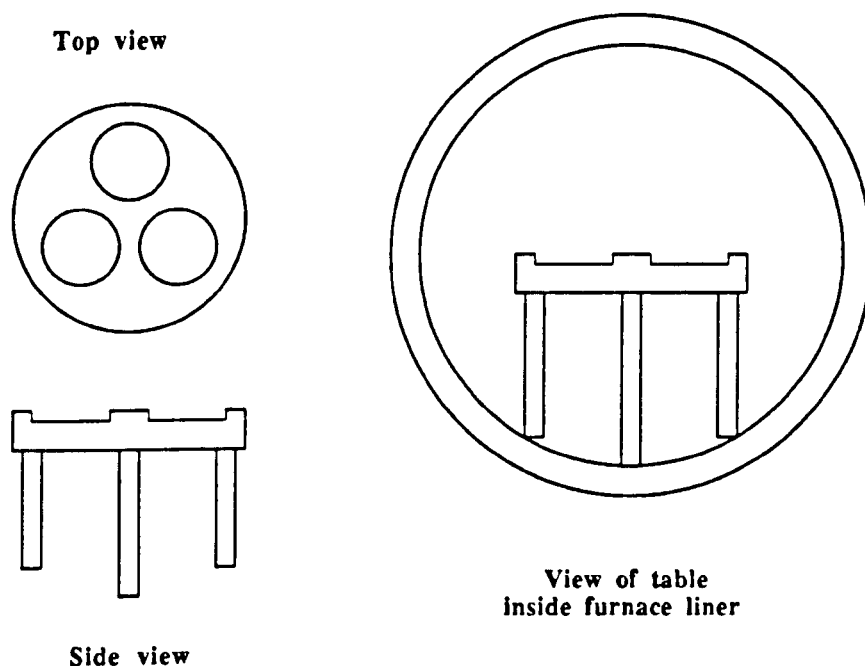


Figure 5.11 Schematic of furnace table design

Softening of the table resulting in bowing and warping limited its useful life and replacements were required. For substrates of a different shape, a 3" silicon wafer was placed on top of the silica table. This technique was also adopted to extend the useful life of the silica table.

The temperature required for fusing was a function of doping, similarly the time required for complete fusing. Values typically used were, a temperature of

1275°C and a fusing time of 60 minutes, ( such values having been empirically determined ).

### 5.5 LAYER THICKNESS CHARACTERISATION

A series of depositions was carried out to characterise the physical thickness of consolidated soot for various layer traversals during deposition. Standard deposition parameters were used and were as follows:—

Halide	Flow rate/sccm
SiCl <sub>4</sub>	150
PCl <sub>3</sub>	150
GeCl <sub>4</sub>	40

Figure 5.12 Halide parameters used in layer thickness characterisation

Traversal rates used were:— 65 mm traversal distance at 60 mm/min on 30 revs/min. The fusing temperature used was 1275°C for 60 minutes.

Six samples were placed in the disc recesses on the small turntable and a coated sample was removed after every two layers. Hence layer thickness was investigated for up to 12 layers of deposited soot.

Upon removal from the turntable, an area of soot was removed from the coated disc using a razor blade scraped over the sample. The now partially coated sample was then sintered as usual. After consolidation, talystep measurements were made at three places along the scored edge to obtain the fused layer thickness.

The same procedure as outlined was repeated for two other depositions in which the traversal rate was varied. The results obtained are presented in figure 5.13.

Similar detailed investigation was not carried out for titanium doped samples, since it was felt that the thickness would be primarily determined by the SiCl<sub>4</sub> flow rate, (since SiCl<sub>4</sub> has the highest vapour pressure of the chlorides used) and the traversal rate used during deposition.

Two drawbacks of using this procedure to measure the film thickness were

highlighted during the talystep measurements:-

- (1) During fusing, shrinkage occurred in the film which resulted in a lip of glass being formed at the edge of the scored area, see Fig. 5.14. One had to ensure therefore that during talystep measurements a sufficiently long traversal length was used to reach the lip-base on the unscraped film side.
- (2) Care had to be taken to ensure complete removal of the soot from the substrate, otherwise any remaining material would affect the talystep results in such a way as to indicate a thinner film than had actually been deposited.

No. Layers	Traversal Rate mm/min	Thickness/ $\mu\text{m}$			Average / $\mu\text{m}$
		Edge	Centre	Edge	
2	60	2.64	1.4	1.64	1.89
4		4.47	4.06	3.77	4.10
6		5.22	6.93	5.64	5.93
8		7.99	7.4	7.55	7.64
10		10.39	10.12	9.82	10.11
2	45	2.62	3.19	2.52	2.78
4		6.74	5.68	4.48	5.65
6		8.04	8.64	9.89	8.86
8		13.93	10.61	13.52	12.70
10		17.70	21.91	16.82	18.81
2	75	1.31	1.68	1.39	1.46
4		2.97	3.1	3.44	3.17
6		5.76	5.56	5.70	5.64
8		6.54	7.06	7.48	7.03
10		10.68	10.21	10.85	10.58

Figure 5.13 Data from talystep measurements

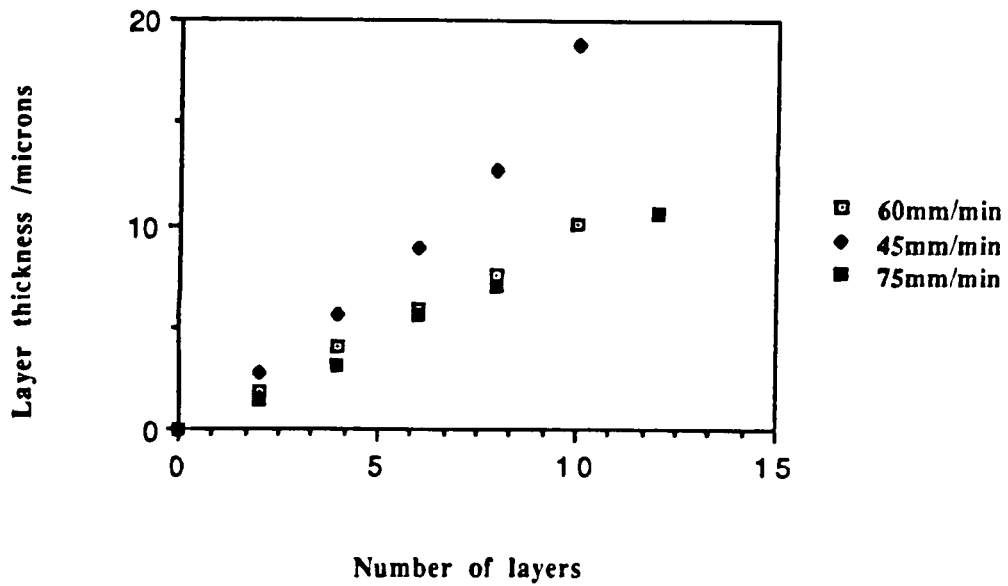


Figure 5.14 Graph of talystep data showing deposited layer thicknesses obtained for various numbers of torch traversals.

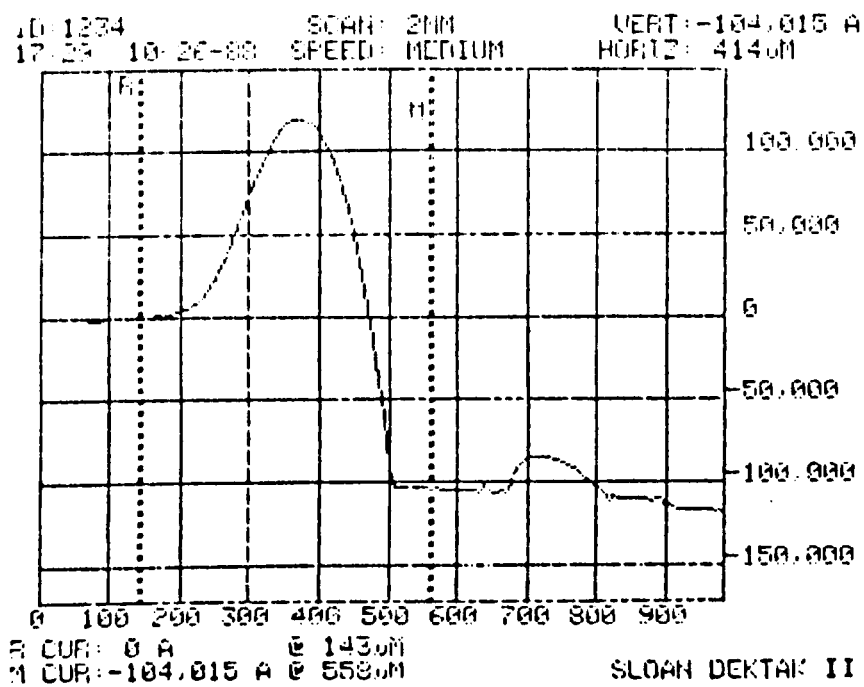


Figure 5.15 Example of talystep measurement, showing lip at scraped edge.

## 5.6 ASSESSMENT OF FUSING AND/OR FUSED MATERIAL

Once again, the description of the film fusing stages and of the fused films is presented in general terms, the main factors found to affect the film quality being presented and the solutions to such problems being described.

As for the deposited material, the fused or partially fused film is visually inspected both perpendicular to the film and in this case, also at grazing incidence. Such observation reveals inhomogeneties, such as the presence of a colouration, pinholes, cracks or surface mottling. If no such blemishes are observed then the film is considered suitable for optical assessment under an optical microscope and, if suitable, for waveguiding assessment and characterisation.

Some of the blemish types appear to be dependent on doping type, whilst others are common to all film types.

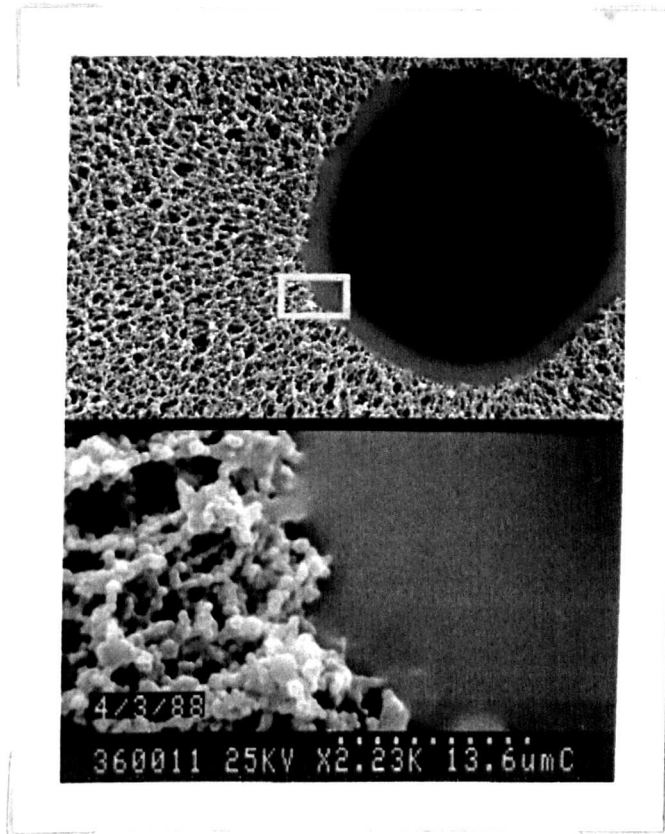
The appearance of a blue tint and areas of 'rosette' shaped blemishes in fused films is common to the  $P_2O_5$  and  $TiO_2/P_2O_5$  co-doped silica films. (See Figure 5.5). In practice,  $SiO_2/TiO_2$  films could not be fused at the target temperature of  $1250^\circ-1300^\circ C$ , since the viscosity was too high and as such these films could not be assessed.

Cracking was more common in  $GeO_2/P_2O_5$  doped silica - as expected, due to the difference in thermal expansion between film and substrate - with higher doping levels of  $GeO_2$  ( $> 30$  sccm's for a 10 layer film). Such problems are discussed further in the sections on individual film types.

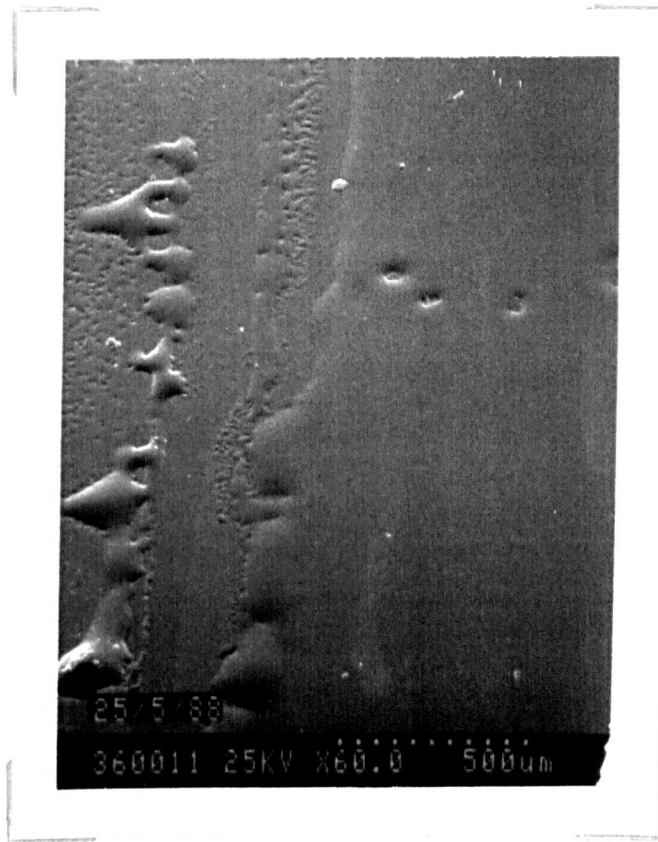
Fusing problems common to both film types included unfused areas at substrate edges, uneven fusing and generally poor film quality with high doping levels ( $> 120$  sccm's). Film shrinkage and trapped pore gas also became a problem in thicker films ( $> 12$  layers). See Fig. 5.16

The solutions to some of the problems are straightforward; slower fusing in a He atmosphere for thicker films to minimise trapped gas; use of 'clean' deposited films, ie, free from physical damage to soot, to ensure even shrinkage; ensuring soot deposition over the substrate edges to facilitate fusing at substrate edges. The problem of poor film quality is more difficult. In such cases further assessment using the SEM is carried out to try to find clues as to the cause of the fusing problem. Such problems will be discussed in the sections on film types.

Assessment techniques for *partially* fused material are virtually the same as those for the fused material. In such cases homogeneity in the white colour of the soot and high reflectivity at grazing incidence are indicative of even fusing.



(a)



(b)

Figure 5.16 Detailing (a) uneven fusing, (b) surface shrinkage

### 5.6.1 THE SYSTEM $\text{SiO}_2/\text{P}_2\text{O}_5/\text{TiO}_2$

The  $\text{SiO}_2/\text{P}_2\text{O}_5/\text{TiO}_2$  films were initially fabricated with a recipe consisting of 300 sccm's  $\text{SiCl}_4$  and 160 sccm's  $\text{PCl}_3$  to which was added 10 sccm's  $\text{TiCl}_4$ . This mixture deposited directly onto a silica substrate was fused at  $1250^\circ\text{C}$  to give a clear film. Energy dispersive x-ray analysis (EDAX)<sup>3</sup> gave the titanium doping level as 0.2wt %. Doubling the  $\text{TiCl}_4$  flow rate resulted in a perfectly fused film with a blue tint. (See Figure 5.17). This tint was found to be independent of the fusing temperatures ( $1250^\circ\text{--}1300^\circ$ ), and fusing times (30mins to 4 hours) but could be fused into a clear glass with an oxy-acetylene welding torch. However, such treatment resulted in the substrate warping to such an extent that it was rendered unsuitable for further processing.

Spectroscopic results obtained from a Perkins Elmer Lambda 9 Spectrometer indicated a broadening of the ultra-violet (uv) absorption edge (see Fig 5.17). Data points from the spectra were used to plot a graph of log absorption vs  $(\text{wavelength})^{-2}$  (see Fig 5.18). The straight line dependence obtained indicating that the tint is due to Rayleigh/Mie scatter<sup>4</sup>. Examination in the SEM revealed an essentially featureless surface, and certainly nothing which would cause such scattering.

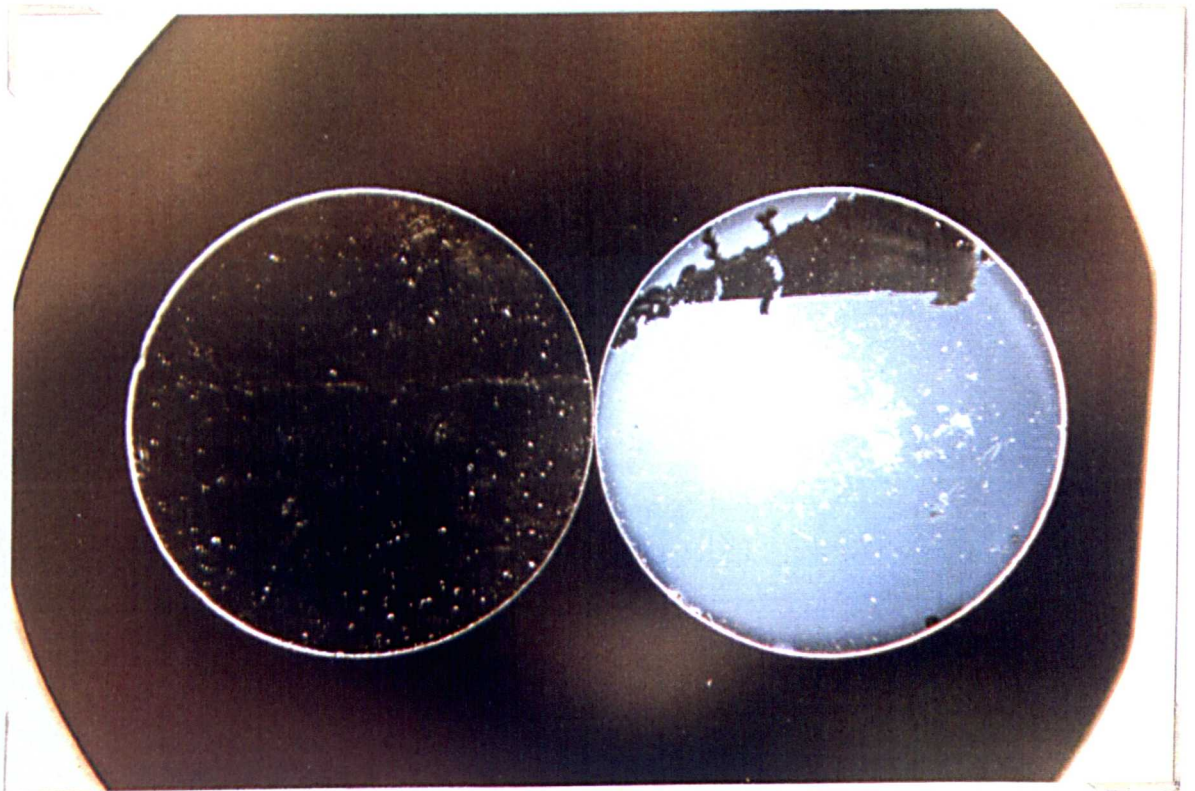


Figure 5.17 Consolidated films, (a) Clear film, (b) Film with blue tint

Wavelength/nm	Absorption
360	0.169
380	0.139
400	0.119
420	0.105
440	0.094
460	0.085
480	0.078
500	0.073
520	0.068
540	0.064
560	0.060
580	0.057
600	0.055
620	0.053
640	0.051
660	0.049
680	0.048
700	0.046

Figure 5.18 Table of spectroscopic data

Using an optical microscope in transmission through the sample a structure akin to that observed in phase separated glasses<sup>5</sup> was revealed. Equally possible was the presence of small scattering centres in the glass, or bubbles, causing the structure observed through the microscope by diffraction.

In order to test which was the cause, half of a fused film was masked off using wax. The sample was then placed in a beaker containing 5 % Hydrofluoric acid (HF) for 15 minutes, such a procedure being adopted in the hope of preferentially etching one phase faster than any other. Analysis of the resulting structure would then confirm which hypothesis was more likely. The HF etched a step in the film which was analysed in the SEM.

The process revealed the presence of crystallites and crystal agglomerates throughout the film. See Fig. 5.20. Qualitative analysis using an EDAX system

the SEM identified the crystal masses as being much richer in titanium than the surrounding area. It was therefore concluded that the observed blue tint was caused by Rayleigh/Mie scatter from Titanium rich crystals and crystal agglomerates.

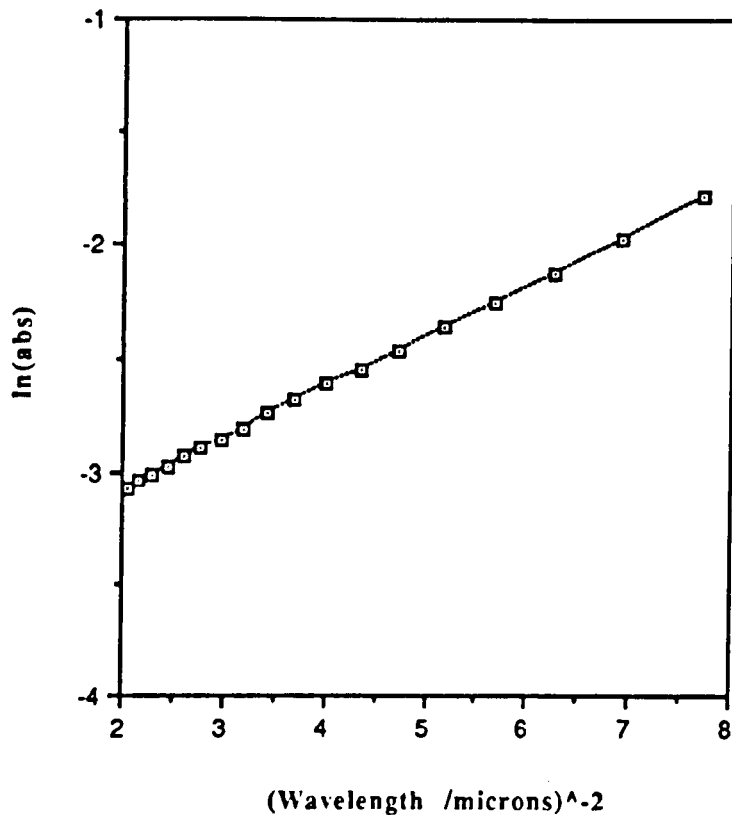


Figure 5.19 Graph of log absorption vs  $\lambda^{-2}$

Such a low doping threshold for titanium would result in such films having very limited application in integrated optics, due to scatter from such crystals producing excessive optical loss. However, since other workers<sup>6</sup>, routinely used this technique, it was felt that a solution to this problem must be available.

It was discovered that by depositing a buffer layer of  $\text{SiO}_2/\text{P}_2\text{O}_5$  immediately followed by a titanium doped layer and fusing the two layers, transparent, tint free films could be produced with much higher titanium levels, before the onset of a blue tint. The recipe used in this case, and for subsequent films, consisted of 150 sccm's  $\text{SiCl}_4$  and 160 sccm's  $\text{PCl}_3$ . Reasons for this behaviour are as yet unclear, although a possible explanation is presented.

EDAX results from measurements on such samples demonstrated the relationship between flow rates and doping levels in wt % of Titanium. All of the films used in these measurements were prepared in the same way, with a 4 layer buffer and a 6 layer core and fused at  $1250^\circ\text{C}$  for sixty minutes, (see Figs. 5.22 and 5.23).

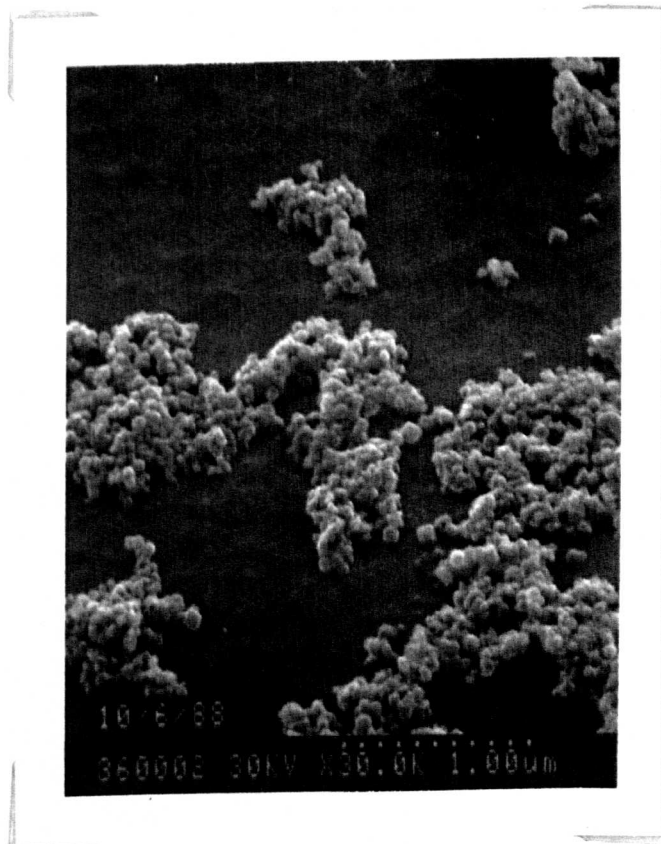
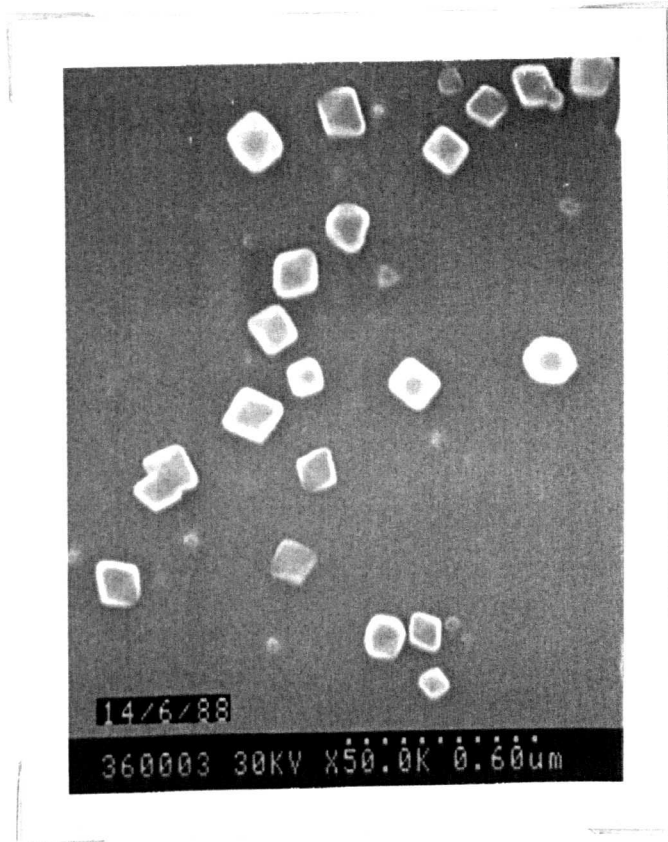


Figure 5.21 Crystals and crystal agglomerates.

Flow Rates /sccm's	Doping level /wt%
30	0.28
60	0.50
90	0.82
120	0.95
150	1.26

Figure 5.21 Table of EDAX results showing carrier gas flow rates versus doping levels for titanium. Phosphorus doping level measured relative to a standard cladding glass number RE(40). This gave 5.6 wt% P

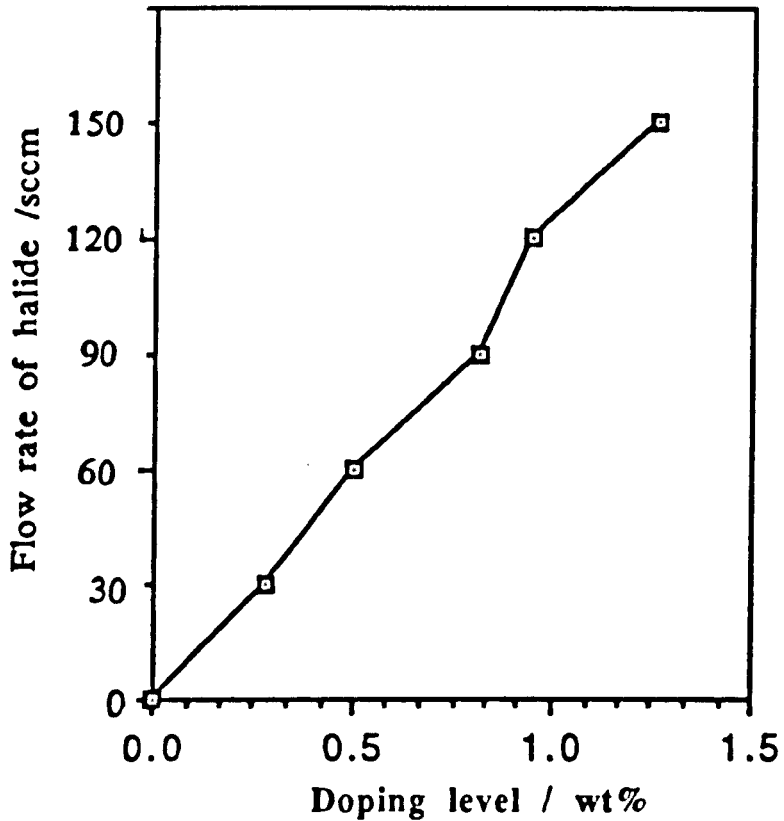


Figure 5.22 Graph of doping levels vs flow rates for titanium

The departure from linearity in Fig. 5.22 coincides with the onset of the blue tint. The  $\text{SiO}_2/\text{P}_2\text{O}_5/\text{TiO}_2$  films were susceptible to two distinct forms of film degradation.

- 1 Cracking and peeling of deposited soot giving rise to 'rosette' shaped blotches. Such films did not improve with fusing. Such degradation as discussed earlier is dependent upon torch/substrate temperature. Furthermore, degradation could be accelerated and accentuated by gently blowing on the film surface of a partially degraded sample. This type of degradation was also common to some  $\text{SiO}_2/\text{P}_2\text{O}_5$  films.
- 2 Film ageing, in which a sample left in ambient conditions in a sample box would, when fused, be blue tinted. Whereas an identical sample prepared at the same time and fused immediately would be clear.

To find a plausible explanation for the problems associated with the  $\text{SiO}_2/\text{P}_2\text{O}_5/\text{TiO}_2$  films one has to explain the following;—

- 1 Film degradation in deposited soot
- 2 Accentuation of degradation with gentle blowing — possible moisture adsorption, occurred in sample with buffer layer, with large torch/substrate separation
- 3 Appearance of blue tint for low doping levels with no buffer layer
- 4 Higher doping levels possible with buffer layer
- 5 No degradation in deposited soot for hotter substrate — reduced torch/substrate separation
- 6 Film ageing — appearance of blue tint when sample exposed to ambient atmosphere for a few days

The other information available is that the blue tint is caused by Titanium rich crystals or agglomerates and no such problems are encountered with germania films. This suggests that the problems arise from the titanium doping or the combination of Ti and phosphorus doping.

One possible explanation which may explain some of the results would be the incomplete hydrolysis of the  $\text{TiCl}_4$  in the flame and the entrapment of the chloride in the porous soot. Such trapped material may subsequently react with ambient moisture forming liquid or gaseous reaction products which may cause the rupture of the surrounding soot and the appearance of rosettes. The  $\text{TiO}_2$  produced might not then be chemically bonded to the silica and may be crystalline.

This would explain the rapid appearance of rosettes upon gentle blowing as the moisture in the breath would cause the hydrolysis reaction.

It is also plausible to suppose that if small amounts of  $\text{TiCl}_4$  were trapped in the soot, while possibly not being reacted immediately, may be oxidised in the furnace, such oxidation leading to crystalline/agglomerate products and a blue tint. Furthermore slow reaction in ambient moisture or adsorption of moisture by  $\text{P}_2\text{O}_5$  and subsequent reaction could feasibly explain film aging.

Similar arguments can be developed to explain the effect of the buffer layer in allowing higher doping levels and the effect of small torch/substrate separation in reducing degradation.

In both cases, one would expect hotter substrates, since a porous buffer layer would trap hot gases and provide some thermal insulation. Reduced torch/substrate separation would also lead to higher substrate temperatures. Hotter substrate temperatures may then result in more complete reaction of  $\text{TiCl}_4$ .

Furthermore, the reaction kinetics involved in the other ternary system  $\text{SiO}_2/\text{P}_2\text{O}_5/\text{GeO}_2$  will undoubtedly differ. However, as observed in the VAD system for  $\text{SiO}_2/\text{GeO}_2$ <sup>7</sup>, the presence of crystals of  $\text{GeO}_2$  does not lead to separate phases in the fused glass. This too, is expected from analysis of the phase diagram for this system in which a much wider glass forming region is evident. Hence we can conclude that even if the same mechanism occurs with the  $\text{GeCl}_4$ , no degradation in the fused film arising from  $\text{GeO}_2$  would result.

Whilst such an explanation is tentative, some aspects have been observed in other systems. The presence of unreacted reagents is observed in the MCVD process with the ternary system  $\text{SiO}_2/\text{P}_2\text{O}_5/\text{GeO}_2$ <sup>8</sup>. Substrate temperature effects have been observed with the binary system  $\text{SiO}_2/\text{GeO}_2$ <sup>9</sup>. Although no such behaviour was observed for  $\text{SiO}_2/\text{TiO}_2$ <sup>9</sup> the presence of a third chloride reagent such as  $\text{PCl}_3$  may alter this behaviour due to competition in the hydrolysis reaction. Such competition has been observed in the oxidation reaction analysed by Wood et al<sup>8</sup>.

Whilst the reduction in torch/substrate separation or the increase in  $\text{H}_2/\text{O}_2$  flow rates reduced the problem of film degradation it did not totally eradicate it and occasionally some samples would still exhibit film degradation. If the explanation offered is accurate, then a more effective means of ensuring more complete reaction of the chloride reagents would be desirable. It has been observed in Flame Hydrolysis systems used by other workers<sup>10,11</sup> that oxygen-rich flames are used, whereas in the system used by the author only stoichiometric flame flow rates were used. It would therefore be suggested, as an area for future work, to assess the effect (if any) on film degradation of using oxygen rich flames, as excess oxygen may aid more complete reaction.

## 5.6.2 THE SYSTEM $\text{SiO}_2/\text{P}_2\text{O}_5/\text{GeO}_2$

In general, germania doped phosphosilicate glass presented fewer difficulties than its titania counterpart. The main problems encountered are film cracking and poor surface quality for thicker layers and/or higher doping levels. Doping levels as low as 75 sccm's of carrier gas through  $\text{GeCl}_4$  in thick films (10 layers and above) were found to produce cracking in fused films. Thinner films (<4 layers) could withstand much higher doping levels (120 sccm's) before such effects dominated.

The value of refractive index calculated from EDAX measurements for samples in which cracking was evident with thick films and low doping levels was 2.2wt% Ge. Such a value appears in reasonable agreement with other workers using this technique<sup>6</sup>, considering the film thicknesses used by the author.

Other problems encountered included film opacity in fusing thick films (>12 layers). This problem appears to be caused by gas entrapment in the pores during fusing and could be solved by reducing the fusing rate to allow the gas time to escape or by using a more diffusing gas as a furnace atmosphere.

Common problems of film shadowing during deposition were encountered and have already been discussed.

Film degradation resulting in 'rosettes' was not encountered in any of the  $\text{GeCl}_4$  depositions.

In contrast to the titania doped films, no buffer layer was necessary. As for the titania system EDAX measurements were carried out to assess the doping levels obtained in fused films with differing flow rates. Figure 5.24 shows the linear relationship obtained. Such linear dependence has been reported by other workers for the binary system<sup>11</sup>.

Flow Rates /sccm's	Doping levels /wt%
30	2.2
48	2.8
60	4.5
70	5.5

Figure 5.23 Table of EDAX results showing flow rates of carrier gas vs doping levels for Germanium. Phosphorus levels as for titanium doping (Fig. 5.21)

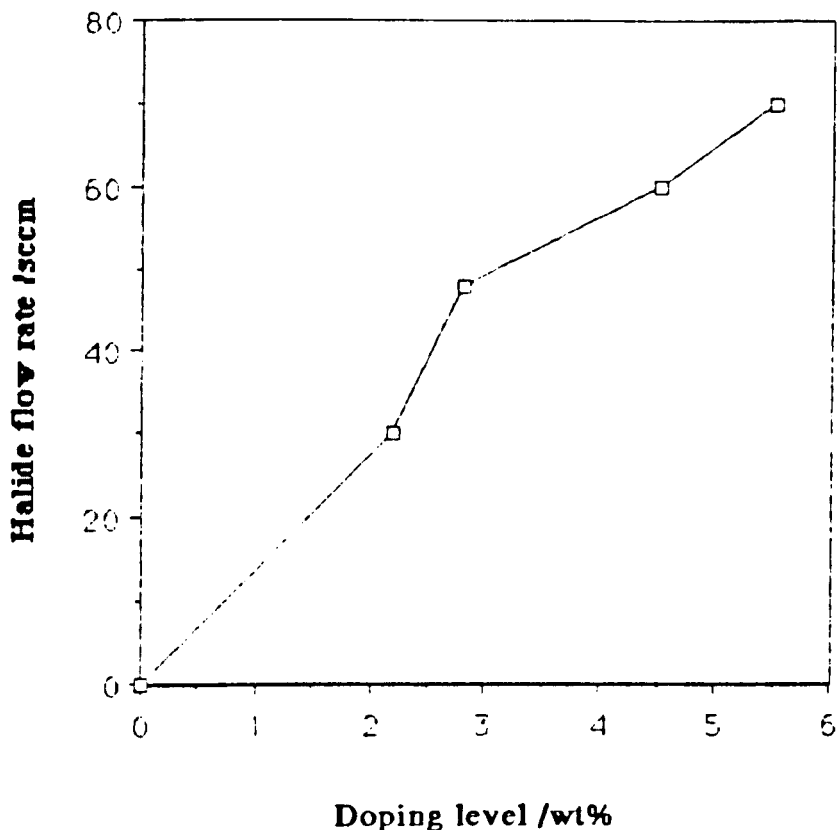


Figure 5.24 Graph of doping level data for Germanium

### 5.7 EFFECT OF FURNACE ATMOSPHERES ON FUSING

In order to evaluate the effects (if any) of a furnace atmosphere during fusing or sintering, a sensitive indicator was required. Using a sample which would completely fuse in various fusing atmospheres for a particular fusing temperature and fusing time is not particularly suitable since such a sample yields little information on the change in sintering rates. A number of experiments were considered, such as fusing for varying times or temperatures, to analyse the sinter structure. However since films can be readily fused without fusing atmospheres, a simple experiment was desired as such experimentation was more for interest than necessity.

The method chosen involved finding a suitable temperature and time which would completely fuse a film of a given composition in static air, and then, reduce the temperature to a level at which a reasonably high degree of fusing was evident, but fusing was incomplete. A small increase in fusing rate with a fusing atmosphere would then be reflected in a greater degree of fusing. Similarly, retarded sintering rates would be identifiable in reduced sintering.

Two atmosphere types were tried: Helium bubbled through water, and Oxygen bubbled through water. A check was made by fusing in static air with the piping from the water bath connected and all three compared to static air.

The deposition conditions used were:-

Dopant	Flow Rate /sccm's
SiCl <sub>4</sub>	75
PCl <sub>3</sub>	160

Figure 5.25 Deposition data in fusing atmosphere experiment.

A fusing temperature of 1250°C for 1 hour completely fused the soot. Reducing the temperature to 1202°C produced a partially fused film which would serve as a suitable indicator. In this film, the centre of the sample had fused clear while the edges were opaque. Fig 5.27 gives examples of SEM photos detailing the two areas.

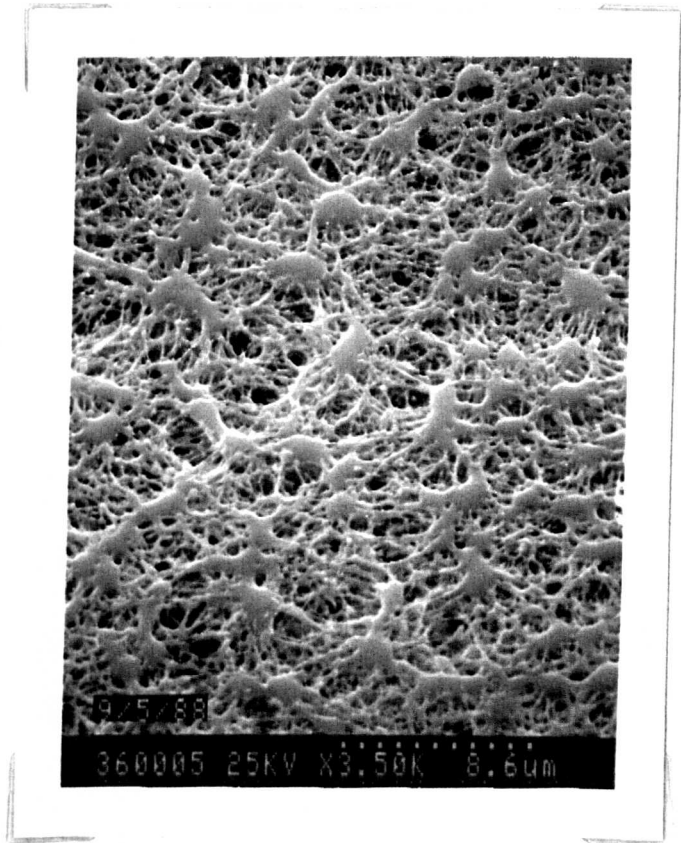
With this sample, an increase in sintering would result in less opacity at the edges and a reduction in sintering would lead to more opacity towards the sample centre.

In both cases using furnace atmospheres, a reduction in sintering was evident, the samples being totally opaque. The gas flow rate used in both cases was 2 l/min through water at 80°C. The furnace temperature was measured prior to fusing and maintained at 1202° ± 2°C. Fig 5.28 shows the resulting structure in the presence of fusing atmospheres. It is interesting to note that the He atmosphere had a greater retarding effect on sintering than the O<sub>2</sub> atmosphere.

Both of these results are in agreement with those of Scherer<sup>12</sup> in which the moist sintering atmosphere was found to retard sintering by *drying the soot*. This suggests that the soot is heavily saturated with water during deposition. The reason for the greater retarding effect of Helium may be due to the more searching nature of that gas and its greater ability to diffuse through smaller pores. Alternatively the oxygen, being a covalent molecule, may be more effective as a carrier gas for water, and may be more heavily hydrated on entering the furnace. As such it would be less efficient in drying the soot.

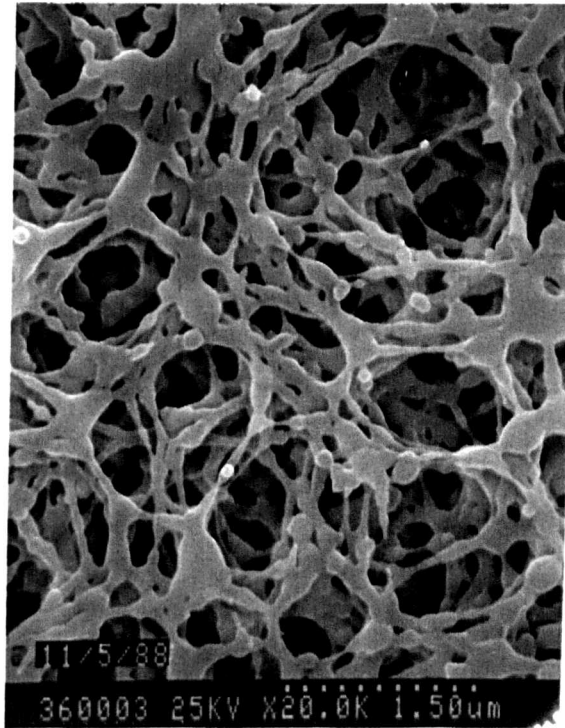


(a) Centre of sample

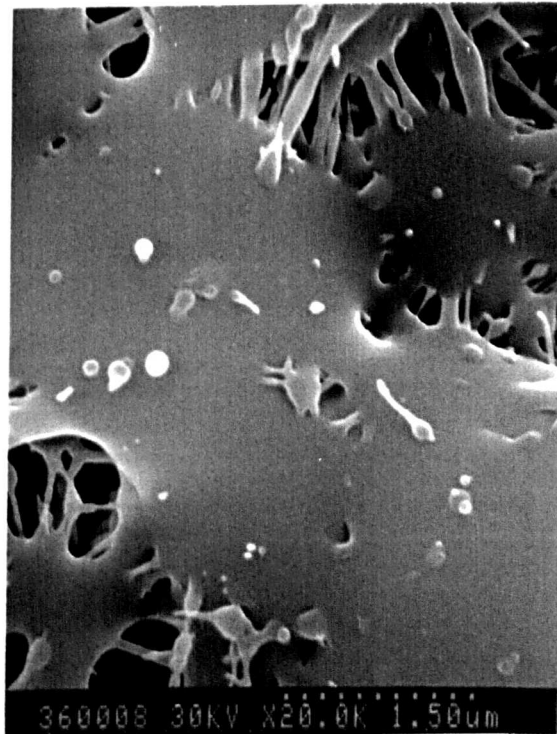


(b) Edge of sample

Figure 5.27 Sintering structures obtained with no added atmospheres



(a) Helium



(b) Oxygen

Figure 5.29 Sintering structures in the presence of fusing atmospheres  
— both photographs taken at centre of sample

## 5.8 CONCLUSIONS

The foregoing section has described techniques used to deposit the doped silica soot and has described the means by which such soot can be assessed. Thermophoretic effects have been highlighted which can seriously affect the homogeneity of deposited soot thickness and techniques of minimising such effects, by varying the silica torch position, have been presented. Characterisation of the layer thickness has been carried out and the results indicate the need for careful measurement procedures in talysteping the consolidated film. Furthermore care must be taken when referring to such measurements, as different traversal rates used during deposition produce different layer thicknesses for the same number of torch traversals.

The problems encountered with each film type used are discussed and the main problems have been highlighted. The  $\text{SiO}_2/\text{P}_2\text{O}_5/\text{TiO}_2$  films are found to contain crystals and crystal agglomerates with doping levels of  $> 0.82\text{wt}\%$  or  $0.2\text{wt}\%$  without a buffer layer. Such inclusions act as scattering centres and give the films a characteristic blue tint. A possible explanation as to the cause behind such crystallisation involved the inclusion of unreacted  $\text{TiCl}_4$  and/or  $\text{PCl}_3$  in the deposited soot which subsequently oxidised in moisture present in the air or during fusing leading to soot decomposition and film ageing. In either case, insoluble crystalline material would result and unsuitable films would be produced.

In the  $\text{SiO}_2/\text{P}_2\text{O}_5/\text{GeO}_2$  films, the main difficulty encountered was film cracking for doping levels  $> 2.2 \text{ wt}\%$ . Such cracking was also more pronounced in thicker films  $> 10$  layers.

Film fusing in various atmospheres was carried out with the result that sintering was retarded when compared with sintering in static air. Such an effect was observed even when 'wet' atmospheres were used.

There lies the potential for future work in two main areas:—

- 1 Using a re-designed turntable which incorporates a heater. In this way the thermophoretic effects can be controlled and even used to tailor the layer thickness of the deposited films
- 2 A more in-depth study into the causes of the film degradation encountered, which could take the form of experimenting with the flow rates of the  $\text{H}_2$  and  $\text{O}_2$  in the hydrolysing flame and monitoring and film effects; or an in-depth analysis of the effluent gases produced from the flame using I-R spectroscopy, following a method similar to that of Wood et al<sup>8</sup>, in their analysis of the MCVD process

## 5.9 REFERENCES

1. K.L. WALKER, G.M. HOMSY, F.T. GEYLING  
J. Colloid and Interface Sci., Vol. 69, No. 1, 15th March 1979, pp138–147  
Thermophoretic Deposition of Small Particles in Laminar Tube Flow
2. K.L. WALKER, F.T. GEYLING, S.R. NAGEL  
J. Am. Ceram. Soc., Vol. 63, No. 9–10, pp552–558  
Thermophoretic Deposition of Small Particles in the Modified Chemical Vapour  
Deposition (MCVD) Process
3. T. AMBRIDGE, B.WAKEFIELD  
Br. Telecom Technol. J., Vol. 3, No. 1, Jan. 1985  
Microanalytical Techniques for Electronic and Optical Materials and Device  
research
4. OPTICS  
Hecht, Zajac, 1980, 6th edition, Addison–Wesley
5. W. VOGEL  
Structure and Crystallization of glasses, pp 33–35, Pergamon Press, 1971
6. M. KAWACHI, M. YASU, T. EDAHIRO  
Electr. Lett., Vol. 19, No. 15, 21st July 1983, pp583–584  
Fabrication of SiO<sub>2</sub>/TiO<sub>2</sub> Glass Planar Optical Waveguides By Flame Hydrolysis  
Deposition
7. E. POTKAY, H.R. CLARK, I.P. SMYTH, T.Y. KOMETANI, D.L. WOOD  
J. Lightwave Tech., Vol. 6, No. 8, Aug. 1988, pp1338–  
Characterisation of Soot from VAD
8. D.L. WOOD, K.L. WALKER, J.B. MACCHESNEY, J.R. SIMPSON,  
R. CSENSITS  
J. Lightwave Tech., Vol. LT–5, No.2, Feb. 1987, pp277–285  
Germanium Chemistry in MCVD process for Optical Fibre Fabrication
9. T. EDAHIRO, M. KAWACHI, S.SUDO, T. EDAHIRO  
Jpn. J. Appl. Phys., Vol. 19, No. 11, Nov. 1980, pp2047–2054  
Deposition Properties of High–silica Particles in the Flame Hydrolysis Reaction
10. M. KAWACHI, S. SUDO, T. EDAHIRO  
Jpn. J. Appl. Phys., Vol. 20, No. 4, April 1981, pp709–712  
Threshold Gas Flow Rate of Halide Materials for the Formation of Oxide  
Particles in the VAD Process for Optical Fibre Fabrication.
11. A.S. HUANG, Y.A. ARIE, C.C. NEIL, J.M. HAMMER  
Appl. Opt., Vol. 24, No. 24, 15th Dec. 1985, pp4404–4407  
Study of Refractive Index of GeO<sub>2</sub>:SiO<sub>2</sub> mixtures using deposited–thin–film  
Optical Waveguides.

12.G.W. SCHERER, D.L. BACHMAN

J. Am. Ceram. Soc., Vol. 60, No. 5-6, May-June 1977, pp239-243

Sintering of Low-Density Glasses: II, Experimental Study

This section is concerned with a description of techniques used to assess the optical waveguiding characteristics of the planar films produced. The characteristics of importance are the refractive index, film thickness and optical loss. Other factors of importance such as dispersion and in-plane scatter have not been investigated.

This section reviews the main aspects of the theory involved in planar optical waveguides and includes a derivation of the Transverse Resonance Condition (TRC) using the ray-optic approach. The operation of the Prism Coupler is described in simple terms in which the phase matching requirements for coupling are presented. A method is then described using the results obtained from the Prism Coupler with the expression derived from the TRC to calculate the thin film parameters of index  $n_f$  and thickness  $W$ . Practical aspects involved in prism design and use are mentioned, and the causes and uses of mode lines or (m-lines) are discussed. Results of film index and thickness from films fabricated by the author are presented, along with qualitative estimates of film loss based on the amount of scatter visible from the film whilst guiding.

### 6.1 PLANAR WAVEGUIDING THEORY

It is not the intention of the author to describe exhaustively the theoretical framework surrounding optical waveguides, merely to describe in sufficient detail the theory required to understand the experiments performed and with sufficient brevity to avoid confusion. To this end, only the theory behind the particular application is included in each section. Further theory is included as and when the need arises.

Numerous references<sup>1-5</sup> abound to instruct the reader in the theory concerning Maxwell's equations and electromagnetic aspects of waveguiding theory. Although the following sections assume a degree of background knowledge in these matters, the main aspects of the theory involved will be reviewed without recourse to electromagnetic field descriptions.

#### 6.1.1 DESCRIPTION OF THE PROBLEM AND BASIC REQUIREMENTS

In order to understand the equations derived, it is necessary to have a clear picture of the problem being considered. In this case, one is concerned with describing the way in which coherent light, generally of a fixed wavelength  $\lambda$ , with wavevector  $k = 2\pi/\lambda$ , travels down a dielectric sheet or film having refractive index,

$n_f$ . Generally, since such films are thin, ( $< 50 \mu\text{m}$ ), a substrate is required to provide a rigid supporting structure. The substrates can be of a similar material, such as silica in this case, or a dissimilar material, such as silicon, on to which a buffer layer of dielectric material has been deposited or grown prior to the film deposition. In either case, below the film there is another dielectric sheet with refractive index  $n_s$ . Commonly, the medium above the film is air although a dielectric *cladding* layer (index  $n_c$ ) is sometimes deposited on top. Figure 6.1 schematically shows a typical structure encountered.

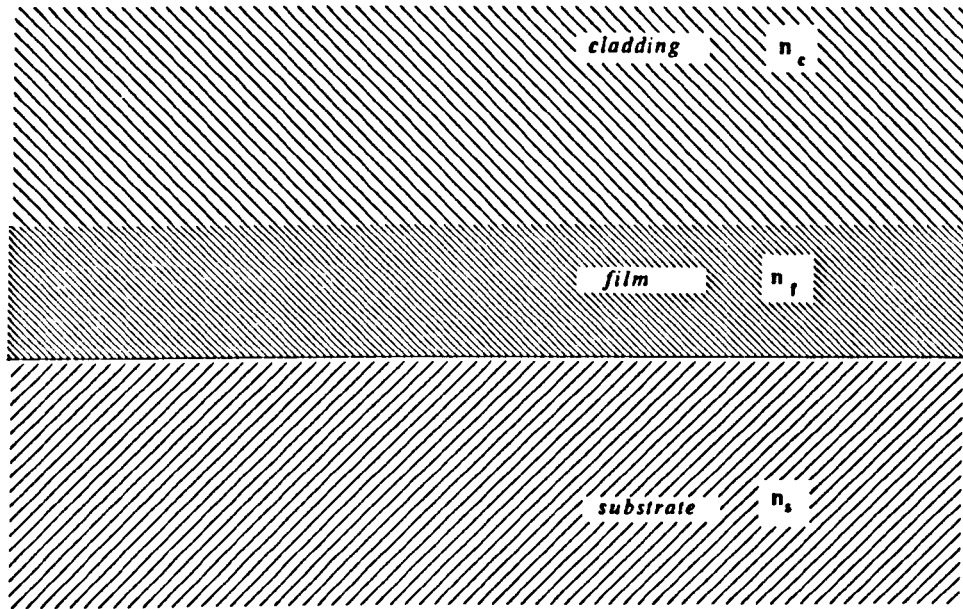


Figure 6.1 Schematic of typical planar waveguide structure, showing cladding, film and substrate regions

The propagation or *guidance* of light down the dielectric film or *waveguide* occurs by a process of total internal reflection at the film interfaces. In order for this process to occur, there is a restriction on the values of refractive index possible. This restriction requires that the film index  $n_f$  be greater than both the buffer layer index  $n_s$ , and the cladding index,  $n_c$ .

i.e. 
$$n_f > n_s, n_c$$

Since the *cladding* is normally air ( $n_c=1$ ), then

$$n_f > n_s > n_c$$

Total internal reflection also requires that the angles of incidence of a ray on the inside of the film boundaries lies within particular limits determined by the values of  $n_f$ ,  $n_c$  and  $n_s$ .

These limits can be calculated from Snell's law<sup>6</sup> which states:-

$$n \sin \theta_i = n' \sin \theta_r$$

- where  $n$  is the film index,  $n_f$ , and  $n'$  is the cladding or substrate index.

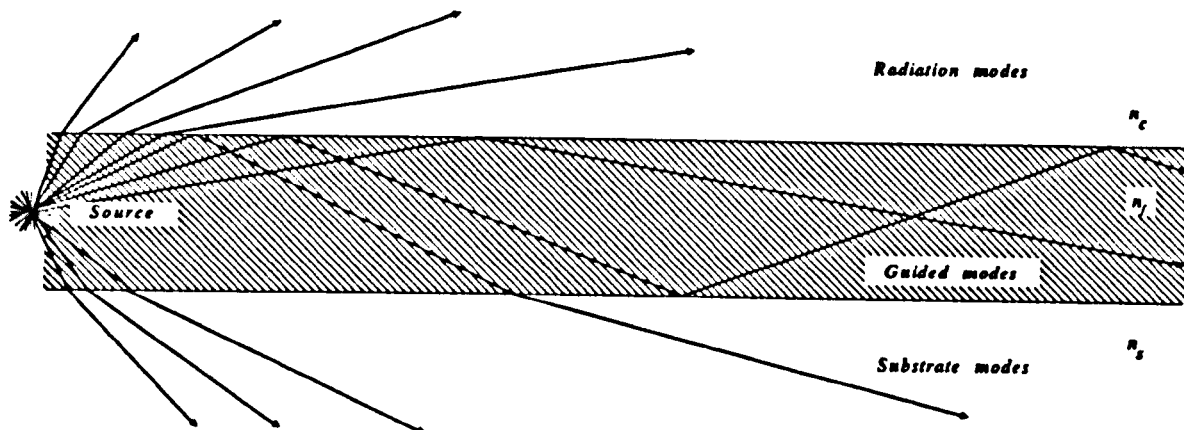


Figure 6.2 Schematic of  $n_f$ ,  $n_c$ ,  $n_s$  showing mode types encountered

The critical angles are defined as those for which  $\theta_r = 90^\circ$ . Thus the angular limits of incidence for total internal reflection are:-

$$\theta_i > \sin^{-1} (n_c / n_f) \quad - \quad \text{at the film/cladding interface}$$

$$\theta_i > \sin^{-1} (n_s / n_f) \quad - \quad \text{at the film/substrate interface}$$

Once both these conditions are satisfied, the light is constrained within the film. However, in order for the light to propagate down the waveguide there is a further criterion which must be satisfied. This criterion requires that the *phase* of the wave after two successive reflections must equal that of the wave before such reflections. This phase requirement has the effect of limiting the values of  $\theta_i$  permissible for guidance to occur from a continuum to a discrete set. If this were not the case, and there was a small phase difference between the waves, then this would increase with subsequent reflections until eventually the phase differences added up to zero resulting in the cancellation of the wave.

It is the purpose of the next section to derive the phase condition which must be satisfied in order that the wave will propagate down the guide. This condition is known as the *Transverse Resonance Condition*.

### 6.1.2 DERIVATION OF THE TRANSVERSE RESONANCE CONDITION

The following derivation is carried out using the ray-optic approach for guided waves. This derivation has been performed by numerous authors, such as Kogelnik<sup>7</sup>, Hunsperger<sup>8</sup>, and Unger<sup>9</sup>. But it is the derivation by Tien<sup>10</sup>, which will be followed here.

As has already been discussed, energy propagates down the dielectric waveguide when total internal reflection occurs at both film interfaces.

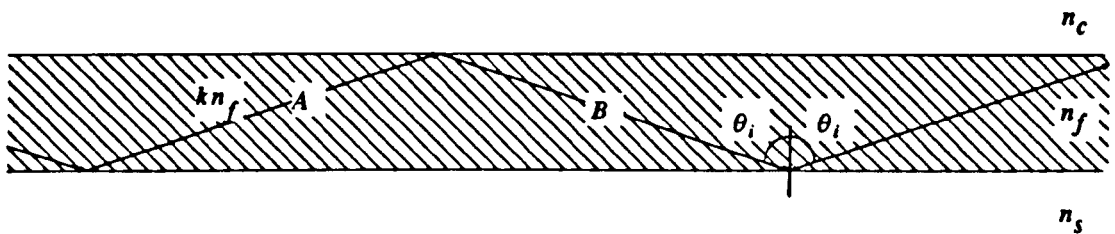


Figure 6.3 Schematic of energy propagation down a dielectric waveguide

Such motion can be represented by two superimposed plane waves, A and B, whose wavenormals follow a zig-zag path down the waveguide, (see Fig. 6.3). The wavevectors of each wave have magnitude,  $kn_f$ , where  $k$  is the free space wavevector and equals  $2\pi/\lambda$  and  $n_f$  is the film index. We can resolve the wavevectors into their components,  $k_z$  and  $k_x$ , and can consider each separately. The  $z$ -component describes the velocity of the mode down the waveguide and is generally referred to as a propagation constant,  $\beta$ . It is equivalent to:-

$$\beta = kn_f \sin \theta_i$$

- or:-

$$\beta = kN_{eff}$$

— where  $N_{eff}$  is the effective index of the waveguide and lies between the values  $n_s$  and  $n_f$ .

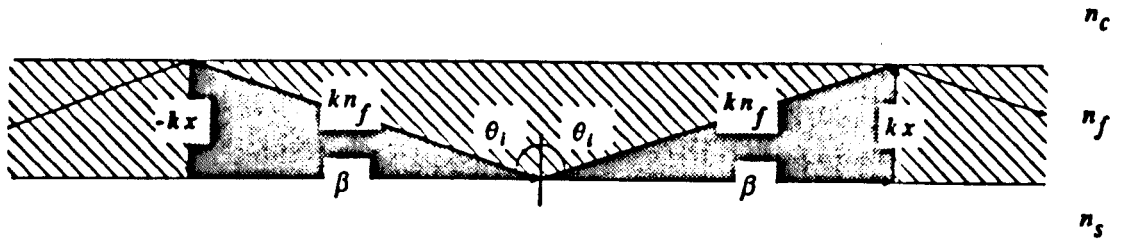


Figure 6.4 Schematic showing wavevectors resolved into constituent components

The  $z$ -components of the wavevector of waves A and B are equal, indicating that the waves propagate at the same speed down the guide.

The  $x$ -components of the wavevectors of waves A and B represent upward and downward travelling waves respectively. Their superposition results in a standing wave pattern which determines the field distribution across the waveguide. This field distribution is referred to as a *mode*, and propagates with velocity  $v$  down the guide, ( $v = \omega / \beta$  where  $\omega$  is the frequency of the wave in question). Both  $k_x$  and  $k_z$  depend on the values of  $\theta_i$ , and when it is varied, both the propagation constant and the field distribution or mode, vary.

The shape of the field distribution (or mode profile) across the waveguide can be determined from the solution of the Helmholtz wave equation<sup>11</sup>, with the appropriate boundary conditions for the wave polarization. However, for our purposes, it is sufficient to derive the condition of constructive interference required for guided modes.

To do this, we consider the  $x$ -components of the wavevectors A and B and calculate the total phase change experienced by the plane wave travelling transversely across the film. For one round trip, the wave travels across the width ( $W$ ) of the film twice, incurring a phase change of  $2 k_x W$ .

Since:—

$$k_x = kn_f \cos \theta_i$$

– then the phase change  $\phi$  is:–

$$\phi = 2kn_f \cos \theta_i W$$

If we now include the phase changes incurred on reflection from the film/cladding and film/substrate boundaries,  $\varphi_c$  and  $\varphi_s$  respectively, then the total phase change incurred is:–

$$\phi = 2 kn_f W \cos \theta_i - 2\varphi_c - 2\varphi_s$$

This phase change must equal  $2\pi$  or a multiple thereof to satisfy the criterion for constructive interference. Therefore:–

$$2 kn_f W \cos \theta_i - 2\varphi_c - 2\varphi_s = 2m\pi$$

– where  $m$  is an integer and defines the *order* of the mode ( $m = 0, 1, 2, \dots$ ). This expression is known as the Transverse Resonance Condition.

The phase changes  $\varphi_c$  and  $\varphi_s$  depend upon the field polarization (Transverse Electric, TE or Transverse Magnetic, TM), on the refractive indices  $n_c$ ,  $n_f$ ,  $n_s$  and on the angle of incidence,  $\theta_i$ .

Expressions for the phase shifts can be derived by the application of the relevant boundary conditions for the field polarization used (TE or TM)<sup>12</sup>.

Here the results will be simply stated, as:–

$$\tan \varphi_c = \frac{(n_f^2 \sin^2 \theta_i - n_c^2)^{\frac{1}{2}}}{n_f \cos \theta_i}$$

$$\tan \varphi_c = \frac{(n_f^2 \sin^2 \theta_i - n_c^2)^{\frac{1}{2}}}{n_f \cos \theta_i}$$

– for TE waves. Similar expressions exist for TM waves<sup>11</sup>.

As Tien<sup>10</sup>, points out, in a guided mode there is only propagation in the  $z$ -direction, the field in the  $x$ -direction merely forming a standing wave, with *evanescent* fields decaying in the positive and negative  $x$ -directions beyond the film boundaries.

We can now move on to consider a technique for coupling light into the waveguides using evanescent fields – namely the Prism Coupler. This, when used in conjunction with the expression for the Transverse Resonance Condition, provides

a means of measuring the film index  $n_f$ , and film thickness  $W$ .

## 6.2 THE PRISM COUPLER

The prism coupler, as the name suggests, is a means by which light can be coupled into a waveguide using a prism. This section will give a brief description of prism design and application.

In a Prism Coupler, the waveguide is mechanically pressed against the prism base. Dust particles between the film and prism base act as spacers, ensuring the presence of an air gap. An incident light beam strikes the prism face AB at an angle  $\alpha_i$ , is refracted inside the prism, (which has refractive index  $n_p > n_f$ ) and suffers total internal reflection at the prism base. If the air gap is sufficiently small, light can be coupled into the waveguide by a process of 'optical tunneling' whereby the evanescent field extending from the prism base couples into the waveguide and excites a waveguide mode.

In order for energy to be transferred, it is necessary to match the  $z$ -component of the wavevector, inside the prism with that expected inside the guide, for the particular mode being excited. See Figure 6.6.

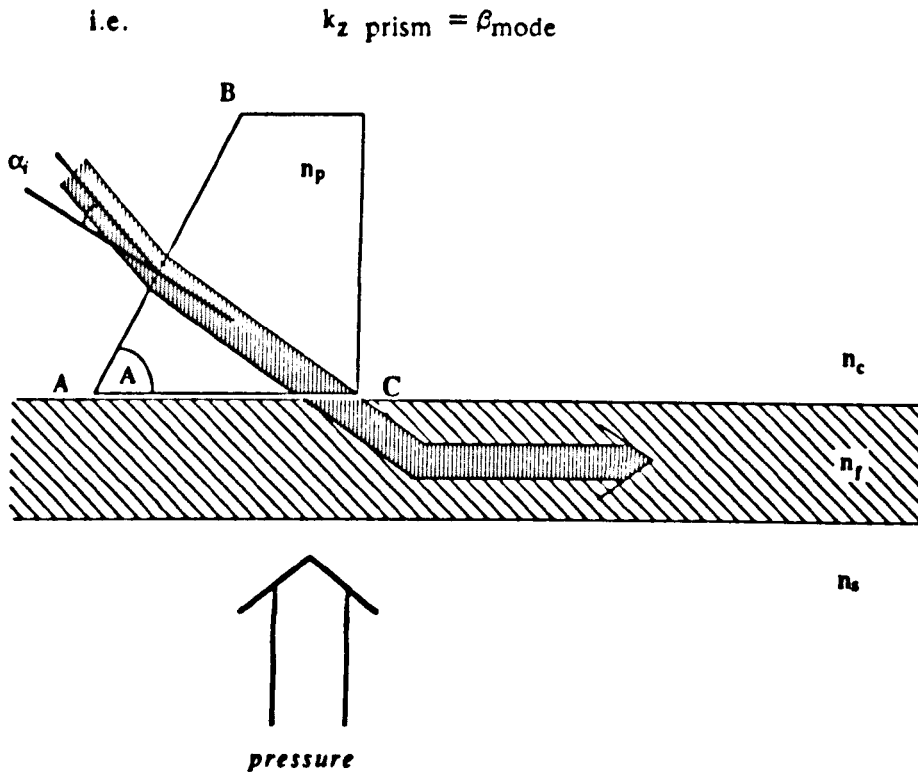


Figure 6.5 Schematic depicting prism coupling using a right-angled prism

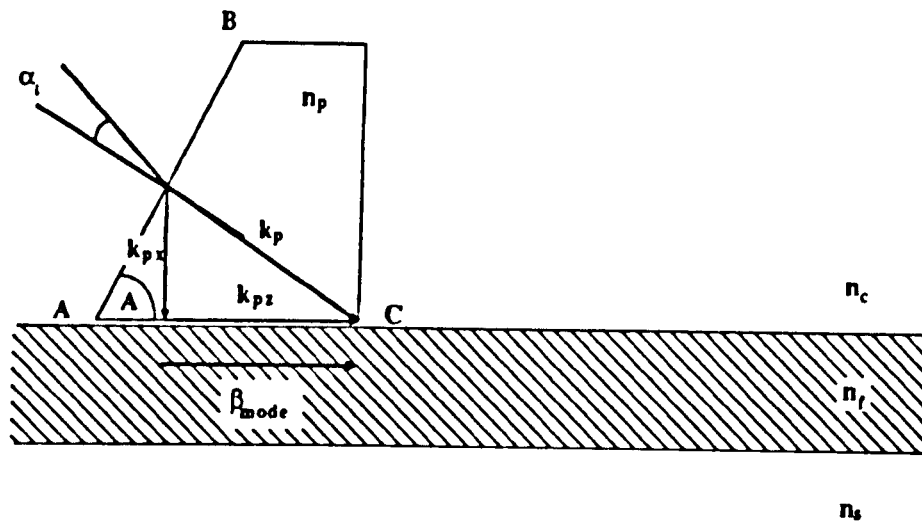


Figure 6.6 Schematic of phase matching for prism coupling

As the angle of incidence in the prism face is varied, the values of  $k_z$  inside the prism will change. At the values of  $\alpha_i$ , where phase matching occurs, the light will be coupled into a particular mode within the waveguide. For each mode that the waveguide can support, there will be a corresponding angle of incidence which can excite it. When coupling is achieved, power is transferred from the area where the beam strikes the prism base. It is at this area or *contact point* where the film parameters are measured<sup>12</sup>.

As well as coupling light in, the prism coupler also couples light out of the waveguide. This dual process occurs along the entire length of the prism base in contact with the film from the contact point onwards. A prism designed for this purpose is called a *rooftop prism*, (see Section 6.3.1). For some applications, it is desirable to stop the light coupling out of the waveguide. To this end a right angled prism is used, designed to frustrate output coupling, by reducing the prism base length. Furthermore, higher coupling efficiency can be achieved by ensuring that the coupling spot is very close to the prism corner.

Once the mode is excited inside the waveguide, the associated wavenormal follows a zig-zag path down the guide, incident on the film boundaries at an angle  $\theta_j$ . However, since we do not know the values of the angles for the modes inside the waveguide, we cannot calculate directly from individual values of  $\alpha_i$  the value of  $n_f$ . What is calculated instead is the value of  $N_{eff}$  – the effective index for the mode. This can be achieved using the expression:–

$$N_{eff} = n_p \sin \left[ A + \sin^{-1} \left[ \frac{\sin \alpha_i}{n_p} \right] \right]$$

- where  $N_{eff} = n_f \sin \theta_i$ ,  $A$  is the prism angle BAC,  $\alpha_i$  the angle of incidence on the prism face, and  $n_p$  the prism index.

This expression can be derived by applying Snell's law to calculate the angle of incidence *inside* the prism, keeping in mind the convention that angles of incidence *above* the normal to the prism face AB are taken as negative, whilst those *below* the normal are taken as positive.

In order to calculate the actual value of film index, we need either:-

- (1) A single mode waveguide in which the film thickness is known, or
- (2) A multi-mode waveguide

In both cases, the value of the substrate index,  $n_s$ , is required *and* the value or values of  $N_{eff}$ .

### 6.2.1 CALCULATION OF THIN-FILM PARAMETERS

One is now in a position to combine the results from measurements made using the Prism Coupler with the expression for the Transverse Resonance Condition to calculate the values of film index  $n_f$  and film thickness  $W$ <sup>13</sup>.

Recalling the expression for the transverse resonance condition:-

$$2kn_f W \cos \theta_i - 2\varphi_c - 2\varphi_s = 2m\pi$$

- with  $\theta_i$  being the angle that the mode wavenormal makes on the film boundaries *inside* the waveguide. Since we cannot measure this angle, it is useful to eliminate it as follows:-

$$\left. \begin{array}{l} N_{eff} = n_f \sin \theta_i \\ N_{eff}^2 = n_f^2 \sin^2 \theta_i \end{array} \right\} n_f \cos \theta_i = (n_f^2 - N_{eff}^2)^{\frac{1}{2}}$$

We thus end up with (after a little re-arrangement):-

$$W = \frac{m\pi + \varphi_c + \varphi_s}{k(n_f^2 - N_{eff}^2)^{\frac{1}{2}}}$$

- where  $\varphi_c$  and  $\varphi_s$  are expressed as:-

$$\varphi_c = \tan^{-1} \left[ \frac{(N_{eff}^2 - n_c^2)^{\frac{1}{2}}}{(n_f^2 - N_{eff}^2)^{\frac{1}{2}}} \right]$$

$$\varphi_s = \tan^{-1} \left[ \frac{(N_{eff}^2 - n_s^2)^{\frac{1}{2}}}{(n_f^2 - N_{eff}^2)^{\frac{1}{2}}} \right]$$

In the case of a single mode waveguide, ( $m = 0$ ), a knowledge of the film thickness  $W$ , allows the calculation of the film index  $n_f$ .

For multimode waveguides, a system of simultaneous equations can be generated from each value of  $N_{eff}$ , and solved to give a value for  $W$  and  $n_f$ . Alternatively a more simple solution is to use a computer to generate plots of the variation of film thickness with film index for *each* value of  $N_{eff}$ , by incrementing values for  $n_f$  (or  $W$ ). By superimposing such plots, the true value of  $W$  and  $n_f$  can be found from the point of intersection.

It was this approach which was adopted by the author. Programs were written using the language QUICK BASIC (QB) to facilitate such work. One program calculated values of  $N_{eff}$  from angles of incidence, the second calculated values of  $n_f$  and  $W$  from overlay plots as outlined above, and the third used the values of  $n_f$  and  $W$  calculated, re-substituted into the transverse resonance condition to calculate the dispersion relation of the waveguide.

### 6.3 PRISM COUPLING PRACTICE

In practice, the experimenter is interested in topics such as: how to design a suitable prism; whether to use a right angled prism or a rooftop prism; how to make use of mode lines ( $m$ -lines); how to assess scatter from mode lines; and what is the accuracy of measurements made. It is a consideration of such topics that will be dealt with in the following pages.

It is worthwhile pointing out that it is in practice that one discovers the greatest drawback involved with the prism coupler technique, namely the requirement for physical contact between prism and film. It was found that many samples could not withstand the ordeal by prism coupler and shattered when pressure was applied to bring the prism and film into close contact.

### 6.3.1 PRISM DESIGN

In designing a suitable prism for prism coupling one must consider whether one wants merely an input or output coupler, or whether one wants an input and output coupler combined. Where an input (or output) coupler is desired one is dealing with a right angled prism of the sort shown in figure 6.7(a).

Alternatively, a rooftop prism can be used, which couples light both in *and* out of the waveguide using a single prism, (fig. 6.7(b)).

Having decided which prism design to use, it is then necessary to determine suitable values for prism refractive index  $n_p$  and prism angle  $A$ . The choice of such parameters is generally determined by the film index encountered and the practical requirement of having the input angle to the prism at, or near, normal incidence. Generally, the prism angle would be chosen as  $45^\circ$  or  $60^\circ$  and the prism index calculated from the phase matching requirement:—

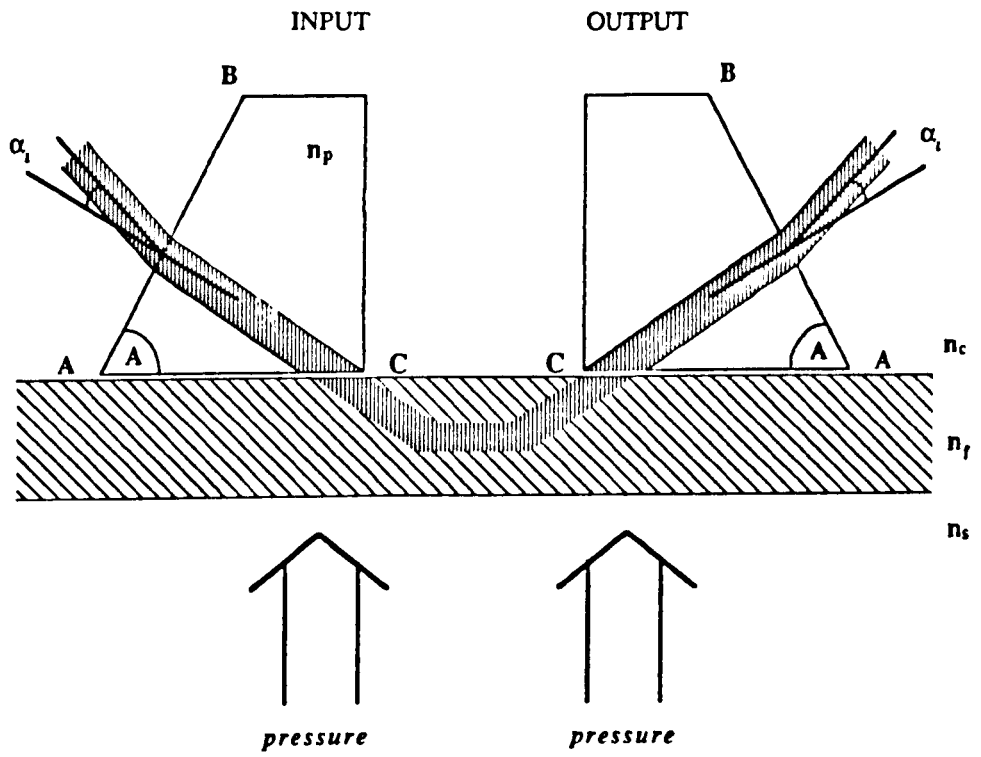
$$k_z \text{ prism} = \beta_{\text{film}}$$

— which reduces to:—

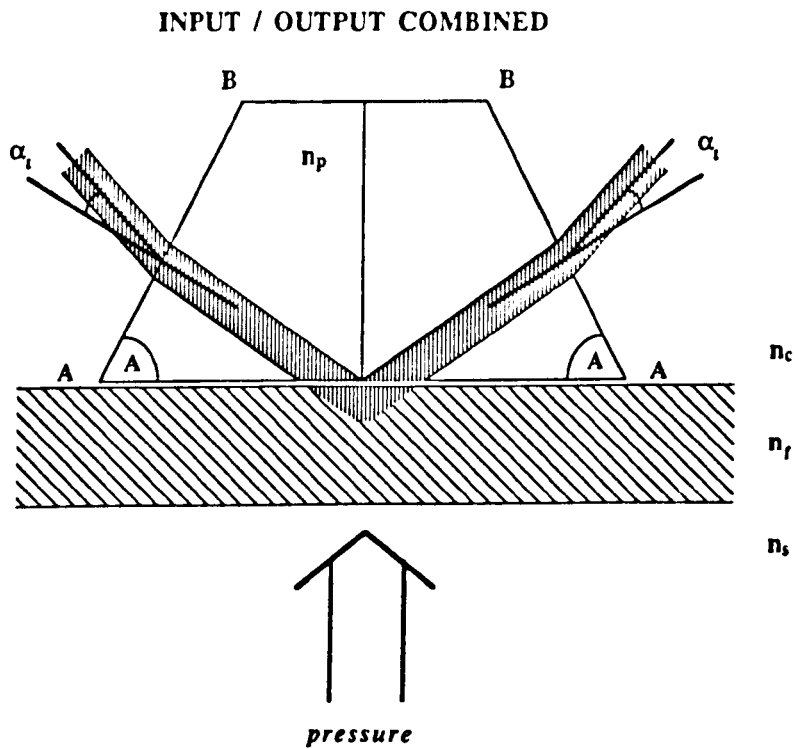
$$n_p \cos \theta_p = n_f$$

In a  $45^\circ$  prism at normal incidence,  $\theta_p = 45^\circ$ ; in a  $60^\circ$  prism,  $\theta_p = 30^\circ$ . With a knowledge of film index, a suitable value of prism index can be calculated.

For the silica films fabricated by the author, a typical value for  $n_f$  would be 1.47. Using this value of  $n_f$ , with a  $60^\circ$  prism, a glass with index 1.69 would be required for the prism. The commercial glass with index closest to this value was Schott SF15, having a refractive index of 1.70. This material was subsequently used to fabricate all of the prisms used by the author. A further refinement used in the prisms involved frosting the back face of the prism. This prevented any light which struck the back face from being returned back along the input beam path.



(a) Right-angled prisms



(b) Rooftop prism

Figure 6.7 Prism coupler designs

### 6.3.2 MODE LINES (M-LINES)

Mode lines come about as a result of light scattering<sup>14</sup> within multimode waveguides. This scattering occurs both perpendicular to, and in the plane of the waveguide. When light is coupled into the guide, it is scattered and excites other mode orders (a *single* mode line would be observed in a single mode guide). When light is coupled out of the waveguide, using an output prism, the different mode orders have different output angles associated with them and are spatially separate when viewed on a screen. See Figure 6.8. As a consequence of this, the *m*-lines give a direct display of the mode spectrum of the waveguide.

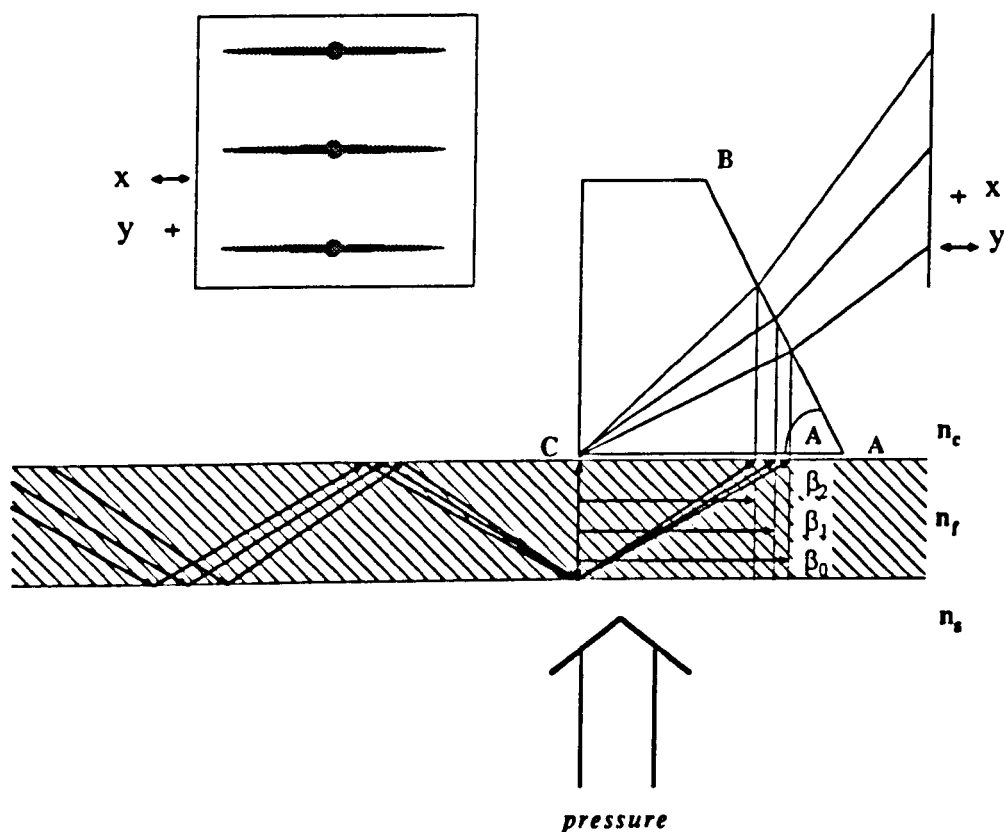


Figure 6.8 Mode lines in a right-angled prism

Mode lines are a result of *in plane* scatter in the guide and may be used to give a qualitative estimation of the guide quality, since the greater the scatter, the longer the mode line (for a fixed prism/screen separation and prism/film pressure). In an ideal guide with no *in plane* scatter, mode spots rather than mode lines would be observed, (although in such a guide no mode spectrum would be observed either, since scatter is required to excite the higher order modes).

Mode lines can be used to improve the accuracy of measured guide effective index. When the angle of incidence onto the prism face is varied, at the points where phase matching occurs, there is an increase in brightness of the particular m-line which corresponds to the mode excited. When the phase matching condition is not satisfied, no mode lines are present since no power is coupled into the waveguide, although stray reflections or scattered light from the prism can also weakly excite the m-lines. Hence by careful observation, of the point of maximum brightness in the mode line, the most accurate value of  $\alpha_j$  can be recorded. Added sophistication can be obtained by using a photodetector instead of the human eye to quantitatively measure the maximum signal<sup>15</sup>.

### 6.3.3 MEASUREMENT PROCEDURE

The procedure for measuring the values of the mode angles was straightforward. The equipment used for this purpose consisted of a right-angled prism suitably supported on a rotation stage with a digital readout. A sample could be placed between the prism and a screw which was used to bring the prism and film into contact. Once the film was mechanically pressed to the prism base, the incident angles were quickly scanned to approximately determine the mode angles, by observing the m-lines. Once assured of guidance, the digital readout from the rotation stage was set to zero at the point where the reflected beam from the input face of the prism was coincident with the input beam.

The prism was then rotated, and readings taken when the individual mode lines appeared brightest. The zeroth order mode was that which had the largest value of  $\alpha_j$ . Beyond the highest order mode supported (lowest  $\alpha_j$ ), substrate modes could be excited. This procedure was repeated several times and for up to three positions on the film.

In all experiments, TE polarised light of wavelength equal to 632.8 nm from a He-Ne laser was used.

### 6.3.4 ACCURACY OF RESULTS

The expression which is used to calculate the value of film index derived earlier is:-

$$N_{eff} = n_p \sin \left\{ A + \sin^{-1} \left\{ \frac{\sin \alpha_j}{n_p} \right\} \right\}$$

- where  $N_{eff} = n_f \sin \theta_j$



The experimental parameters used are as follows:—

Torch Position details  $X = 80$  mm,  $Y = 21$ mm,  $\theta = 25^\circ$

$\text{SiCl}_4$  /  $\text{PCl}_3$  flow rates = 150 /160 sccm's

Prism details  $n_p = 1.7$ ,  $A = 60^\circ$

TE polarization used in a 5mW He-Ne laser with  $\lambda = 632.8$ nm

Mode No.	Angle / degrees		
	a	b	c
<b>Position A</b>			
0	1.04	1.06	1.08
1	0.34	0.41	0.37
2	-0.57	-0.43	-0.49
<b>Position B</b>			
0	0.76	0.76	0.77
1	0.07	0.11	0.10
2	-0.73	-0.67	-0.67

Figure 6.10 Mode angles from prism coupling measurements

Values of effective index ( $N_{eff}$ ) are calculated using a program called QB.PRISM, using a value of 1.46 for the substrate index.

Overlay plots of the variation of  $n_f$  with  $W$  were made for each value of  $N_{eff}$  using the program QB, 3LAYER. The value (or values) of  $n_f$  and  $W$  in the region of the point (or points) of intersection were recorded.

The spread of values observed for  $n_f$  and  $W$  arise from the limits observed in the overlay plots generated. Single values would be obtained if all of the plots intersected at one point. However when such is not the case, then there is more than one point of intersection, and a range of values for  $n_f$  and  $W$  are all that can be obtained.

Mode No.	Effective Index		
	a	b	c
<b>Position A</b>			
0	1.47812	1.47814	1.47815
1	1.47520	1.47581	1.47546
2	1.46724	1.46848	1.46795
<b>Position B</b>			
0	1.47883	1.47883	1.47892
1	1.47285	1.47320	1.47312
2	1.46583	1.46636	1.46636

Figure 6.11 Effective indices calculated from mode angles

Attempt No.	Film Index $n_f$	Thickness $/\mu\text{m}$
<b>Position A</b>		
a	1.4776-1.4784	3.6-4.0
b	1.4776-1.4784	3.8-4.2
c	1.4776-1.4794	3.6-4.2
<b>Position B</b>		
a	1.4748-1.4764	3.6-4.2
b	1.4748-1.4764	3.8-4.2
c	1.4784-1.4768	3.8-4.4

Figure 6.12 Values of film index and thickness from overlay plots of  $N_{\text{eff}}$

An average value calculated from the above data gave the film index  $n_f$  as 1.4769 with film depth  $W$  of  $3.95 \mu\text{m}$ . Values of film thickness measured using a talystep produced an average value of  $4.1 \mu\text{m}$ .

The correspondence between the values of film thickness is good, considering the fact that the film exhibited shadowing prior to sintering and considering the errors expected in such measurements (section 6.3.4).

Most of the results obtained in the prism coupling experiments were not in such agreement. Differences in the values of  $W$  obtained were often found to be as large as 33% (% difference defined as  $\Delta W / W_{\text{talystep}} \times 100\%$ ). Typically this corresponded to a 3  $\mu\text{m}$  difference in a 10  $\mu\text{m}$  film (example being batch 62,  $W_{\text{taly}} = 10 \mu\text{m}$ ,  $W_{\text{meas}} = 6.7 \mu\text{m}$  in a 10 layer film). A possible explanation for such a discrepancy is film shadowing during deposition as a result of substrate temperature effects (section 5.3). In this case, layer thickness variation would be present in the consolidated films. (One measured example gave values of film depths of 3.6  $\mu\text{m}$ , 4.4  $\mu\text{m}$  and 6.4  $\mu\text{m}$ ). Whilst some of the variations in  $W$  may be artefacts of the scoring technique used to prepare films for talystep measurement, the differences encountered indicate the effect of inhomogeneous deposition. Since, in prism coupling, the film parameters are measured at the point of contact, then variations in values of  $W$  calculated from such measurements reflect the underlying film inhomogeneity.

A further source of error is possible in the titania doped films. In such films a buffer layer consisting of  $\text{P}_2\text{O}_5$  doped silica is deposited prior to the core layer deposition, both layers being consolidated at the same time. Observation of the mode lines of such films reveals a decrease in spacing between successive lines. This behaviour is indicative of a graded index profile<sup>7</sup>. As a consequence of this, the values of  $n_f$  and  $W$  calculated from the theory of section (6.2.1) will be in error, since a constant step index profile is assumed. However, values obtained for such films can still be used to indicated trends associated with variations in  $\text{TiO}_2$  doping levels, all other parameters being equal.

#### 6.4.2 COMPARISON OF FILM INDEX RESULTS

One is now in a position to draw together the results obtained for film index from Prism Coupling and EDAX measurements (section 5.6.).

Values of film refractive index can be calculated from the values of doping levels obtained in EDAX measurements. Such values are drawn from previous work carried out by workers dealing with optical fibres,<sup>16</sup> (see section 4.3). It has been assumed in the following analysis that the increase in index arising from each dopant can be simply added to yield the cumulative index increase.

Care must be taken when comparing the measured values of index to those calculated using EDAX. In both cases, average values are measured and are

sensitive to the film parameters at the point of measurement. Since different measurement points have been used in each case, discrepancies in the values obtained are possible.

Batch No.	Dopant	Flow rate /sccm	Doping level /wt%	Calculated Index	Measured Index
67	PCl <sub>3</sub>	160	4.5	1.47	1.4682
64	GeCl <sub>4</sub>	20	—	—	1.4724
58	"	30	2.2	1.4747	—
66	"	48	2.8	1.4754	1.4756
61	"	60	4.5	1.4772	1.4769
62	"	70	5.5	1.4784	1.4774
28	TiCl <sub>4</sub>	12	0.18	1.4726	—
69	"	30	0.28	1.473	1.4716
70	"	60	0.5	1.4735	1.4732
71	"	90	0.82	1.475	1.4736
72	"	120	0.95	1.4775	—
73	"	150	1.26	1.479	—

Figure 6.13 Comparison of refractive index values from EDAX and prism coupling results

### 6.4.3 ESTIMATION OF OPTICAL LOSS

Techniques to measure the optical loss in planar films generally fall into two categories:—

- (1) Measurement of changes in output power taken by coupling guided light out of the waveguide — generally by using an output prism positioned at various points along the waveguide<sup>10</sup>.
- (2) Measurement of the decay in scattered light intensity perpendicular to the plane of the film<sup>17</sup>, as one moves along the waveguide away from the

input coupler following the line of the stripe produce by such scatter

Both methodologies have their advantages and disadvantages. In the first method, one must endeavour to maintain the same pressure between prism and film in order that the difference in coupling encountered when moving the prism does not affect the results. Such a problem can, however, be overcome by using three prisms in which two are used as output couplers<sup>18</sup>.

The second technique assumes the presence of a constant cross-section of scattering centres. The light is scattered out of the waveguide and can be measured using a detector of one form or another. However, positioning of the detector relative to the stripe observed is important, since the detector can register the light scattered from a larger area than that corresponding to the guide width.

Measurements were attempted using the second technique in which the detector used was a HAMMAMATSU camera linked to a TV monitor and HP computer. (See Section 7.4) This technique was chosen in preference to the prism technique because of its simplicity and also because the experimental arrangement to make such measurements was already set up at BTRL where such measurements were made.

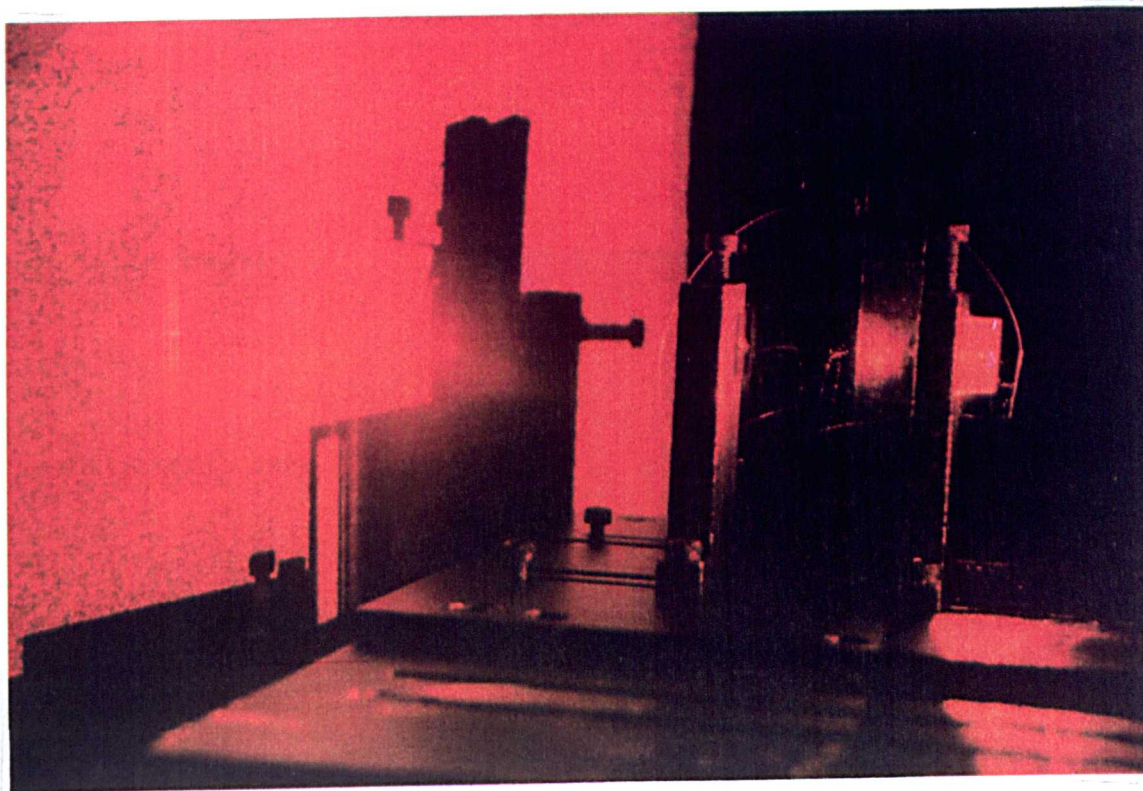
Two film types were examined:—

- (1) ASG films — Arsenic Oxide doped Silica, fabricated at BTRL using the oxidation of silane and arsine (see section 2.1.1)
- (2) Films fabricated by the author

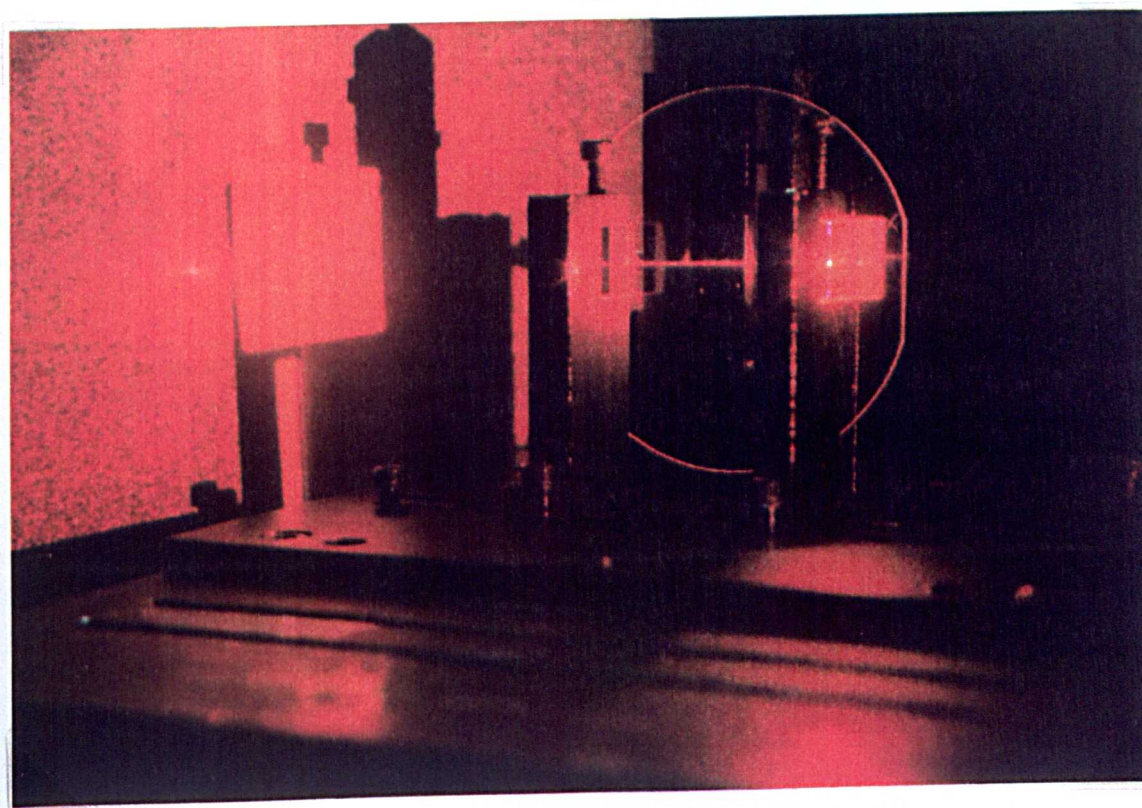
— the examining wavelength of light used was 632.8 nm and in both cases, light was coupled in using a prism and observations of mode lines were used to indicate guidance.

In the first film type a clear stripe was observed from the scattered light. The decay of optical power was measured and a least-mean-squares line fitted to a decaying exponential curve. From this an optical loss figure of the order of 0.5 dB/cm was obtained<sup>19</sup>.

In the author's films, no stripe was visible even though guidance was verified using an output coupler and no sensible result could be obtained. This result suggests that the number of scattering centres per unit cross-section was low, which in turn suggests a low-loss waveguide, assuming Rayleigh scatter to be the predominant loss mechanism.



(b)



(a)

Figure 6.14 Observed scatter for guided modes in planar films  
(a)ASG (b)Ge/P co-doped films

Further attempts to measure planar film loss were not carried out, as the observed result suggested that the films were of sufficient quality to merit further processing. This processing involved the fabrication of ridge waveguides using a combination of photolithography and reactive ion etching (RIE). The following chapter will discuss such work.

## 6.5 CONCLUSIONS

The foregoing section has discussed the basic theory behind, and practice of, planar optical waveguide characterisation. Planar waveguiding theory has been outlined culminating in the derivation of the Transverse Resonance Condition, (T.R.C.) The use of a Prism Coupler to excite guiding modes in the film has been described and the necessary criteria for prism design presented. Thin-film parameter evaluation using measured values of effective index in conjunction with the T.R.C. has been carried out and results given. Problems encountered with the films fabricated by the author centre around inhomogeneous layer thickness in the consolidated films giving rise to inaccuracies in the calculated values for layer index and thickness. The solution to this was discussed in chapter 5 and involves greater control over substrate temperature during deposition. Values of refractive index expected from the measured doping levels are compared with those calculated using the Prism Coupler and are found to be in reasonable agreement considering the inaccuracies encountered in the measurement procedure. With greater precision in Prism Coupling practice greater accuracy can be achieved<sup>15</sup>. An attempt to measure the optical loss using a HAMMAMATSU camera was made on two film types; one, Arsenic Oxide doped silica fabricated at BTRL exhibited a loss of 0.5 dB/cm; the other being the type fabricated by the author had insufficient scatter visible to obtain sensible results using this technique.

## 6.6 REFERENCES

1. P. LORRAIN, D. CORSON  
Electromagnetic Fields and Waves  
Freeman and Co.
2. B.I. BLEANEY, B. BLEANEY  
Electricity and Magnetism  
Oxford University Press
3. D.L. LEE  
Electromagnetic Principles Of Integrated Optics  
Wiley
4. P.K. TIEN  
Appl. Opt., Vol. 10, Nov. 1971, pp2395-2413  
Light Waves In Thin Films And Integrated Optics
5. P.J.R. LAYBOURN, J. LAMB  
Radio And Electronic Engineer, Vol. 51, No.7-8, July-Aug. 1981, pp397-413  
Integrated Optics: A Tutorial Review
6. F.A. JENKINS, H.E. WHITE  
Fundamentals Of Optics  
McGraw-Hill
7. H. KOGELNIK  
Integrated Optics; Ed. T. TAMIR, pp15-81  
Topics In Applied Physics, Vol. 7, Springer-Verlag
8. R.G. HUNSPERGER  
Integrated Optics: Theory And Technology  
Springer-Verlag
9. H.G. UNGER  
Planar Optical Waveguides And Fibres  
Clarendon Press
10. P.K. TIEN, R. ULRICH  
J. Opt. Soc. Am., Vol. 60, No. 10, Oct. 1970, pp1325-1337  
Theory Of Prism-Film Coupler And Thin-Film Light Guides
11. G. H. OWYANG  
Foundations Of Optical Waveguides  
Elsevier
12. R. ULRICH, R. TORGE  
Appl. Opt., Vol. 12, No. 12, Dec. 1973, pp2901-2908  
Measurement Of Thin-Film Parameters With A Prism Coupler
13. A.S. HUANG, Y. ARIE, C.C. NEIL, J.M. HAMMER  
Appl. Opt., Vol. 24, No. 24, 15th Dec. 1985, pp4404-4407

Study Of Refractive Index Of  $\text{GeO}_2\text{:SiO}_2$  Mixtures Using Deposited Thin-Film Optical Waveguides

14.P.K. TIEN, R. ULRICH, R.J. MARTIN

Appl. Phys. Lett., Vol. 14, No. 9, 1st May 1969, pp291-294

Modes Of Propagating Light Waves In Thin Deposited Semiconductor Films

15.H.J. LEE, C.H. HENRY, K.J. OBLOWSKY, R.F. KAZARINOV

Appl. Opt., Vol. 27, No. 19, 1st Oct. 1988, pp4104-4109

Refractive-index Dispersion Of Phosphosilicate Glass, Thermal Oxide, and Silicon Nitride Films On Silicon

16.K.J. BEALES, C.R. DAY

Phys. & Chem. Glasses, Vol. 21, No. 1, Feb. 1980

A Review of glass fibres for optical communications

17.Y. OKAMURA, S. YOSHINAKA, S. YAMAMOTO

Appl. Opt., Vol. 22, No. 23, 1st Dec. 1983, pp3892-3894

Measuring Mode Propagation Losses Of Integrated Optical Waveguides:  
A Simple Method

18.Y.H. WON, P.C. JAUSSAUD, G.H. CHARTIER

Appl. Phys. Lett., Vol. 37, No. 3, 1st Aug. 1980, pp269-271

Three Prism Loss Measurements Of Optical Waveguides

19.S.D. HUBBARD, B.J. AINSLIE, S.A. BAILEY, G.D. MAXWELL

Int. Cong. On Opt. Sci. & Eng., 24-28th April 1989, Paris

Arsenic doped silica as a passive waveguiding material.

In the following chapter, the techniques used to fabricate ridge waveguide structures are discussed. Such techniques involve photolithography, followed by dry etching using the process of Reactive Ion Etching (R.I.E.). Physical analysis of such structures involves etch depth determination and etch quality assessment. Following such assessment, the optical characteristics are determined, which in this case involves measurement of waveguide loss. To this end, two techniques are outlined and the results presented.

As has been the case for chapter 6, the theory involved in this work is outlined as and when the need arises and is of sufficient depth to explain the experiments performed. Discussion of optical ridge waveguide theory in depth has been omitted, since it does not directly contribute to the work carried out.

**7.1 RIDGE WAVEGUIDE THEORY**

Structures which are capable of optical confinement in two dimensions come in a number of forms. Figure 7.1 shows some of the more common types encountered<sup>1</sup>.

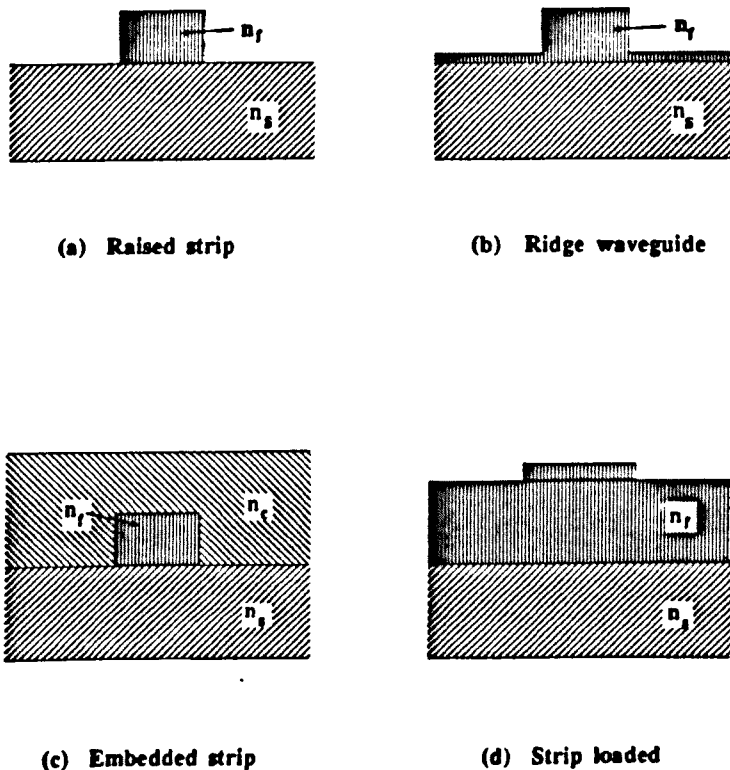


Fig 7.1 Common waveguiding structures used to confine light in 2-D

In all of the waveguide types, confinement is predominantly within the cross-sectional area of the guide, with evanescent fields extending beyond the film boundaries.

As for the planar waveguide structures, optical confinement is a result of total internal reflection, and mode guidance occurs when the necessary phase conditions are satisfied. A simple technique to calculate the guiding properties of such 2-D structures involves considering each direction (x and y) separately. The structure can then be thought of as two planar slab waveguides. This method is known as the Effective Index Method and will be described in the following section.

### 7.1.1 THE EFFECTIVE INDEX METHOD

In this section, the ridge waveguide structure (Fig 7.1(b)) will be discussed. The general structure can be expanded to show the two planar waveguide structures under consideration (Fig 7.2).

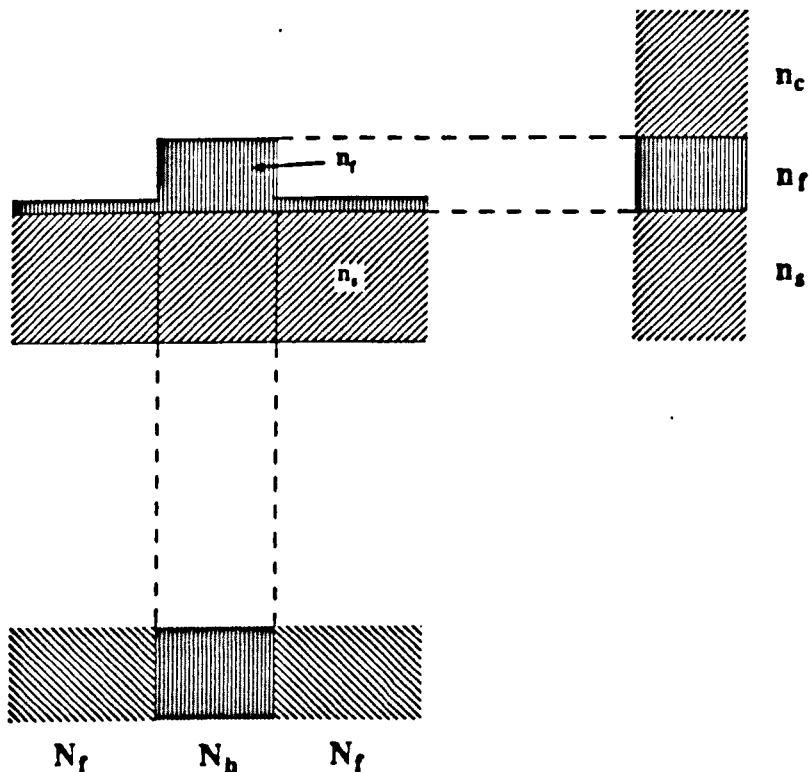


Fig 7.2 Ridge Waveguide Structure expanded to show two planar guides.

We consider the cross-section of the waveguide in the  $x$ -direction consisting of a three-layer planar waveguide with indices  $n_c$ ,  $n_f$  and  $n_s$ . The analysis for this structure is exactly that described in section 6.1.2. The Transverse Resonance Condition (TRC) is equal to:-

$$2n_f k h \cos \theta_i - 2\varphi_c - 2\varphi_s = 2m\pi$$

- where all the terms are as previously defined. As before  $m$  is an integer and describes the mode pattern which exists in the  $x$ -direction.

We now consider the  $y$ -direction, consisting of three areas having indices  $N_f$ ,  $N_h$  and  $N_f$ . These indices are the *effective indices* in the  $y$ -direction and since  $h > f$ , then  $N_h > N_f$ .

Exactly the same analysis can be applied as has already been used so long as the effective index values are used. Consequently we obtain:-

$$2N_h k W \cos \theta'_i - 2\varphi - 2\varphi = 2l\pi$$

- where  $l$  defines the mode order in the  $y$ -direction. In this case, we have a symmetrical waveguide structure in which the 'cladding' and 'substrate' index are equal. Thus:-

$$2N_h W k \cos \theta'_i - 4\varphi_f = 2l\pi$$

where  $\varphi_f$  is given by

$$\varphi_f = \tan^{-1} \frac{(N_h^2 \sin^2 \theta'_i - N_f^2)^{\frac{1}{2}}}{N_h \cos \theta'_i}$$

The actual mode description for the ridge waveguide is obtained from a description of the electromagnetic field polarisation used (TE or TM) with a subscript describing the mode order, ie  $TE_{lm}$  or  $TM_{lm}$ , for example,  $TE_{01}$ , in which there is a zeroth order mode in the  $y$ -direction and a first order mode in the  $x$ -direction.

The field patterns arising from such mode distributions are schematically shown in Figure 7.3. Such field patterns can be calculated from solutions to the 2-D Wave Equation<sup>2,3</sup>.

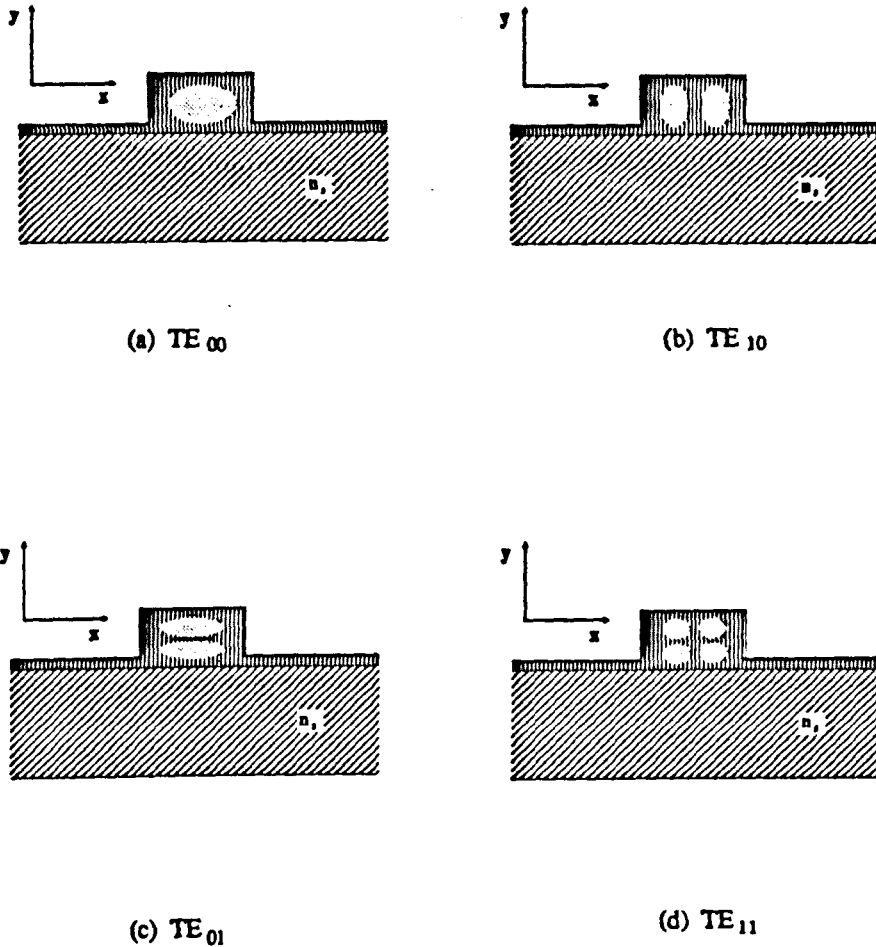


Figure 7.3. Mode Patterns In Ridge Waveguide Structure

## 7.2 PHOTOLITHOGRAPHY

The following section will describe the basic elements involved in the photolithographic process and will include a description of resist and mask types available. The adopted procedures will be described and the results obtained will be presented.

### 7.2.1 BASIC CONCEPTS

Photolithography is a standard pattern definition process used in the electronic industry<sup>4</sup>, and now finds application for the generation of patterns in optical circuits. The main elements used in the process are shown schematically in Figure 7.4.

The process involves the exposure of selected parts of an optically sensitive polymer coating the planar film through a mask in which the pattern to be transferred is defined by optically opaque areas. In order to achieve accurate pattern reproduction of very small features it is desirable to minimise the diffraction of the light between the mask and photoresist. To this end, the mask/sample separation ( $d$ ) should be small, and in practice the mask is placed in contact with the surface of the photoresist, such lithography being termed contact printing.

Once the photoresist has been exposed, it is developed and the pattern revealed. There are four cases possible, depending on the type of photoresist used and on the type of mask used.

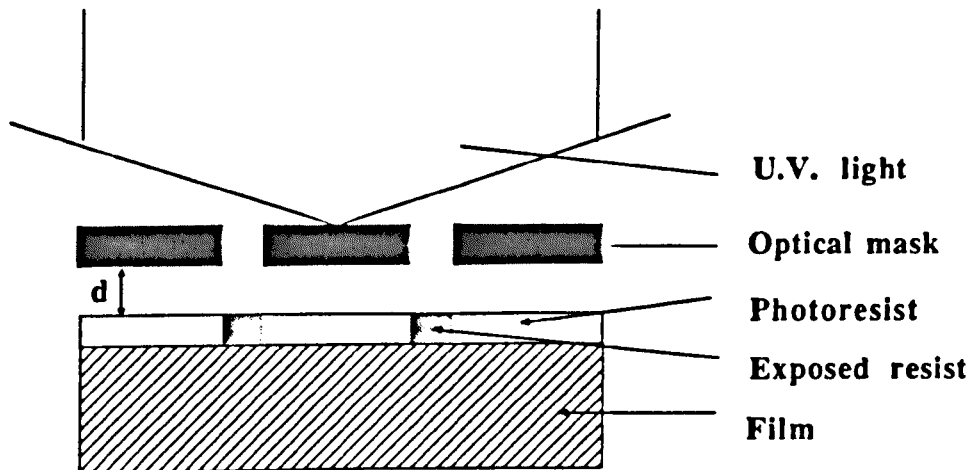
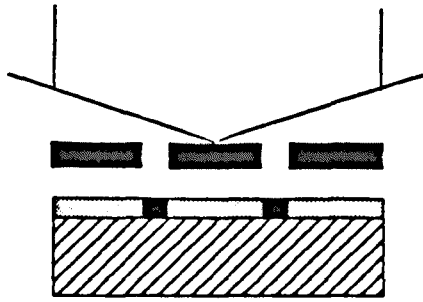


Figure 7.4 Schematic showing main elements used in photolithography

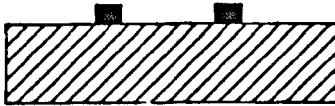
1. Positive photoresist, in which the exposed resist becomes more soluble
2. Negative resist which becomes less soluble after exposure
3. Use of a light-field mask, in which the desired pattern is defined by the optically opaque areas
4. A dark-field mask, in which the pattern is defined by the transparent areas

In practice, only the positive photoresist was used by the author, with a combination of light and dark field masks.

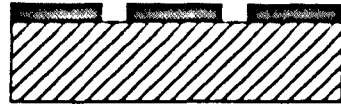
Once exposed and developed, the remaining photoresist can be used as a mask to protect the underlying film during the etching stage. Alternatively a metal mask can be deposited on top of the film and photoresist areas. The photoresist can



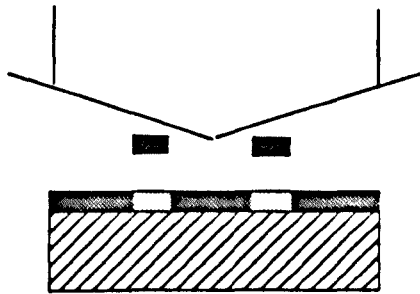
(a) Dark field mask



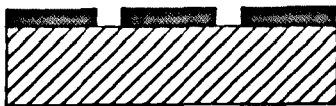
Negative resist - exposed area remains after developing



Positive resist - unexposed area remains after developing



(b) Light-field mask



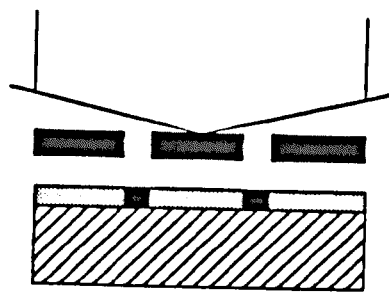
Negative resist - exposed area remains after developing



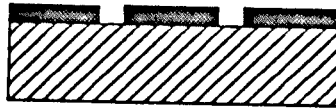
Positive resist - unexposed area remains after developing

Figure 7.5 Schematic of resist/ mask combinations

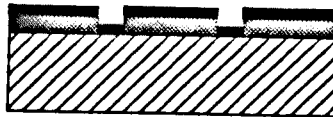
then be removed, taking with it the metal layer on top of the resist areas. This leaves the remaining metal mask behind. This step is called *lift-off* since the metal is lifted off with the resist.



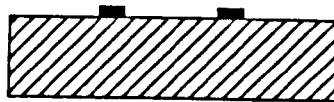
(a) Exposure



(b) Develop



(c) Metal overlay



(d) Lift-off

Figure 7.6 Schematic of lift-off

If we consider the case where positive photoresist is being used, then the lift-off stage will be applicable with a dark field mask. After etching, the metal layer can be removed to leave the etched pattern behind.

## 7.2.2 PHOTOLITHOGRAPHIC PRACTICE

The photolithographic practice describes the stages used by the author to prepare the samples: the procedure for photoresist coating, the exposure and development of the resist, and the added steps required in lift-off.

The sample preparation prior to coating with photoresist can play an important role in determining the quality of the photolithography. Any residues of grease or other contaminants can affect the adhesion of the resist and any particulate contaminants can lead to uneven contact between the optical mask and the surface of the photoresist.

Consequently the following procedure was adopted:-

- 1 Wash samples in GENKLENE
- 2 Three minutes in ultrasonic bath (ub) in GENKLENE
- 3 Wash in ACETONE
- 4 Three minutes in ub in ACETONE
- 5 Wash in METHANOL
- 6 Three minutes in ub in METHANOL
- 7 Rinse in METHANOL
- 8 Blow dry with nitrogen and dry on hotplate

Once cleaned and dried the samples can be coated with photoresist

The general technique used to coat the samples with photoresist is spinning. The sample is placed on a variable speed rotating stage and held in place by suction from a vacuum pump. A quantity of photoresist is dripped onto the sample surface through a filtering syringe and the sample spun at a pre-determined rate for a fixed time. This then results in a film of resist of a particular thickness predominantly determined by the spin speed.

If the cleanroom environment used is not humidity controlled, then a resist primer is spun onto the sample prior to using the resist to remove any moisture on the sample. Details of resist used, spinning data and time are in Figure 7.7.

Parameter	Value
Resist Primer	Hexamethyl diisilazine (HMDS)
Photoresist	ShIPLEY 1450J
Spin speeds	4000 rpm
Spin time	30 s
Pre-bake temperature	90°C
Pre-bake time	30 mins

Figure 7.7 Typical parameters involved in resist spinning

Once spun, the resist is given a pre-bake of approximately 30 minutes at 90°C to dry the photoresist.

A further refinement is beneficial if a dark field mask is used and lift-off required, involving an extra stage prior to exposure. Instead of the 30 minutes pre-bake, a 15 minute pre-bake is used, followed by a 15 minute soak in CHLOROBENZENE, with a further 15 minute pre-bake at 90°C. This has the effect of speeding the removal of the metal coated resist.

Two masks were available to define the straight line patterns used. One, being a light field mask, consisting of a set of 7 lines, 3 inches long of sizes 6µm, 8µm, 14 µm, 18 µm, 22 µm, 36 µm, 50 µm with line spacings of 1000 µm. The other mask was a dark field mask patterned with three sets of lines of sizes 1,2,3,4, and 5 µm, 2½ inches long with line separation of 100 µm and pattern separation of 1 mm. Consequently, lift-off was required when patterning the 1 → 5 µm lines.

Sample exposure was carried out using a Hybrid Technology Group (HTG) mask aligner. Here the sample was exposed through the mask using ultra-violet light for a pre-set time, the exposure time being empirically determined by the thickness of resist used.

Once exposed, the sample was developed. The time for development was again determined through trial and error, and was related to resist thickness and exposure times. After this stage the sample was given a post-bake at 120°C for approximately twenty minutes to harden the developed resist remaining. Typical parameters are summarised in Figure 7.8 corresponding to the resist spinning parameters used.

Parameter	Value
Exposure time	6-10 seconds
Developer	1:1 Shipley AZ Developer:Water
Developing time	60 s
Post bake temperature	120°C
Post bake time	20 mins

Figure 7.8 Typical Exposure Parameters

Once exposed and developed, the samples were ready for etching.

### 7.3 REACTIVE ION ETCHING (RIE)

The process of RIE is similar in concept to sputter etching, in which a high voltage is established between two electrodes and a plasma discharge is induced with a Radio Frequency (RF) field. Ionic species are generated in the plasma and are accelerated to the electrode on which the substrates are placed<sup>4</sup>. The ionic species impact on the surface of the sample and material is removed by a transfer of momentum. With Reactive Ion Etching (RIE), a molecular discharge is induced. In this way, the surface atoms are sputtered by reactive molecular ion species and yield a *volatile compound*,<sup>5</sup>. Typical gases used in the process include  $\text{CHF}_3$  and  $\text{C}_2\text{F}_6$ .

The process is carried out at low pressures, typically 20 mTorr and uses low etch gas flow rates often of the order of 15 sccms. A typical chamber configuration is shown schematically in figure 7.9.

The system requirements include:—

- 1 Etch anisotropy
- 2 Large film etch rate
- 3 Etch rate of film  $\gg$  etch rate of mask

It is also important to avoid polymer re-deposition, where organic molecular species of a non-volatile nature are formed in the plasma and are deposited on the film surface. Such re-deposition is found to depend on the carbon/fluorine ratio<sup>6</sup>, and is exacerbated by exposed metal surfaces inside the chamber<sup>7</sup>.

With careful selection of etch gases or gas mixtures, and etch chamber design, the aforementioned problems can be reduced.

The parameters adopted to etch the ridge waveguide structures are typical for RIE. The main points of interest are detailed in Figure 7.10. All samples were mounted on a 4" silicon wafer on top of the table electrode, to reduce re-deposition.

Etch times would typically be  $\approx$  60 minutes which gave an etch depth of 2  $\rightarrow$  2.4  $\mu\text{m}$ . This gives an etch rate of 330  $\rightarrow$  400 Angstroms/min.

Generally, the deposited films were  $\text{GeO}_2$  doped with a layer thickness of 2.4  $\mu\text{m}$ , with the result that the film would be completely etched away.

Once etched, the remaining mask material was removed, the etchants used for this purpose depending on the mask material. For photoresist masks, a 5:1 mixture of sulphuric acid:hydrogen peroxide was suitable. Alternatively, plasma etching using Oxygen was just as effective. With the aluminium masks, an etch consisting of Phosphoric acid ( $\text{H}_3\text{PO}_4$ ), nitric acid ( $\text{HNO}_3$ ), and water in the ratio of 16:1:2 was

found to be suitable.

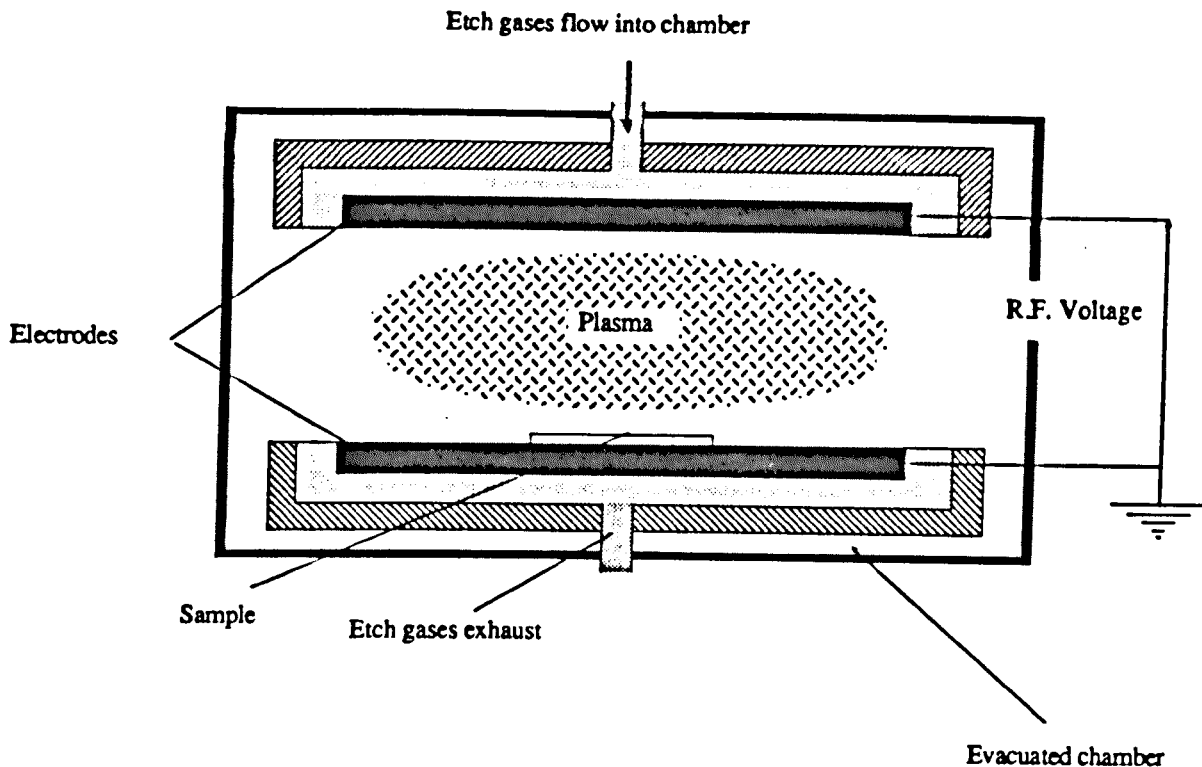


Figure 7.9. Typical Etch Chamber schematic

Etch Gases	Flow Rates /sccm	Etch Pressure /mTorr	RF Power/W		DC Self Bias /V
			FWD	RVS	
CHF <sub>3</sub>	15	12→25	100	0	200→250
CHF <sub>3</sub> /Ar	15/15	"	"	"	"

Figure 7.10 Parameters used in RIE

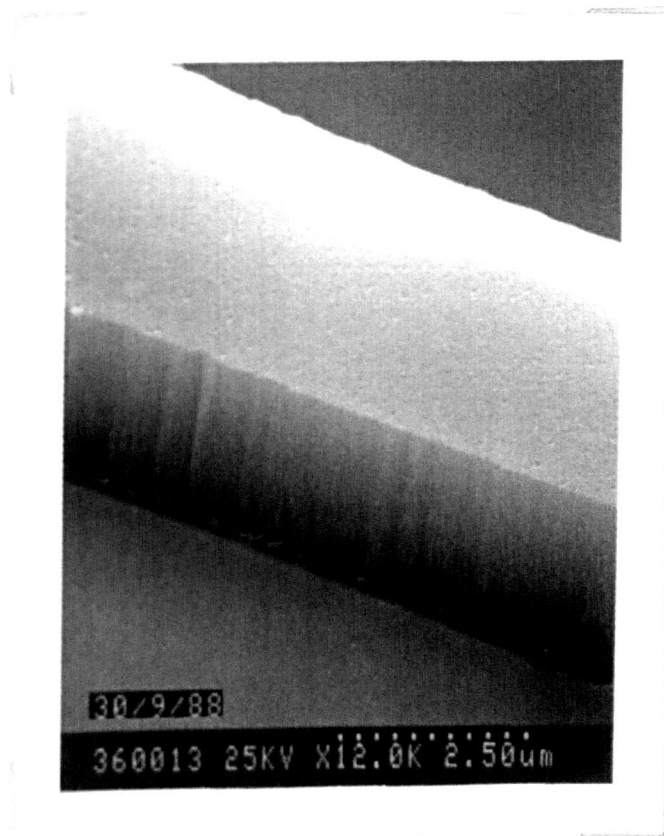
Assessment of the etched waveguides was carried out using Talystep measurements to determine etch depth and SEM analysis to look at the etch quality of the ridge walls, the desired result being vertical, smooth walls (smooth meaning

that the scale of the wall irregularities induced  $\ll$  wavelength of guided light used). Figure 7.11 summarises some of the etching results and includes the salient etch parameters.

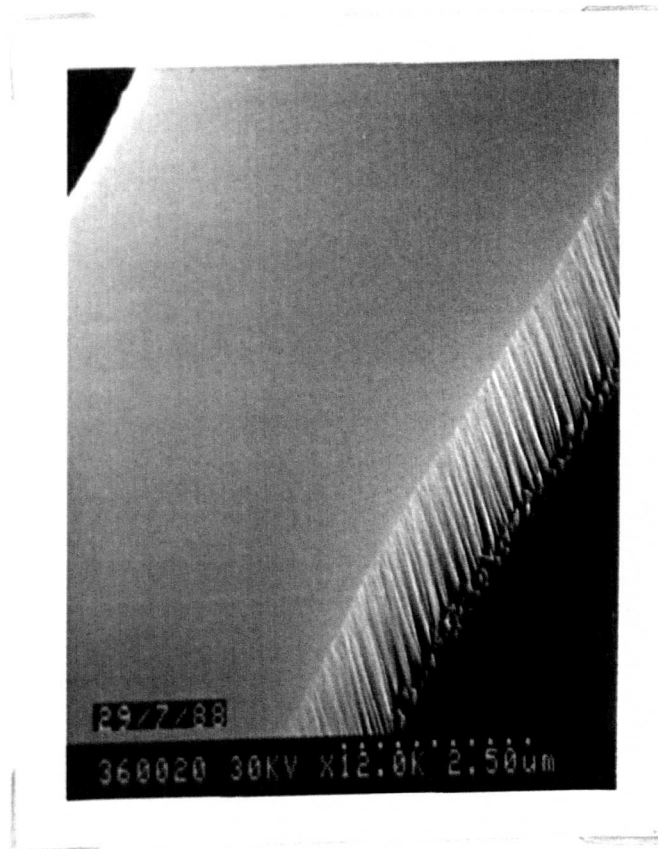
Batch	Etch Gases	Etch Pressure /mTorr	Gas Flows /sccm	RF Power/W		DC Self Bias /V	Etch Time /min	Etch Depths / $\mu$ m
				FWD	RVS			
77	CHF <sub>3</sub>	13.5	15	100	0	240	60	2.40
78	CHF <sub>3</sub> /Ar	19.5	15/15	100	0	230	60	2.35
45	CHF <sub>3</sub>	12.3	15	100	0	270	120	4.20
96	CHF <sub>3</sub>	24.5	35	100	0	200	60	1.30
97	CHF <sub>3</sub>	12.0	15	100	0	200	60	2.20
97	CHF <sub>3</sub> /Ar	19.8	15/15	100	0	250	60	2.40

Figure 7.11 Summary of main results

The quality of etch as regards wall roughness is represented in Figure 7.12 using SEM photographs.



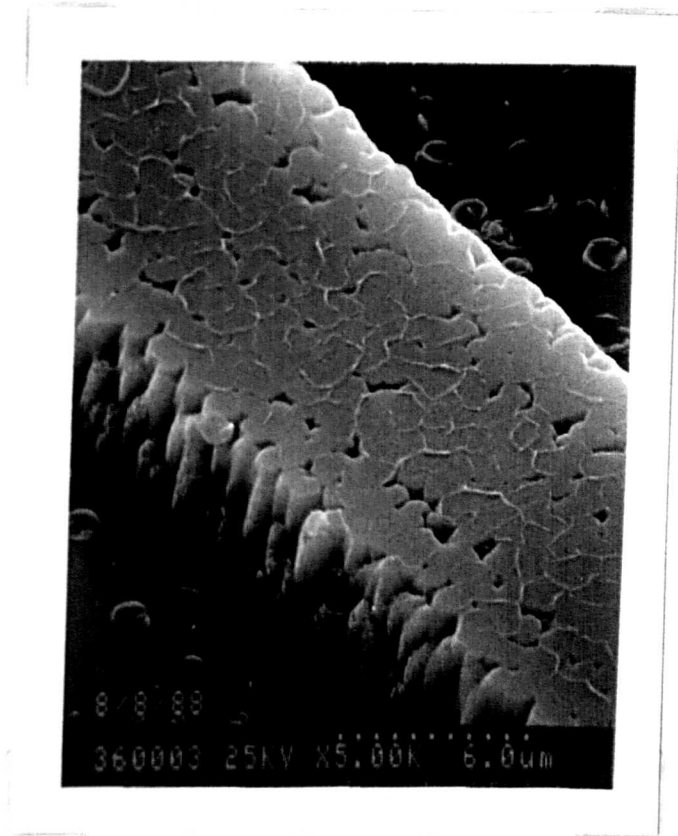
(a)



(b)

Figure 7.12 SEM photographs of etch quality

(a)The Good, (b)The Bad and (c)The Ugly



(c)

Figure 7.12 SEM photographs of etch quality

(a)The Good, (b)The Bad and (c)The Ugly

## 7.4 LOSS MEASUREMENT TECHNIQUES

Both techniques to measure the optical loss in the ridge waveguide structures used *end-fire* launching. It is therefore instructive at this point to give a brief description of the necessary sample preparation, and the experimental arrangement required, before describing the loss measurement techniques used.

End fire launching entails focussing the laser light onto the polished end face of the ridge waveguide. In order to do this, one requires:-

- 1 Polished facets at the ends of the waveguide
- 2 Focussing lenses and positioning equipment to place the polished facet at the beam focus

Sample preparation involved cutting the etched films perpendicular to the waveguides into suitably sized pieces (approx 25mm), using a diamond saw. Once cut, the samples were bonded to a glass support using Shellac prior to an initial 'roughing down' of the end faces on a cast iron plate using 600 grit silicon carbide powder. This process lasted until the damage produced by the diamond saw had been removed. Further polishing on a brass plate using 3  $\mu\text{m}$  aluminium oxide abrasive removed the scratches left by the roughing stage to produce a semi-polished facet. The final polishing stage is on an expanded polyurethane bowl plate with a colloidal silica liquid. Visual inspection was carried out periodically using an optical microscope to assess the polish quality.

Once polishing was complete, the samples were removed from the glass supports by gently heating and Shellac residues were cleaned with methanol.

The components involved in end-fire launching are depicted schematically in figure 7.13. The laser beam was focussed by the lens and the waveguide positioned at the focal point.

The focussed beam provided a range of wavevectors which coupled into corresponding modes in the waveguide. The modes which could not be sustained, coupled out of the guide as radiation or substrate modes<sup>9</sup>.

Since a significant amount of work is involved in fabricating waveguiding structures it is desirable to use non-destructive techniques to measure the film parameters. Two such techniques were investigated.

- 1 Video camera technique<sup>10</sup> - measures the light scattered out of the waveguide
- 2 Fabry-Perot cavity technique<sup>11,12,13</sup> - measures cavity resonances

induced by heating the sample whilst supporting a guided mode.

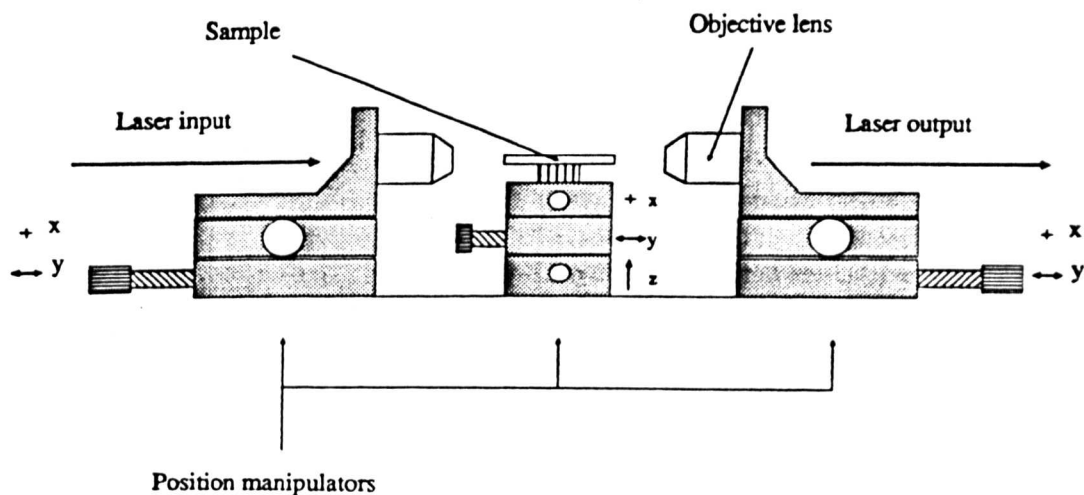


Fig 7.13 Schematically depicts the components used in end fire

#### 7.4.1 VIDEO CAMERA TECHNIQUE

This technique is a simple, semi-automatic process which can be applied to measure the optical loss in both planar and ridge waveguide structures.

A video camera is used to record the light scattered perpendicularly from the waveguide, and to convert the analog data to a digital signal which is then processed by a computer. Figure 7.14 details the typical experimental arrangement used for the ridge waveguides. The same arrangement can be used for planar films by replacing the end-fire arrangement with that used for prism coupling.

The camera used was a HAMMAMATSU TV, Ltd, AIS8. The camera control unit included an A-D converter which fed the signals to an HP 9836 microcomputer and to a TV monitor. The parameters which could be varied from the computer included the length and position of the sampling line scanned by the camera. The sampling line could be positioned transverse to or colinear with the ridge waveguide. In practice, positioning the line colinear with the waveguide was nontrivial and gave no profile information for the scattered light. Consequently the sampling line was positioned transversely across the streak and the width of the scan line reduced until it was comparable to the observed streak width. This helped reduce the amount of stray scattered light entering the sampling line and contributing to measured intensity.

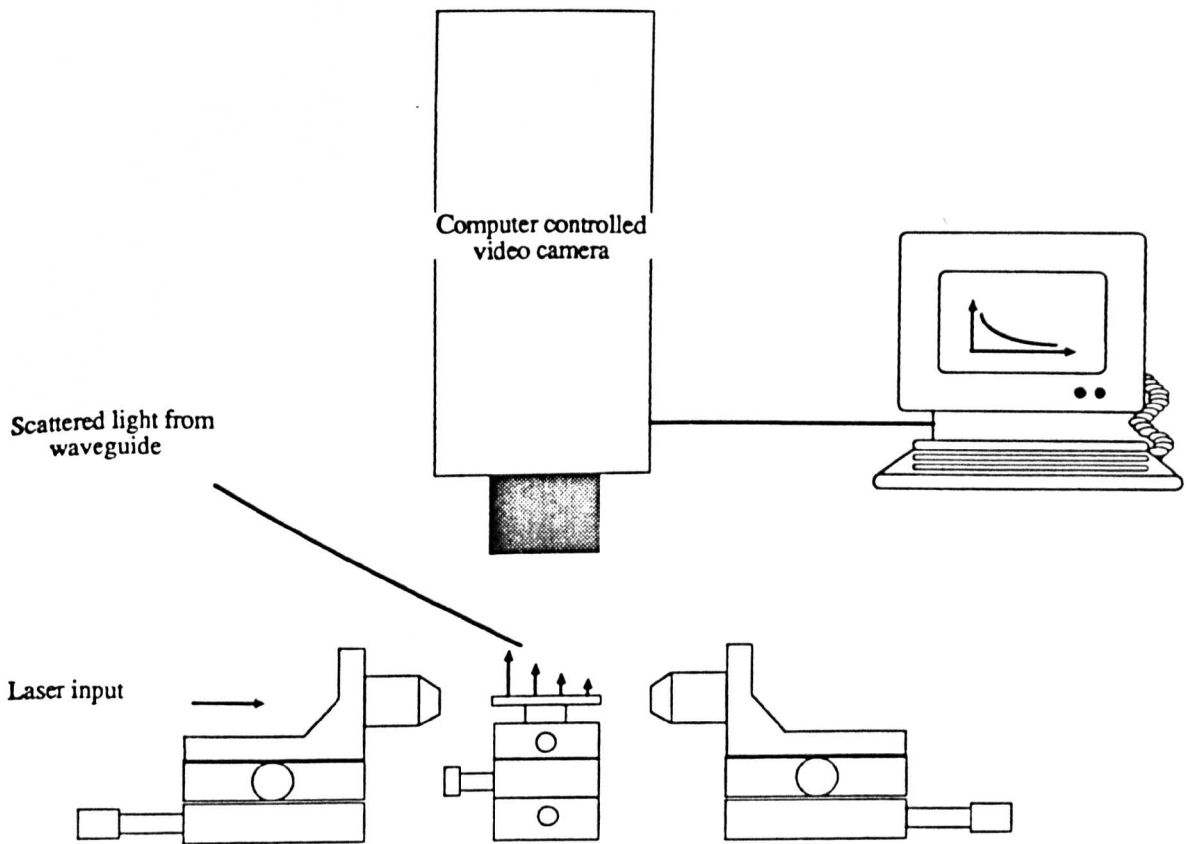


Figure 7.14 Experimental Arrangement for Loss Measurement

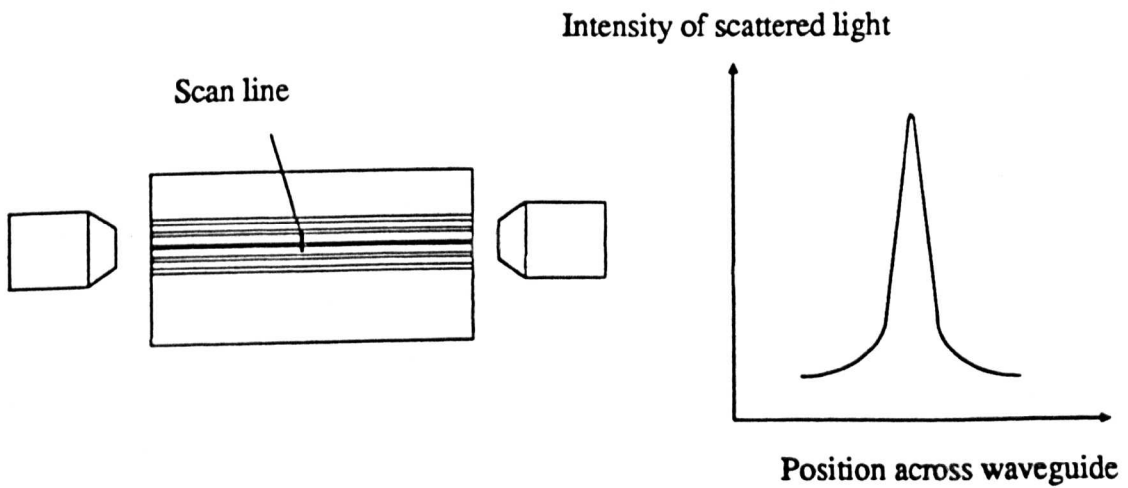


Figure 7.15 Positioning of line across waveguide with schematic showing type of output

The scan line is moved along the programmed scan length, and records the intensity decay in the scattered light. This intensity data is processed using the microcomputer, and a least-squares-fit to a decaying exponential is applied to the results, the slope of which yields the propagation loss.

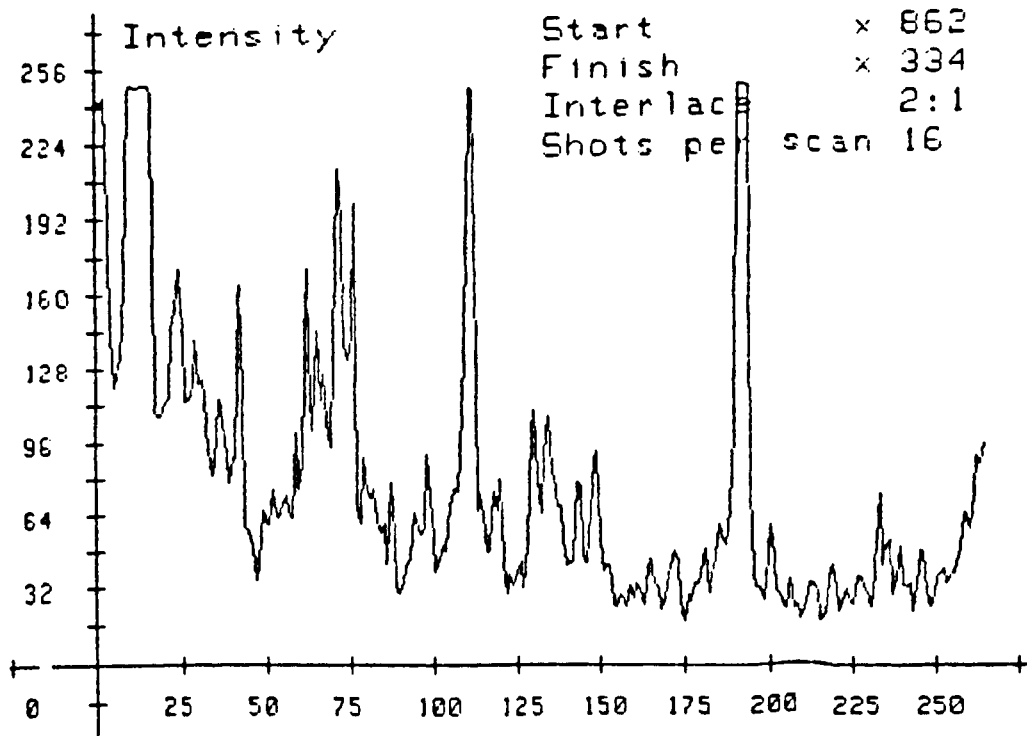
Film Type	Scan Length /cm	Loss dB/cm
ASG	(a) 0.55	3.53
	(b) 0.50	0.49
	(c) 0.54	- 1.15
Ge/P doped silica	(d) 1.29	5.19
	(e) 0.86	2.53
	(f) 0.561	0.2

Fig 7.16 Typical results produced from video camera technique on the two film types encountered (see Sections 2.1.1 and 6.4.3 for concerning ASG fabrication and planar assessment)

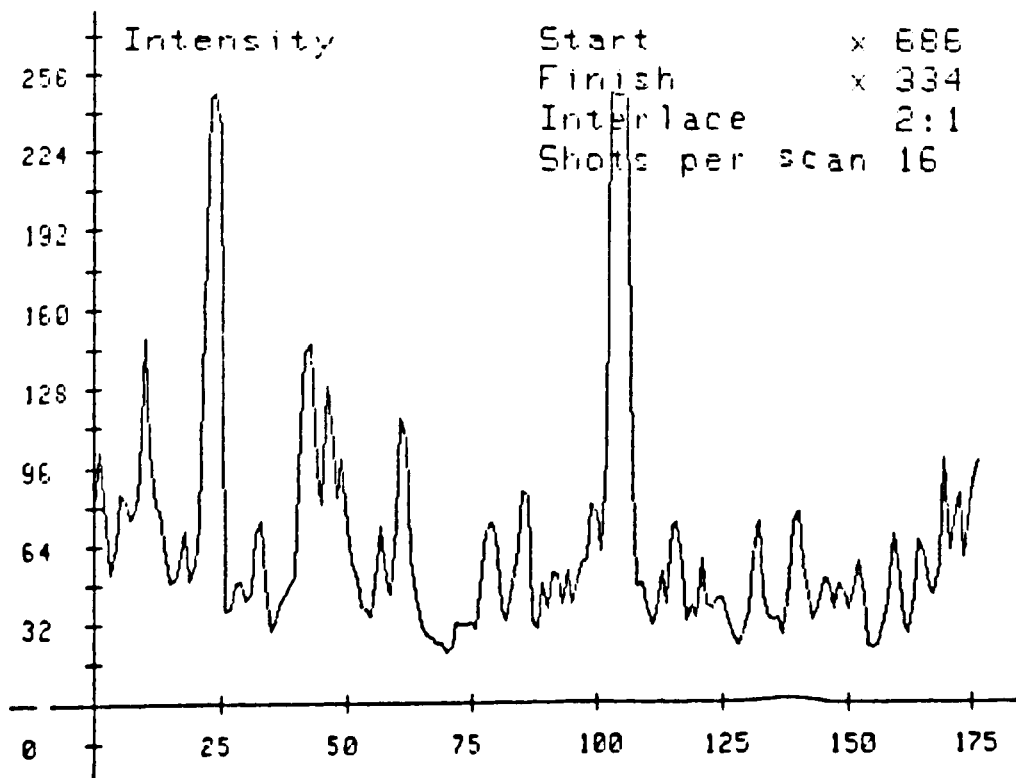
From the results in figure 7.18 we see that the loss obtained can vary by a factor of 10 or more depending on the scan length used, ( 5.19 dB over 1.29 cm in 7.16 (d) to 0.2 dB over 0.561 cm in 7.17 (f)).

The major problem associated with this technique is the effect produced by stray scattered light. This can include light scattered from random scattering centres on or near the waveguide, as well as scatter from the substrate.

This presents a serious drawback when measuring low-loss waveguides where the background scatter is comparable to the waveguide scatter. Figure 7.17 details two scans taken from the same sample. In one, the sample has been moved so that no light is coupled into the waveguide and the trace displays the level of background scatter. In the other, a mode is propagating down the waveguide and the trace is a measure of light scattered from the guided mode plus the background scatter. The traces also show the intensity spikes from random scattering centres on or near the waveguide. Such spikes can dramatically affect the value of loss obtained from a least-squares-fit to the data. By carefully arranging the starting and finishing points for the scan length around such intensity spikes, one can tailor the loss obtained. In some cases one can even record gain, as in 7.16 (c).



(a) Longest scan



(b) Middle length scan

Figure 7.17 Three scans with varying scan lengths showing change in calculated loss

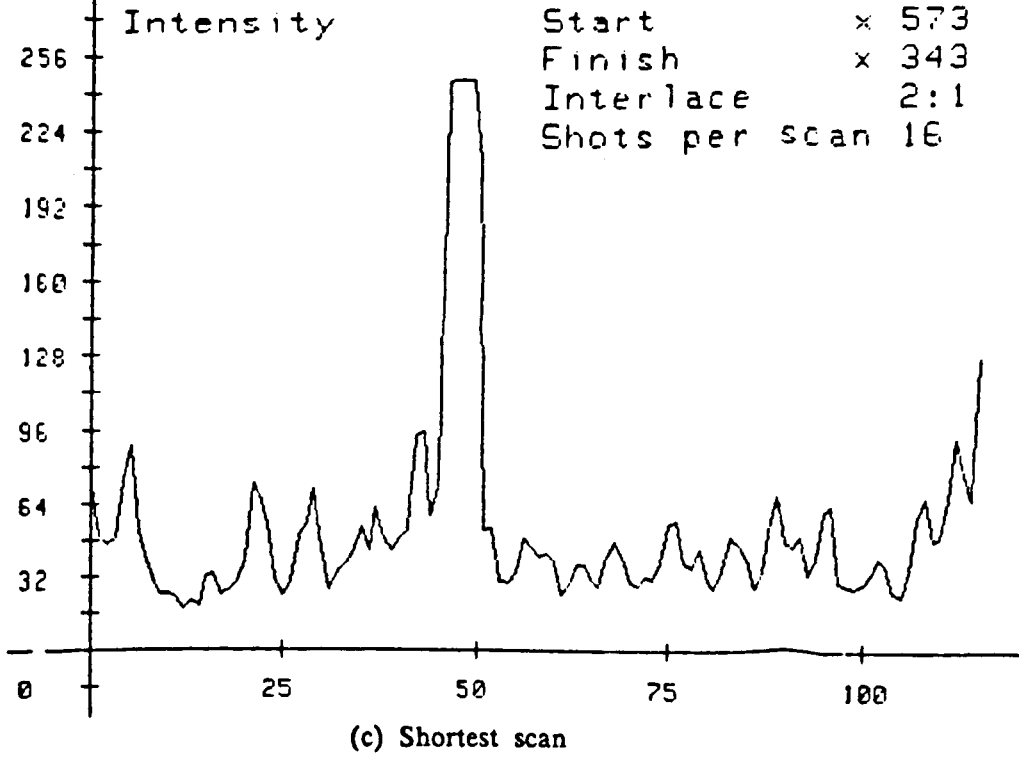
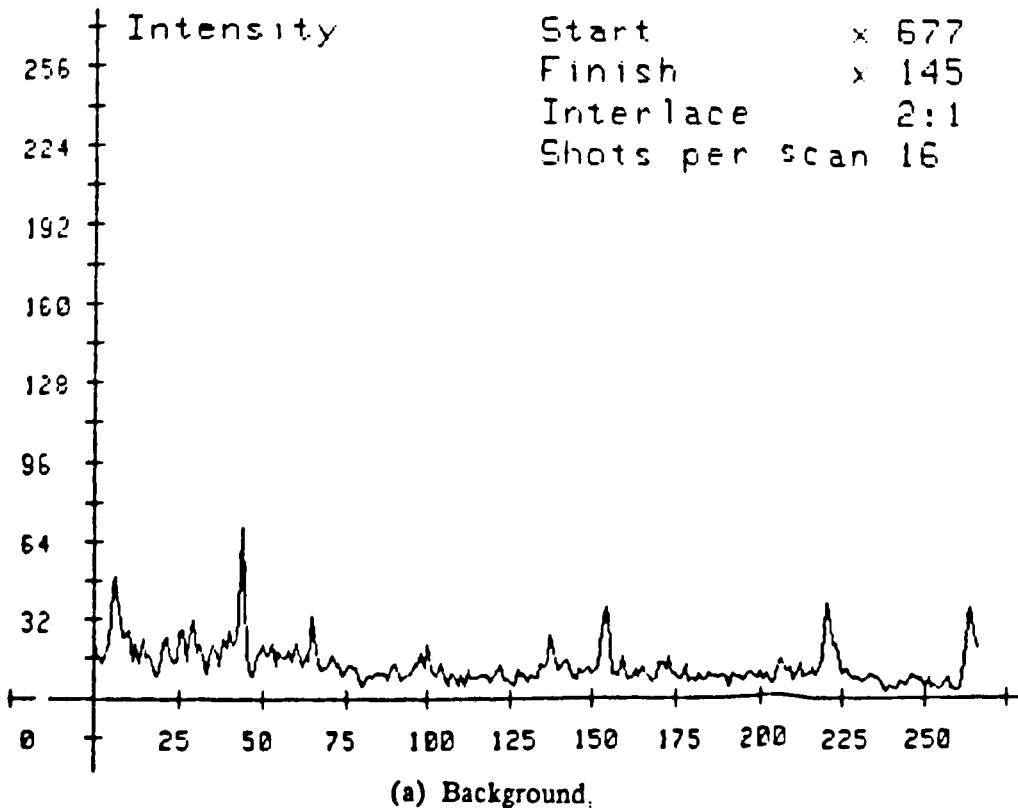
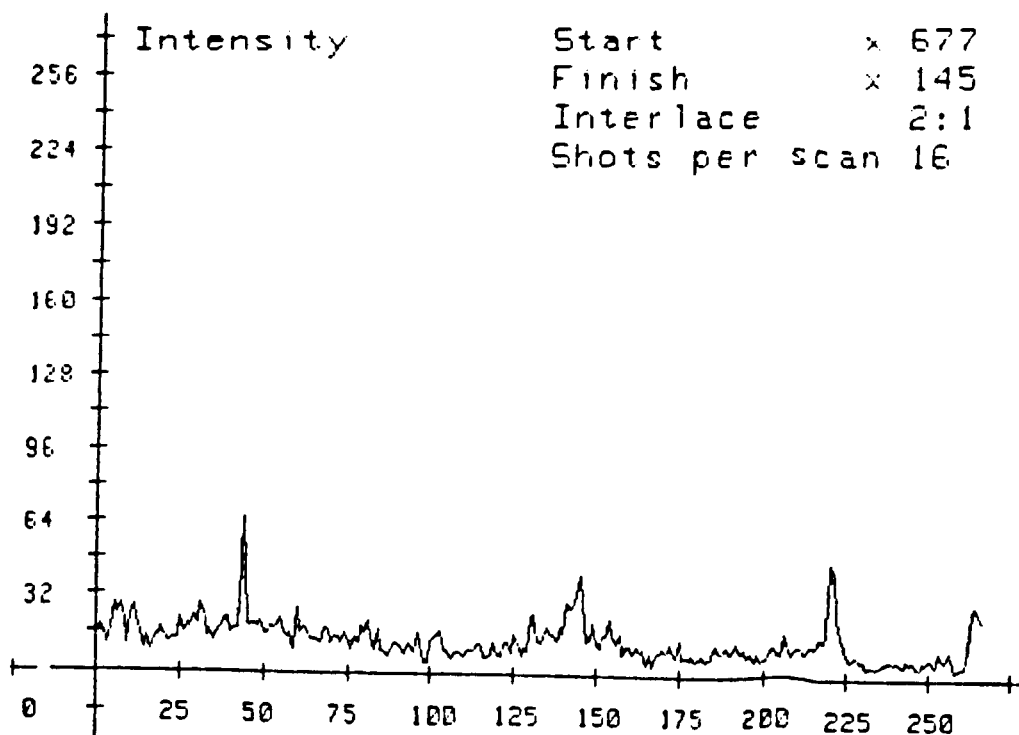


Figure 7.17 Three scans with varying scan lengths showing change in calculated loss

The problem of background scatter was encountered when a silica substrate was used. Films deposited on silicon did not exhibit such scatter at 632.8 nm. This problem could be surmounted by index matching the sample to a silica block, the back surfaces of which had been painted matt black.





(b) Guiding

Figure 7.18 Two scans - (a) Background, (b) Guiding

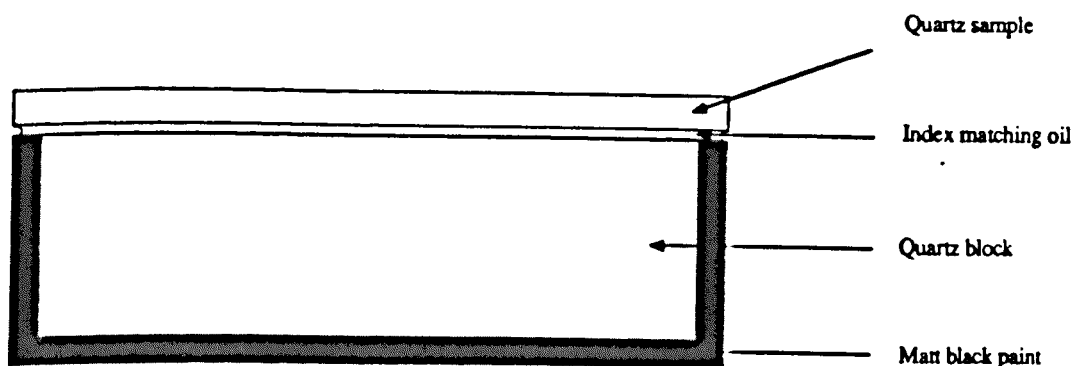


Figure 7.19 Schematic of arrangement used to eliminate substrate scatter

This eliminated the background scatter allowing more accurate scans to be made. However, the problem of intensity spikes remained. Such spikes are the result of random scattering centres, and can be caused by dust or contamination introduced during the waveguide fabrication stages (especially etching and polishing).

This problem is more an artifact of the measurement technique rather than an

inherent loss factor, for although the scattering centres are part of the physical environment in which the light propagates, when they are not in contact with the waveguide itself they can scatter light which has already been scattered from the waveguide. The effect of such spikes is reduced with increasing scan lengths, since their contribution is less important. However, the sample lengths of films fabricated by the author were of the order of 10–20 mm. In such cases this technique is potentially unreliable.

#### 7.4.2 FABRY-PEROT CAVITY RESONANCE TECHNIQUE

This technique uses a Fabry-Perot Cavity formed by the waveguide itself, to determine the waveguide loss. Resonances are induced by heating the waveguide which causes an increase in the optical path length of the structure, a result of which the cavity passes through resonant and antiresonant positions producing the observed oscillations.

##### 7.4.2 (1) DERIVATION OF THE EXPRESSION FOR LOSS

It is a straightforward procedure to calculate the transmission characteristics of a Fabry-Perot interferometer<sup>11</sup>. If one then includes a term for optical attenuation, one obtains an expression of the form:-

$$T = \frac{\gamma^2 I_0}{(1 - \gamma^2 R)^2 + 4\gamma^2 R \sin^2(\varphi/2)}$$

- where T is the transmitted intensity,  $I_0$  is the effective input intensity (which includes terms relating to coupling efficiency),  $\gamma$  is the single pass wave amplitude reduction factor, R is the power reflection coefficient and  $\varphi$  is the phase difference which equals  $2\beta L$ .

The resonant ( $T_R$ ) and antiresonant ( $T_A$ ) transmissions are given by<sup>13</sup>:-

$$T_R = \frac{\gamma^2 I_0}{(1 - \gamma^2 R)^2}$$

$$T_A = \frac{\gamma^2 I_0}{(1 + \gamma^2 R)^2}$$

With a knowledge of the value of  $R$ , the single pass loss  $\Gamma$  can be obtained from the ratio of  $T_R$  and  $T_A$ . That is:-

$$K = T_R / T_A$$

Expressing this in terms of  $\gamma^2$  yields :-

$$\gamma^2 = \frac{1}{R} \frac{\sqrt{K} - 1}{\sqrt{K} + 1}$$

The loss is thus :-

$$\Gamma = -20 \log_{10} \gamma$$

$$\Gamma = -10 \log_{10} \left[ \frac{1}{R} \frac{\sqrt{K} - 1}{\sqrt{K} + 1} \right]$$

#### 7.4.2 (2) EFFECT OF NON-PARALLEL FACETS

If the cut and polished facets are not parallel, but are inclined at some angle  $\theta$  relative to each other, then an additional phase increment  $\delta$  will be introduced upon reflection. In order to assess the permissible limits for non-parallelism, an overlap integral was calculated between an assumed Gaussian profile of the fundamental mode and a phase factor describing the phase increment introduced by non-parallel facets. This analysis does not take into account changes in reflectivity with facet angle, although such analysis has been published subsequent to this work<sup>14</sup>. However the analysis gives an indication of the tolerances required in the cutting and polishing stages.

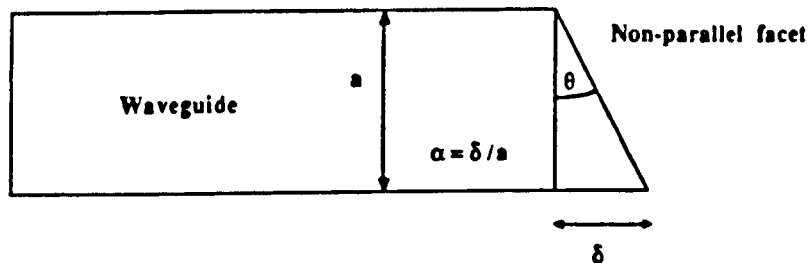


Figure 7.21 Schematic of problem

The normalised Gaussian profile, with standard deviation equal to the guide width  $a$ , is given by:-

$$U(x) = \left\{ \frac{1}{a/\pi} \right\} e^{-\frac{x^2}{2a^2}}$$

- where the normalisation factor is calculated for power,  $U(x)^2$  from:-

$$\int_{-\infty}^{\infty} U(x)^2 dx = 1$$

The phase factor introduced by the non-parallel facets is given by:-

$$\Phi(x) = e^{-i\alpha x} dx$$

- where:-

$$\alpha = \delta / a$$

The overlap integral is calculated in terms of power,  $U(x)^2$  and involves evaluating the integral:-

$$\Gamma = \int_{-\infty}^{\infty} \left[ \left\{ \frac{1}{a/\pi} \right\} e^{-\frac{x^2}{2a^2}} \right]^2 e^{-i\alpha x} dx$$

Which is the Fourier transform of a Gaussian function.

This integral can be calculated analytically by standard means, to give:-

$$\Gamma = e^{-\frac{\alpha^2 a^2}{4}}$$

Values calculated for  $\Gamma$  are given below using parameters encountered in practice. The facet angle can be calculated from the expression:-

$$\delta = a n_f k \tan \theta$$

- where  $n_f$  is the film index,  $k = 2\pi/\lambda$ ,  $a$  is the guide width and  $\theta$  the facet angle.

$\delta$	$e^{-\frac{\alpha^2 a^2}{4}}$	$\theta/\text{deg}$
$\pi/8$	0.962	0.286
$\pi/4$	0.857	0.573
$\pi/2$	0.539	1.145
$\pi$	0.084	2.29

Figure 7.22 Calculated values for facet angle tolerances

Hence, only small facet angles can be tolerated before the power level falls appreciably. This result will be the likely limitation on the applicability of this loss measurement technique.

The field lost on reflection from an angled facet will couple to radiation modes, resulting in a higher loss figure being measured for the waveguide than is actually present.

#### 7.4.2 (3) EXPERIMENTAL ARRANGEMENT

The experimental arrangement used is schematically represented in Figure 7.33

A current is passed through the wire wound resistor, producing heat which is absorbed by the waveguide, leading to thermal expansion and cavity resonances. The guided mode is observed using a HAMMAMATSU camera, and intensity oscillations recorded using the chart recorder.

#### 7.4.2 (4) RESULTS

In practise, convincing oscillations, (to people other than the author), could not be observed in the silica waveguides because the reflectivity from the facets was too low ( approx 4%). However, the reflectivity of the facets could be increased by coating with aluminium. To do this, the sample was bonded, waveguide side down, to a silica block using wax. The ends of the waveguide protruded very

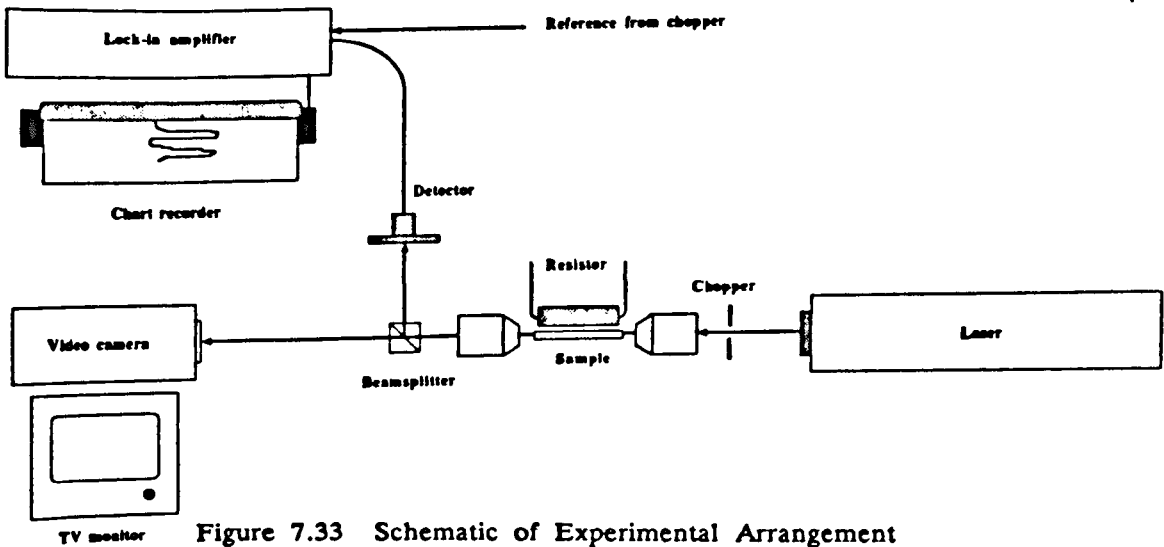


Figure 7.33 Schematic of Experimental Arrangement

slightly over the edge of the silica block to allow the exposed ends to be cleaned, and the bonding wax coating the facets removed. Visual observation was periodically carried out using a microscope to determine when the waveguide facets were clean. The sample and block were then placed inside an evaporator and the polished sample edge coated with aluminium. This process was repeated for the opposite facet of the waveguide. The aluminium layer-thickness was monitored with a crystal oscillator during evaporation and the final layer thickness verified using a Talystep.

The reflectivity of the thin aluminium film was calculated by measuring the reduction in transmittance at normal incidence, in a microscope slide of known refractive index, coated at the same time. The transmittance in an uncoated area was used as a reference. The derivation of the expressions used for this purpose are in Appendix A. It is assumed that the aluminium films are lossless.

Results were obtained for only one sample, due in part to the lack of time available. Figure 7.34 tabulates the data used and figure 7.35 shows the oscillations obtained.

Aluminium Thickness /nm	Measured Reflectivity*	Tabulated Reflectivity†
(a) 12.5	90.0	83.0
(b) 25.0	90.1	90.0

Figure 7.34 Reflectivity data, (a) input facet, (b) output facet

\* through both films together, † see figure 7.37, appendix A

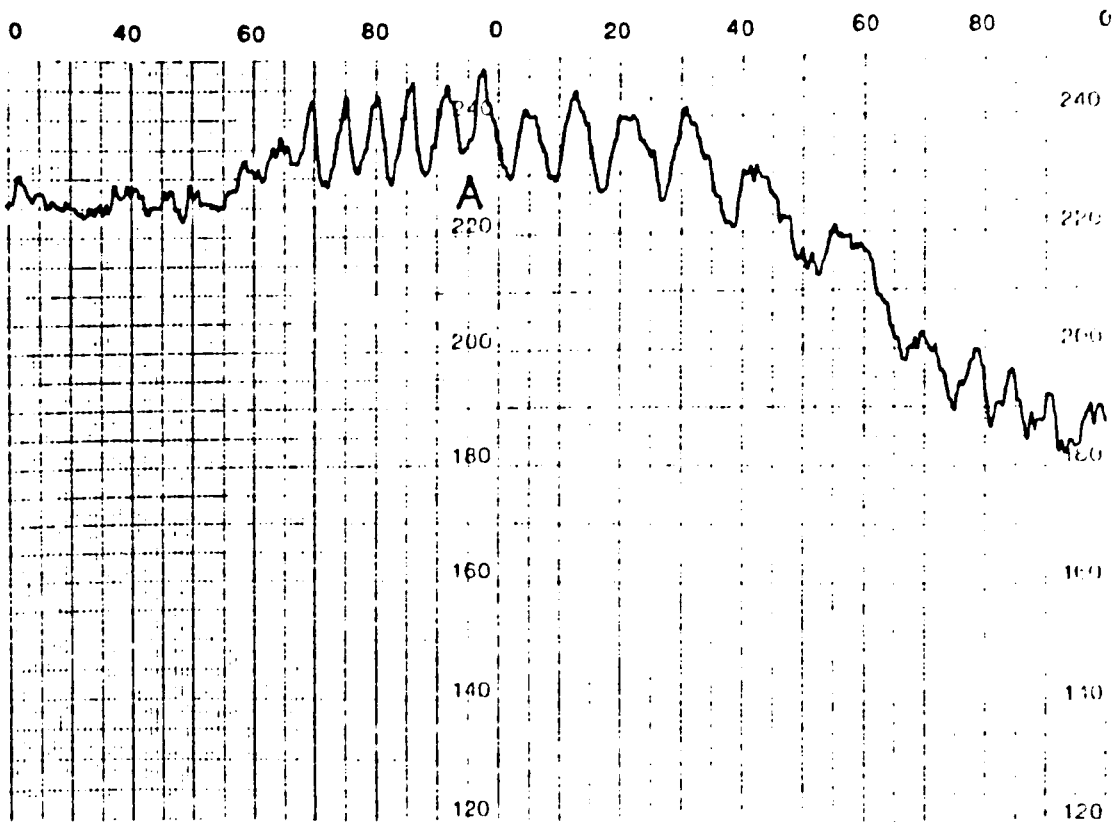


Figure 7.35 Observed oscillations

Average values for the maximum and minimum observed intensities,  $I_{max}$  and  $I_{min}$  of 256.4 and 238.4 (arbitrary units), calculated from 5 successive oscillations in region A are used in the loss calculation. Using the value of reflectivity from figure 7.34 with the above data substituted into the expression for loss on section 7.4.2 (1), a loss figure of  $-16.986$  dB was obtained. The sample length was 1.8 cm and hence the loss is 9.44 dB/cm.

#### 7.4.2 (5) DISCUSSION OF RESULTS

It is instructive to consider sources of error arising from this technique and to assess, if possible, their contribution to the loss.

As already discussed (section 7.4.2 (2)), non-parallel facets can contribute significantly to waveguide loss. With that in mind, the facet angles were measured.

The facet angles on the waveguide in question were measured using a Nikon microscope with a micrometer objective incorporating a travelling cross-hair arrangement. The samples were placed on the rotating support stage of the microscope, and the cross-hairs used as guides for the measurements.

Measurement No	Angle measured	
	Facet A	Facet B
1	12'	1° 36'
2	28'	1° 12'
3	18'	1° 18'
4	18'	1° 12'
Average	19'	1° 19'

Figure 7.36 Values of facet angles

The large facet angle of  $>1^\circ$  will result in a decay of more than 50% of the reflected power. This will obviously contribute significantly to the waveguide loss. Furthermore, it is difficult to estimate how much this will contribute to the loss in dB since the calculations of section 7.4.2(2) do not fully explain the experimental results of other workers<sup>16</sup>.

Other possible sources of error include absorption in the aluminium facets and sample movement during heating. Such effects can be reduced by careful experimentation - ie, more sensitive measurements of reflection coefficients to obtain the loss due to the aluminium and bonding of the sample to the sample holder to stop any movement during heating.

## 7.5 CONCLUSIONS

The method of ridge waveguide fabrication has been outlined and results of such fabrication presented. Etch quality can be improved by careful selection of etch gases and conditions. The structures produced have been assessed in terms of: etch quality, using SEM analysis; etch depth, using talystep measurements and optical loss.

The techniques for the assessment of optical loss are two-fold:- (1) Video Camera Technique, and (2) Fabry-Perot Cavity Technique. Both techniques are non-destructive. The results from both techniques were felt to be susceptible to systematic errors and the results should be interpreted with care

However, the results from section 6.4.3 demonstrated that the planar films had very little out-of-plane scattering which in turn suggests a low loss waveguide, furthermore good quality silica films should have very low absorption loss. This

then suggests that the loss encountered in the waveguides is introduced during the processing stages required to form the ridge waveguide structure and is likely to arise from wall roughness introduced during etching.

It is not possible at this stage to quote a loss figure in the ridge waveguide structures with any degree of confidence. Both techniques tried have inherent problems which affect the measured optical loss.

## 7.6 APPENDIX A Calculation of Reflectance of Aluminium Films

If  $I_g$  and  $I_{Al}$  are the transmitted intensities through the uncoated and coated areas of the glass microscope slide respectively, then:—

$$\frac{T_g}{T_{Al}} = \frac{I_g}{I_{Al}}$$

— since the transmittances are in the same ratio as the transmitted intensities.

But:—

$$T_g = (1 - R_g)$$

and:—

$$R_g = \left[ \frac{n - 1}{n + 1} \right]^2$$

— where  $n$  is the refractive index and  $R_g$  is the reflectance of the microscope slide

Hence:—

$$T_{Al} = \frac{I_{Al}}{I_g} \left[ 1 - \left[ \frac{n - 1}{n + 1} \right]^2 \right]$$

The reflectance of the aluminium coated film is therefore:—

$$R_{Al} = T_{Al} - 1$$

The value of reflectance obtained by measurement using the above expression was checked against values calculated using a program called Filmstar by FTG Software Inc. (courtesy of Dr. I. Reid, BTRL ). Reflectance, and transmittance values for varying film thickness are included in Figure 7.37.

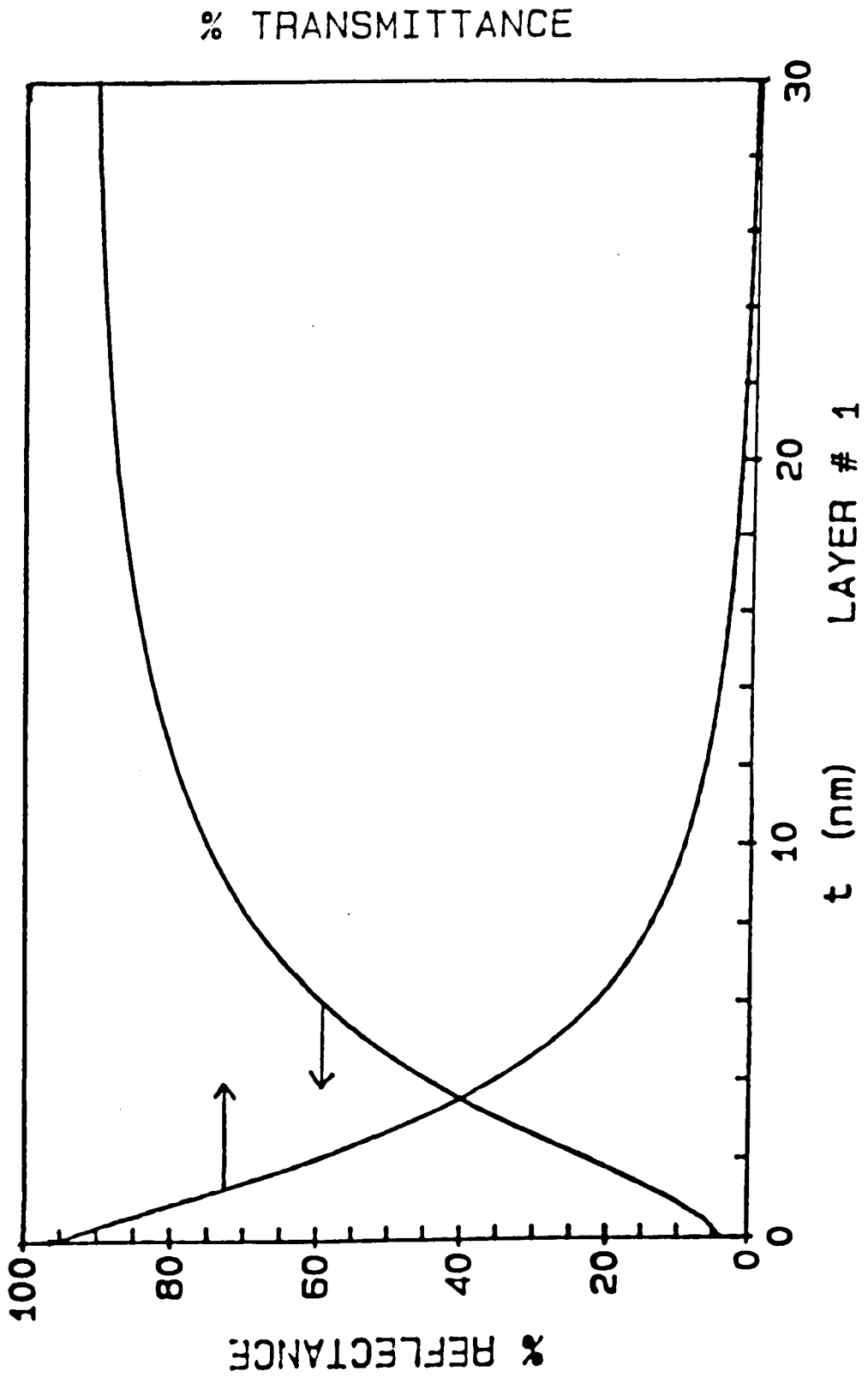


Figure 7.37 Reflectance and transmittance of thin Aluminium films

## 7.7 REFERENCES

1. H. KOGELNIK  
Integrated Optics, Ed. T. Tamir, p63  
Theory of dielectric waveguides
2. E.A.J. MARCATILI  
Bell System Tech. J., April 1974, pp645- 674  
Slab- coupled waveguides
3. J.K. BUTLER, C.S. WANG, J.C. CAMBELL  
J. Appl. Phys., Vol 47, No.9, Sept. 1976, pp4033- 4043  
Modal characteristics of optical stripline waveguides
4. S.M. SZE  
VLSI Technology
5. L.M. EPHRATH  
J. Electrochem. Soc.:Reveiws & News, Vol. 129, No. 3, 1982, pp62C- 66C  
Dry etching for VLSI- A reveiw
6. C. STEINBRUCHEL, H. W. LEHMANN, K. FRICK  
J. Electrochem. Soc.: Solid State Sci. & Tech., Vol. 132, No.1, Jan. 1985,  
pp180-186  
Mechanism of dry etching of silicon dioxide
7. J.M. MORAN, D. MAYDAN  
Bell Syst. Tech. J., May- June 1979, Vol. 58, No.5, pp1027-1036  
High Resolution, Steep Profile, Resist Patterns
8. R. G. HUNSPERGER  
Integrated Optics : Theory and Technology, p89
9. T. TAMIR  
Integrated Optics: Ed. T. Tamir  
Beam and Waveguide couplers
- 10.Y. OKAMURA, S. YOSHINAKA, S. YAMAMOTO  
Appl. Opt., Vol. 22, No. 23, 1st Dec. 1983, pp3892- 3894  
Measuring mode propagation losses of integrated optical waveguides:  
A Simple Method
- 11.F.A. JENKINS, H.E. WHITE  
Fundamentals of Optics, McGraw- Hill
- 12.R. ROGENER, W. SOHLER  
Appl. Phys. B., Vol. 36, pp 143-147,, 1985  
Loss in low- finesse Ti:LiNbO<sub>3</sub> Optical Waveguide Resonators
- 13.R. G. WALKER  
Electr. Lett., 20th June 1985, Vol. 21, No. 13, pp581- 583

Simple and accurate loss measurement technique for semiconductor optical waveguides

**14.D. MARCUSE**

J. Lightwave Tech., Vol. 7, No. 2, Feb. 1989, pp336– 339

Reflection loss of Laser Mode From Tilted End Mirror

**15.H. A. MACLEOD**

Optics of Thin Films, 2nd Ed. 1986

**16.KADHAIR AL-HEMYARI, C. WILKINSON**

Private Communication

This final chapter details extensions to the film deposition technique allowing the incorporation of rare-earth materials into the glass. The method adopted for such doping is described and the results presented. Applications for such films are outlined and work carried out on one such application – a silica based distributed feedback laser (DFB) is discussed. Also included in this chapter are the results from work involving second harmonic generation (SHG) in  $\text{GeO}_2/\text{P}_2\text{O}_5$  co-doped silica films.

The chapter will be divided into three broad sections; one, detailing the rare-earth doping and assessment; one discussing grating design and fabrication; and the third, detailing basic theory involved in, and experimental results of Second Harmonic Generation, (SHG) in planar waveguides.

### 8.1    DOPING OF PLANAR SILICA FILMS

Doping techniques for silica can be classed in two broad categories depending on the vapour pressure of the dopant species – namely those with moderate to high vapour pressures (such as  $\text{GeCl}_4$ ,  $\text{TiCl}_4$ ) and those with low vapour pressures (such as  $\text{NdCl}_3$ ,  $\text{ErCl}_3$ ).

The materials falling into the first category, can be readily incorporated into the standard vapour delivery systems in CVD processes, such being the case for the materials used to fabricate passive waveguides.

Low vapour pressure materials, such as the rare-earth compounds, require alternative vapour delivery techniques or even alternative doping methods altogether. Two such methods are:–

- (1) the use of a secondary burner or heater to heat a source of suitable dopant to a level where it has a significant vapour pressure and can be transported in a similar manner to other standard dopant species<sup>1,2</sup>. Sintering can occur in situ or can take place in a separate stage
- (2) the use of solution doping<sup>3</sup>, whereby a partially fused sample or preform is immersed in a solution containing the desired dopant; dried to remove the solvent, and then fully sintered

Of the two techniques, it is the second which has been used by the author because of its simplicity and because absorption and fluorescence results are available from measurements made on fibres using the same technique<sup>4,5</sup> which are useful for comparison.

The technique involves partially fusing the deposited silica film to produce a rigid skeleton. This was achieved by heating the samples at approximately 1000°C for 5 minutes.

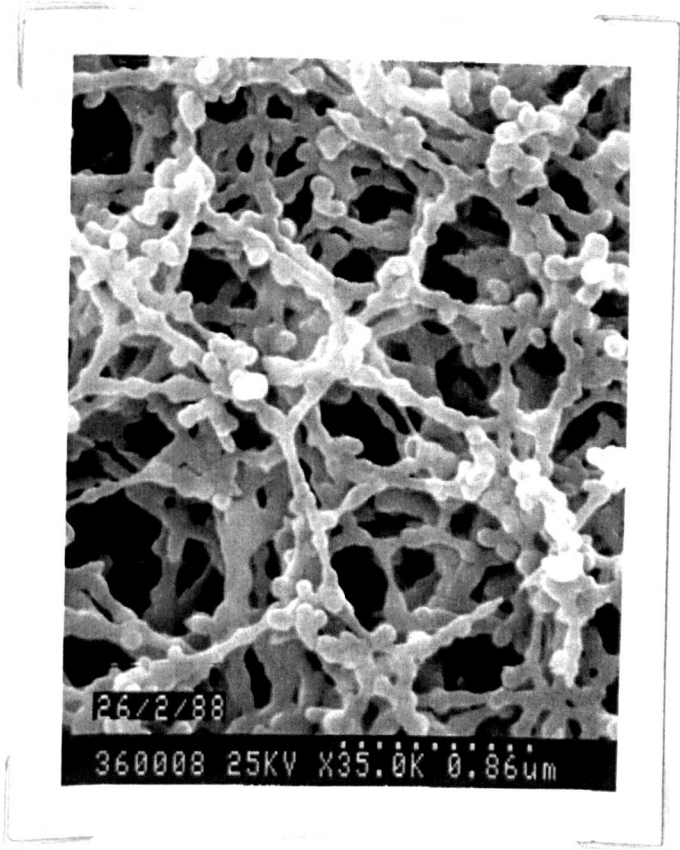


Figure 8.1 SEM picture of partially fused rigid skeleton

This structure is now sufficiently strong to withstand the capillary forces introduced when the sample is immersed in a suitable doping solution and subsequently dried<sup>6</sup>. The doping solution in this case consists of a decomposable rare-earth salt in a suitable solvent. Two rare-earth materials were used Neodymium chloride,  $\text{NdCl}_3$  and Erbium chloride,  $\text{ErCl}_3$ , dissolved in pure ethanol. Both rare-earth ions exhibit fluorescence at wavelengths of potential interest for telecommunications. Co-doping of rare-earth material with Aluminium nitrate,  $\text{Al}(\text{NO}_3)_3$ , was also attempted since improvements in fluorescence bandwidth have been reported<sup>7</sup>.

### 8.1.1 DOPING METHOD AND RESULTS

The doping method used involves immersing the sample into the rare-earth solution. This was then covered with a beaker to reduce evaporative loss of the solvent. The solution was poured off after typically five minutes and the sample gently blown dry.

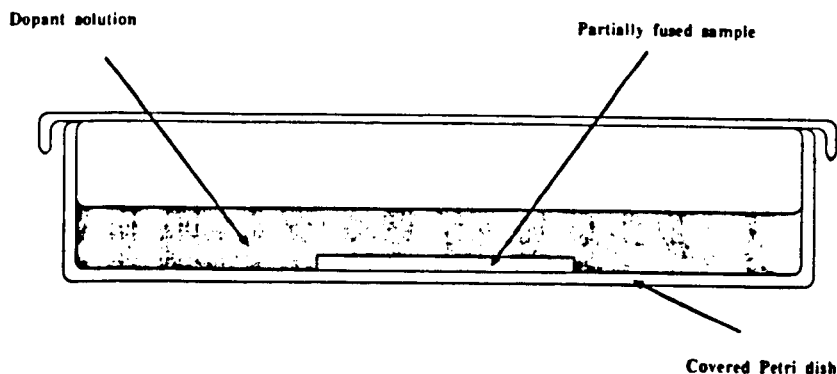


Figure 8.2 Schematic of doping method

The dried sample was then ready for the second sintering stage – heating to around 1300 °C for typically 60 minutes.

All samples for solution doping were prepared in the same way. The deposition consisted of two layers with flow rates of nitrogen through the bubblers of  $\text{SiCl}_4$  150 sccm's, and  $\text{PCl}_3$  160 sccm's. Initial fusing was carried out at 1000 °C for five minutes.

These rare-earth doped samples were all single mode at  $\lambda = 632.8$  nm and the layer thickness was estimated to be approximately  $2\mu\text{m}$  (from figure 5.13)

Batch	Dopant & Concentration/M		Fusing details		Film Quality
			Temp /°C	Time /mins	
89	ErCl <sub>3</sub>	0.02	1300	60	Slight blue tint
		0.01	1300	60	Clear
		0.005	1300	60	Clear
86	NdCl <sub>3</sub>	0.02	1300	60	Blue tint
		0.01	1300	60	Blue tint
		0.005	1300	60	Clear
90	Al(NO <sub>3</sub> ) <sub>3</sub>	0.02	1300	60	Unfused
		0.01	1300	60	Unfused

Figure 8.3 Summary of doping experiments

Standard photolithography and etching were carried out (section 7.2.2) to produce ridge waveguides. These samples were cut and polished to facilitate measurements in the waveguides using end-fire launching, (figure 8.4). The results of luminescence measurements obtained are given in figures 8.5 and 8.6.

The pump wavelength of 514.4 nm (5W peak power) being incident on the surface of the waveguide and the fluorescence measured from the output facet of the waveguide. Typical waveguide dimensions were  $50\mu\text{m}$  wide by  $2.5\mu\text{m}$  deep and 25 mm long.

The same samples were then analysed using EDAX to assess the doping levels of the rare-earth materials, (see figure 8.7).

Comparisons of these luminescence results, in terms of fluorescence peak positions with similar work in optical fibres, agree well with the peak positions in medium to high P<sub>2</sub>O<sub>5</sub> doped hosts for Neodymium, and for GeO<sub>2</sub> - P<sub>2</sub>O<sub>5</sub> - SiO<sub>2</sub> doped fibres<sup>5</sup> for Erbium. Data from the fibre results will be used in 8.1.2 to calculate the expected absorption from such dopants. It is this absorption which will determine whether or not practical devices are feasible.

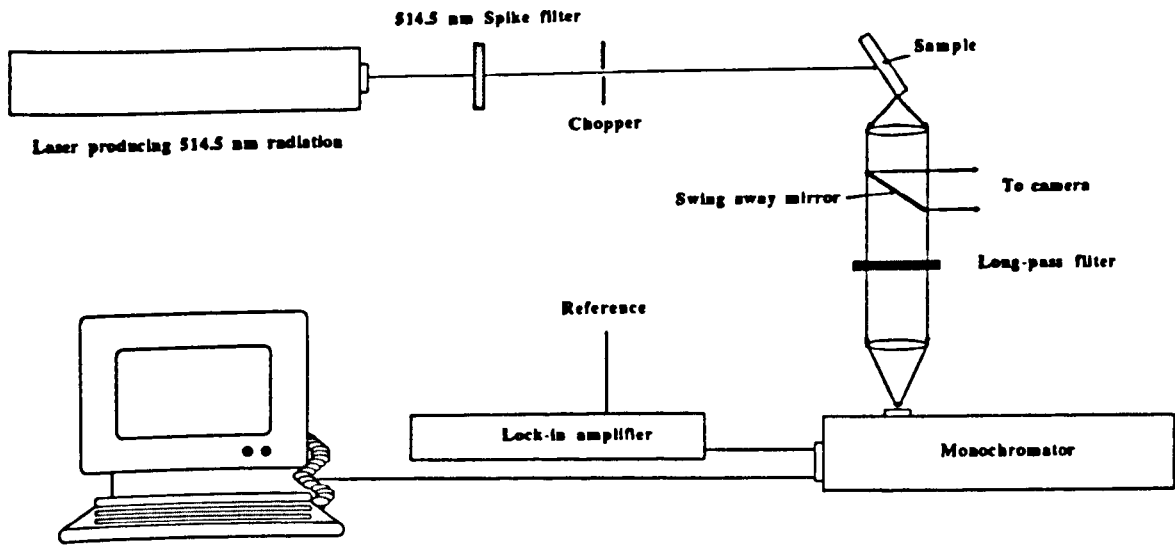


Figure 8.4 Schematic of Luminescence measurement facility

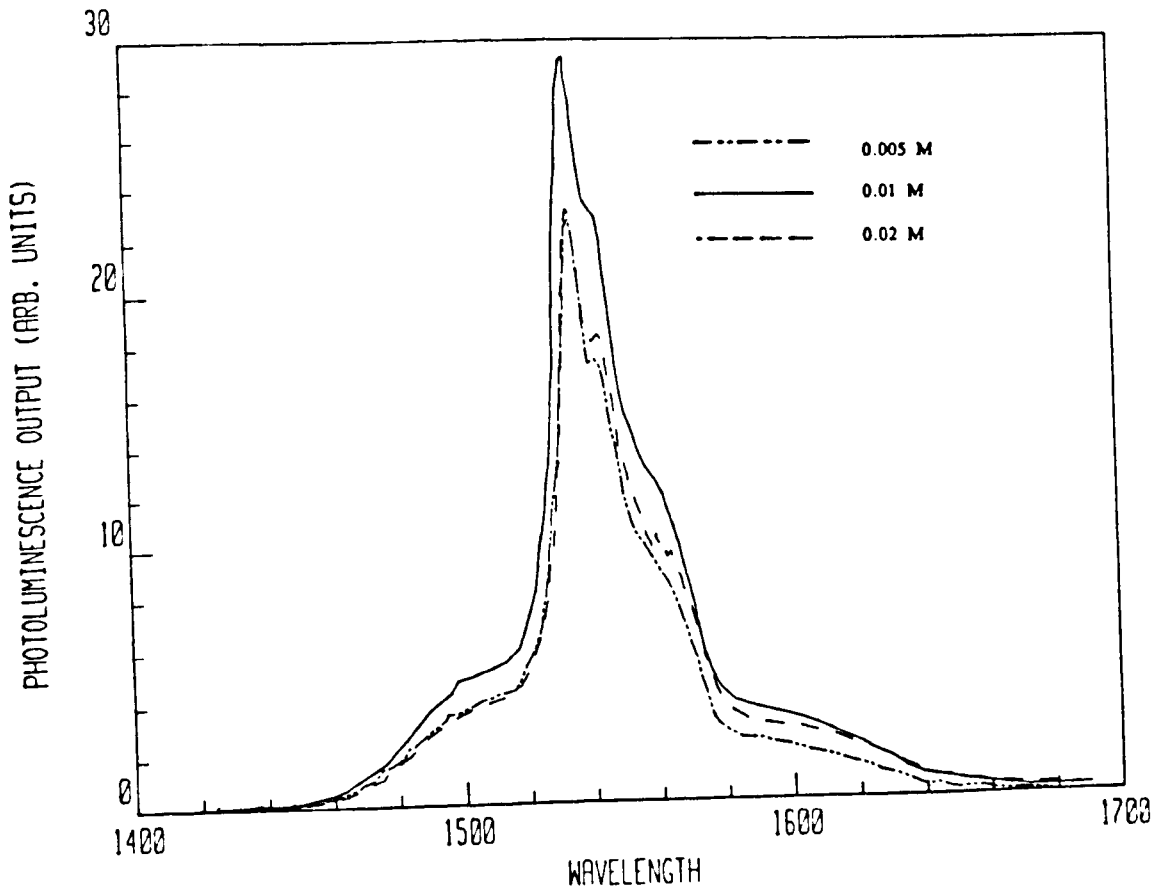


Figure 8.5 Luminescence Spectra of Er<sup>3+</sup> doped planar silica ridge waveguide

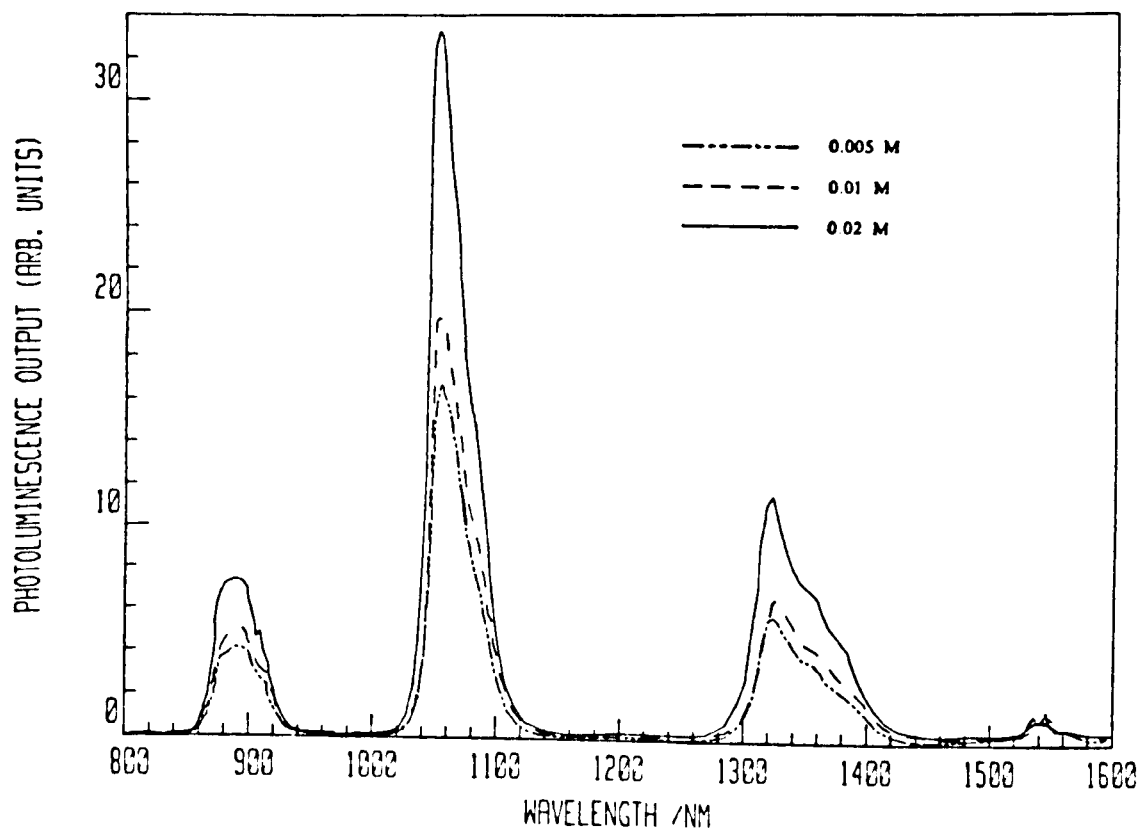


Figure 8.6 Luminescence Spectra of  $\text{Nd}^{3+}$  doped planar silica ridge waveguide

Dopant & Concentration /M	Doping level		
	In Waveguide /wt%	Between Waveguides /wt%	
$\text{ErCl}_3$	0.02	0.80	0.24
	0.01	0.37	0.07
	0.005	0.16	0.04
$\text{NdCl}_3$	0.02	0.40	0.10
	0.01	0.70	0.18
	0.005	0.36	0.09

Figure 8.7 EDAX measurements on rare-earth doped waveguides

### 8.1.2 DISCUSSION OF RESULTS

When considering the results from the EDAX measurements, it must be borne in mind that the measurements are local, in the sense that an average value is taken from a local area illuminated by the electron-beam. Hence any doping variations occurring across the sample (possibly arising from uneven pore closure during initial sintering) will not be detected if the variation is on a scale that is larger than the spot size of the illuminating electron beam.

This may possibly account for the result of the 0.02m Nd<sup>3+</sup> doped sample which does not follow the expected trend of increasing doping level with increasing concentration of doping solution.

If we turn our attention to the photoluminescence results we see the expected trend in the output intensities of the observed spectra for Nd<sup>3+</sup>. In this measurement, the pump wavelength of 514.4 nm generates luminescence over much greater distances inside the waveguide than the spot size of the electron beam used in the EDAX measurement. As such it gives a non-local average value for luminescence which would iron out any local doping variations.

Having said that, we observe in the Erbium doped samples a different result, namely the expected trend in doping levels but not in luminescence. This runs counter to the arguments already developed and its cause is as yet unclear.

With the results of the doping levels in figure 8.7, and the absorption data from reference 5, we can calculate the expected single pass absorption from the expression:-

$$\alpha = E(\lambda)xy$$

where  $\alpha$  is the absorption (dB),  $E(\lambda)$  is the extinction coefficient at the chosen pump wavelength (dB/cm/wt%)  $x$ , is the doping level in wt%, and  $y$  is the sample length in cm. Keeping in mind that in fibres the attenuation is much lower and the path lengths much larger, but the material is intrinsically the same.

Figure 8.8 details the results of such a calculation for various pump wavelengths using a value of 0.5 wt% as a typical doping level and 5 cm as a typical device length.

Dopant	Pump Wavelength/nm	Extinction Coeff. /dBcm <sup>-1</sup> wt%- <sup>-1</sup>	Absorption /dB
Er <sup>3+</sup>	650	2.17	5.425
	980	2.30	5.75
	1480*	1.50	3.75
Nd <sup>3+</sup>	750	3.20	8.00
	810	5.00	12.50

Figure 8.8 Expected absorption in rare-earth doped silica

\* See reference 8.

For such devices to be of use, the gain produced must be greater than the scatter loss of the waveguide – the absorption losses are negligible since absorption is bleached in a three level system. If one had a quantum efficiency of one – which is the case for low Er<sup>3+</sup> doped fibres<sup>5</sup>, then the possible gain equals the absorption. This then sets an upper limit on the waveguide loss which can be tolerated before such devices become impractical for laser applications. As a sample calculation if we assumed a figure of 0.5 dB/cm waveguide loss, then in 5 cm, the loss would be 2.5 dB and the absorption would exceed the loss and gain would be obtained at all of the pump wavelengths highlighted above.

## 8.2 HOLOGRAPHIC GRATING FABRICATION

Producing waveguiding films containing rare earth materials is only one of the steps involved in fabricating a planar ridge waveguide laser. Also required is a means of providing the necessary feedback in such a structure for lasing to take place. Such feedback could be provided using external mirrors<sup>9</sup>, or mirrors butted to the ends of the waveguides or direct coating of the waveguide end facets. However such a structures would be sensitive to vibration and misalignment, in the cases of external or butted mirrors. Alternatively a diffraction grating etched into the waveguide could provide a stable and vibration insensitive feedback mechanism, when acting as a Bragg reflector, as well as providing narrow linewidth operation of the laser. Such a distributed feedback (DFB) laser<sup>10</sup> would be compact and

inherently rugged.

It was with this application in mind that grating structures were fabricated using a holographic technique<sup>11</sup>. As well as providing the necessary feedback, such gratings could be used as reverse couplers to launch the pump wavelength into the waveguide. The fabrication of such structures was carried out on passive waveguides and the gratings used as reverse couplers, thereby outlining the necessary processing stages required in their fabrication.

### 8.2.1 GRATING COUPLERS – BASIC THEORY

In a grating coupler, an input beam is incident on a diffraction grating formed on a waveguide and one of the diffraction orders of the grating is used to couple light into a particular mode of the waveguide. The angle of incidence of the input beam is tuned until the diffracted beam has the same phase velocity in the waveguide as the mode itself. See figures 8.9 and 8.10.

The basic theory outlined here describes the derivation of the phase relations necessary for the operation of grating couplers and follows the method of Dalgoutte and Wilkinson<sup>12</sup>. No analysis has been carried out on grating efficiency.

From figure 8.10, it is clear that the condition for phase matching, and hence coupling will be achieved when

$$K - \beta = k_a \sin \theta_a \quad \text{or} \quad k_s \sin \theta_s$$

Therefore, with a knowledge of the values of  $K$ , and  $k_a$ , the value of  $\theta$  required for coupling can be calculated and checked by experiment.

i.e. 
$$\theta_a = \sin^{-1} ((\lambda_0/\Lambda) - n_{\text{eff}})$$

– where  $\lambda_0$  is the free space wavelength and  $\Lambda$  the grating period.

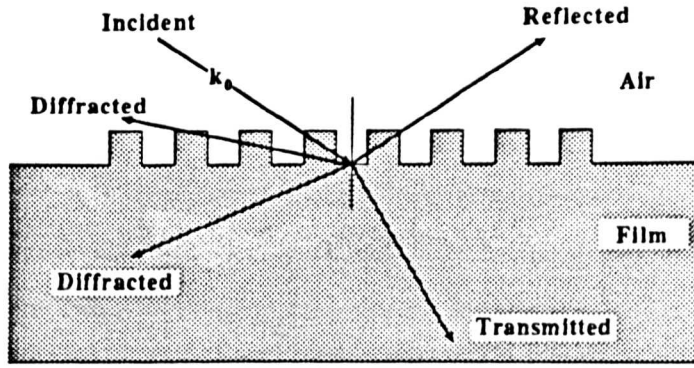
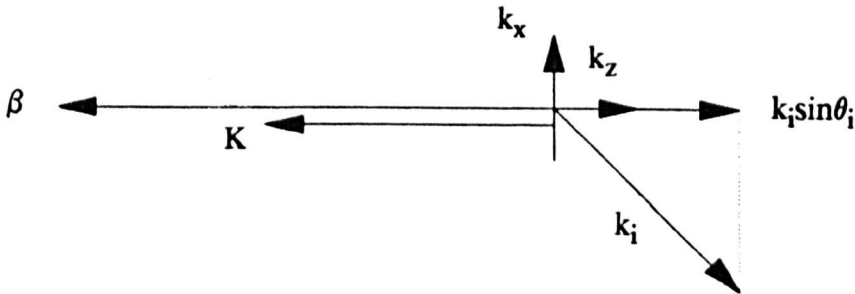


Figure 8.9 Schematic of Grating Coupler Operation

Wavevector diagram for a reverse coupler



Conservation of momentum in the waveguide yields:-

$$K - \beta = k_i \sin \theta_i$$

Figure 8.10 Vector diagram for grating coupler

## 8.2.2 FABRICATION OF GRATING COUPLERS

The procedure adopted to fabricate the diffraction gratings consisted of typically six main steps:-

- (1) Light from an Ar<sup>+</sup> laser ( $\lambda = 457.9\text{nm}$ ) was split, and recombined after passing through beam expanders and spatial filters, to produce interference fringes on the surface of photoresist spun on to the waveguide. These fringes then exposed the resist. The fringe spacing was determined by the angle of incidence of the interfering beams on the sample surface, (in this case the angle was  $50^\circ$ ). Stray

reflections and standing waves were avoided by bonding the sample with index matching oil to a glass wedge the back faces of which had been painted matt black.

- (2) The resist was developed to give a low contrast grating in photoresist
- (3) The samples were then placed in an evaporator at an angle and a NiCr mask was deposited on the peaks of the grating
- (4) An oxygen plasma etch was used to strip away the uncoated photoresist, thus producing a high contrast grating
- (5) The silica waveguide was then etched in  $\text{CHF}_3$  using the same process as has already been outlined.
- (6) Finally the mask was removed to leave the grating structure etched in the waveguide.

The only deviation from the above procedure which was attempted involved using a thinner layer of photoresist, which was exposed and developed through to the surface of the waveguide. No metal overlay or  $\text{O}_2$  etch was required and the resist was used as the mask for the  $\text{CHF}_3$  etch. Figure 8.11 schematically depicts the process steps involved. Typical results are detailed in figures 8.12 and 8.13

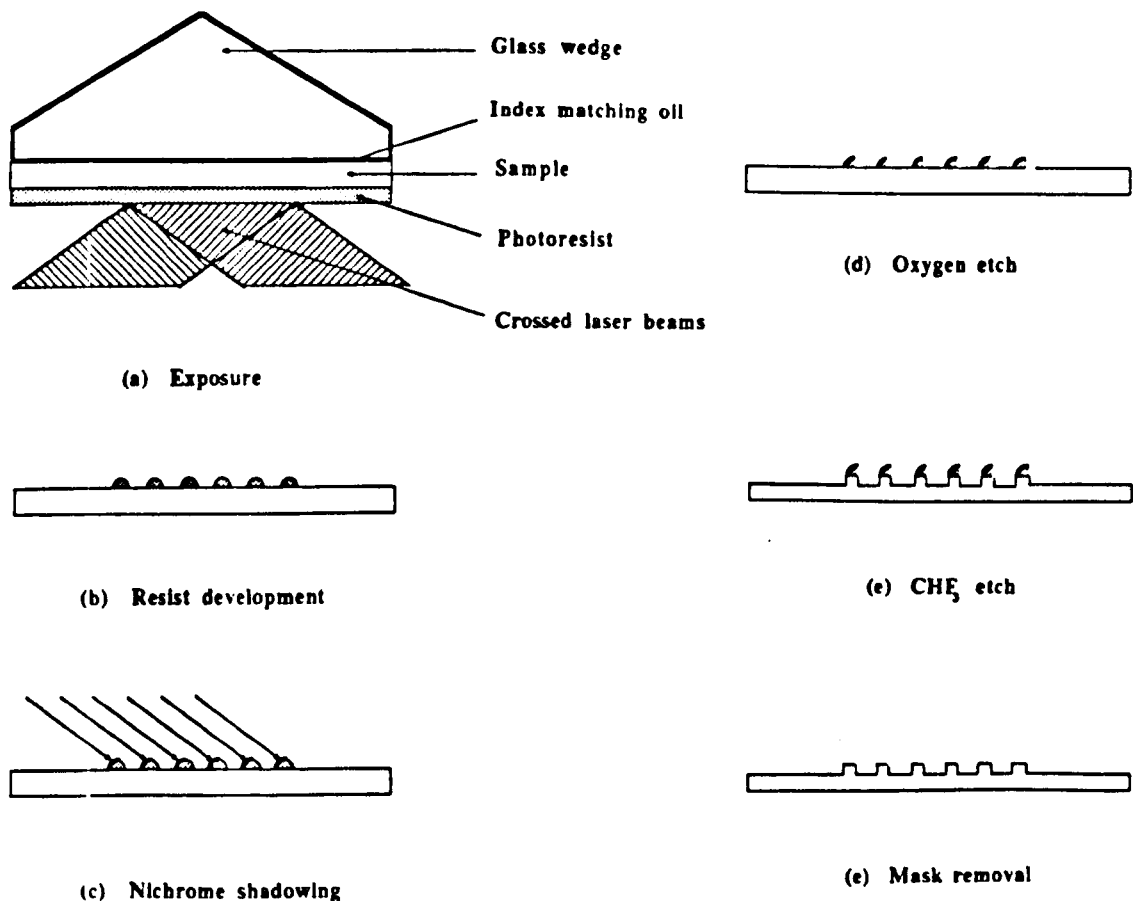


Figure 8.11 Schematic of process stages in grating fabrication

Sample no.	Resist Details			Exposure Time /s	Developing Time /s
	*Resist ratio	Spin speed /rpm	Spin time /s		
53	100	4000	30	45	40
83	100	4000	30	45	20
78	100	4000	30	45	20
93	66	5000	30	40	18
52	25	5000	30	†40	12

Figure 8.12 Details of grating mask fabrication

\* the percentage refers to the ratio of Shipley 1450J resist to thinner used

† no NiCr mask was used in this case

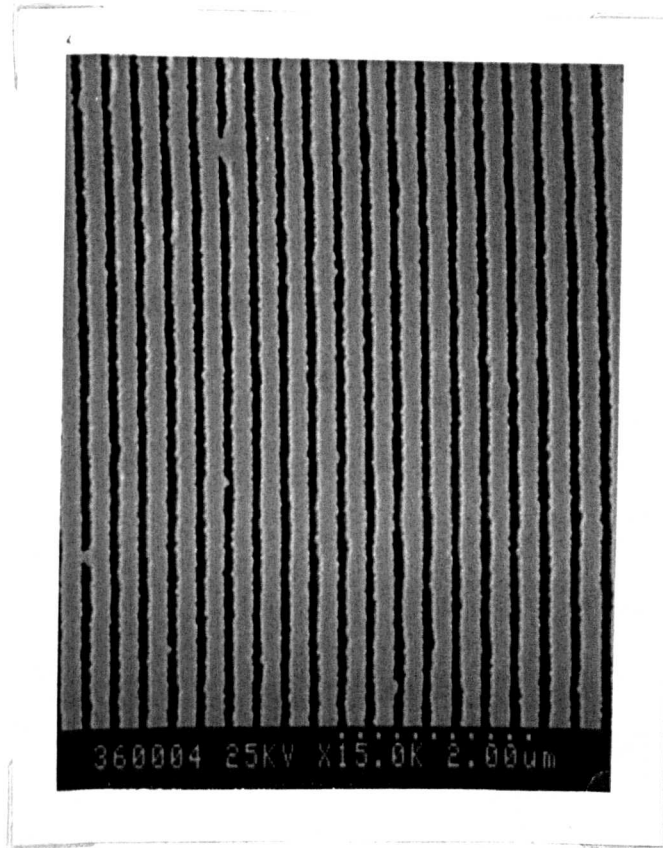
Sample no.	Etch details				
	Plasma gas	Etch pressure /mr	Forward power /W	Flow rate /sccm	Etch time /mins
53	O <sub>2</sub>	21.3	50	20	15
	CHF <sub>3</sub>	20.8	100	15	5
83	O <sub>2</sub>	15.9	50	10	15
	CHF <sub>3</sub>	19.5	100	15	5
78	O <sub>2</sub>	21.4	50	20	15
	CHF <sub>3</sub>	19.5	100	15	10
93	O <sub>2</sub>	12.8	50	20	7
	CHF <sub>3</sub>	13.8	100	35	10
52	O <sub>2</sub>	12.0	50	20	7
	CHF <sub>3</sub>	20.8	100	42	5

Figure 8.13 Etching parameters used in grating fabrication

### 8.2.3 ASSESSMENT OF GRATINGS

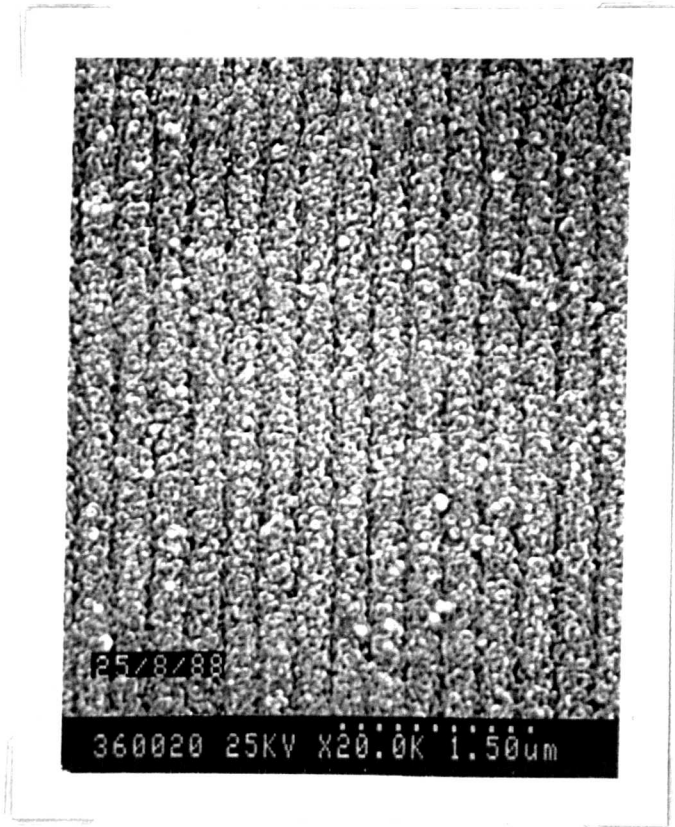
Grating assessment was carried out primarily by direct observation of the etched gratings using the SEM. Coupling of light into the waveguide was then carried out on samples with suitable gratings. Figure 8.14 shows SEM photographs of the resulting etched structures.

In the coupling experiments, laser light was incident on the grating and the sample rotated. When phase matching was achieved, light was launched in the reverse direction to the input beam, and a bright stripe was visible. The angles of incidence were measured for each mode coupled into. Using the values of  $\theta$ ,  $\Lambda$ , and  $\lambda_0$ , the values of  $n_{\text{eff}}$  could be calculated and checked against those measured with the prism coupler. Figure 8.15 details the results of the coupling experiments.

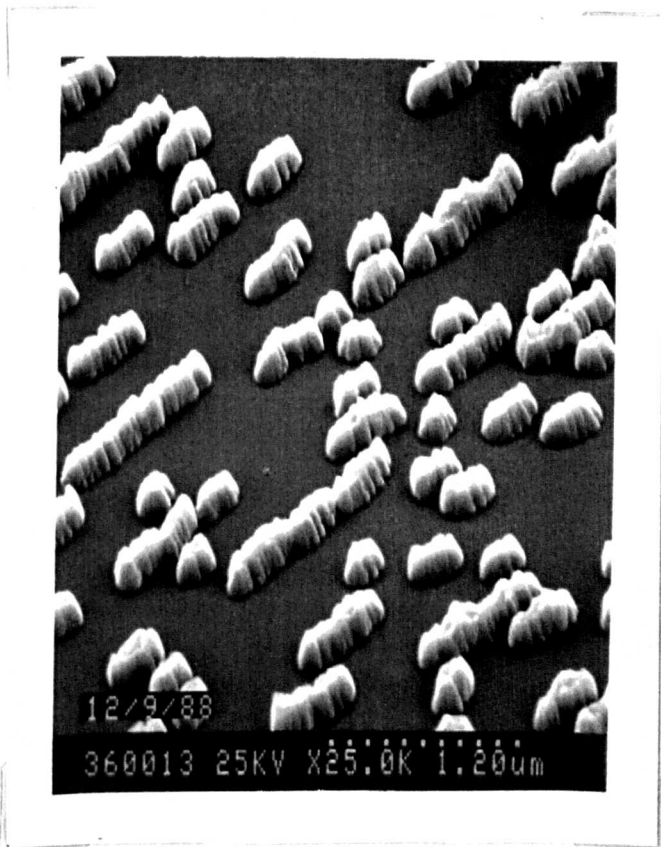


(a) Good

Figure 8.14 SEM photos of etch quality — the good, the not-so-good and the interesting but totally useless.



(b) Not-so-good



(c) Interesting but totally useless

Figure 8.14 SEM photos of etch quality — the good, the not-so-good and the interesting but totally useless.

Sample no.	Coupling	$\lambda_0$	$\Lambda$	$n_{eff}$	$n_{eff}$
	Angles				
	/°	/nm	/nm	from grating	coupling
53	41.16	632.8	298.8	1.4596	1.472
	40.57			1.4674	1.479
52	41.34	632.8	298.8	1.4572	1.469
	40.61			1.4668	1.479

Figure 8.15 Details of coupling experiments

Writing wavelength = 457.9, angle of  
incidence of writing beams = 50°

The values of effective index calculated from the grating coupler measurements are in reasonable agreement with those obtained from the prism coupling when one keeps in mind the inaccuracies already discussed in the prism coupling measurements.

### 8.3 SECOND HARMONIC GENERATION (SHG) IN $\text{GeO}_2/\text{P}_2\text{O}_5$ WAVEGUIDES

Second Harmonic Generation aroused considerable interest when it was first observed in optical fibres<sup>13</sup>, such a process having hitherto been considered impossible in such centro-symmetric materials. Since the waveguides fabricated by the author are compositionally the same as the optical fibres in which the phenomenon was observed, it was considered sensible to attempt similar experiments to ascertain whether SHG could be observed in such planar ridge structures. To that end an experiment was performed in which high intensity infra-red radiation 'seeded' with its second harmonic was passed through the waveguide.

The results of that experiment<sup>14</sup> are presented in the following section together with a phenomenological description of the theories involved in the process as are currently understood.

### 8.3.1 PHENOMENOLOGICAL MODEL OF SHG IN DOPED SILICA

In order to understand the phenomenon of Second Harmonic Generation (SHG), it is necessary to consider the polarization response of a material to applied electric fields. In most materials with modest field intensities, the induced polarization response is linear, (see Figure 8.16(a)). That is to say:—

$$P = \epsilon_0 \chi E$$

— where  $\chi$  is the dielectric susceptibility of the material,  $\epsilon_0$  is the dielectric permittivity and  $E$  is the applied electric field, which may be static or time varying.

However, if the material is subject to much higher field intensities, then the polarization response may become non-linear. Such is the case for the polarization responses depicted in figure 8.16 (b) and (c). The polarization may then be expressed as a power series which includes higher order terms,

$$P = \epsilon_0 \{ \chi^{(1)}E + \chi^{(2)}E^2 + \chi^{(3)}E^3 + \dots \}$$

If we apply a time varying field to such a non-linear material then the time varying response of the polarization is found to contain frequency components not present in the original applied electric field. Thus, higher frequency components have been generated.

Consider figure 8.16 (b). Here we have a *centro-symmetric* material in which the deviation of polarization from that of a linear response is the same for a given amplitude of applied electric field of both positive and negative sign. If we analyse the polarization response for an applied field  $E(\omega)$ , in terms of its Fourier components, it is found to contain terms in  $\omega, 3\omega, 5\omega$  and higher odd components as well as a d.c. offset. It does not contain terms in  $2\omega$  or other even orders. As such, SHG would not be expected from such a material. Silica glass falls into this category of material.

The non centro-symmetric material schematically represented in figure 8.16 (c) has a different value of polarization for a given amplitude of electric field depending on sign. The Fourier components of  $P(\omega)$  in this case contains frequency components of both even and odd orders, and one would therefore expect second harmonic generation in such materials.

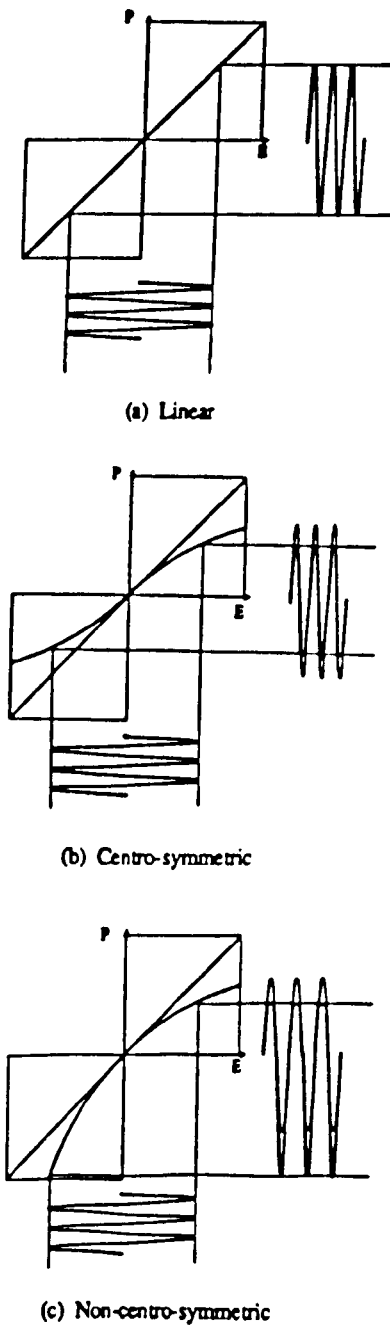


Figure 8.16 Polarisation responses of linear and non-linear materials to an applied oscillating field

Second Harmonic Generation is however observable in silica, arising from other sources<sup>15,16</sup> including the presence of interfaces, (e.g. between core and cladding in fibres where symmetry is broken), electric quadrupole and magnetic dipole effects. The levels of second harmonic signal arising from such sources are very small<sup>17</sup> and would not in themselves account for the observed experimental results. It is however felt that such weak signals may play a part in the process.

There are two models postulated to explain the observed phenomenon of SHG in optical fibres. One, considers the effect as arising from the formation of colour

or defect centres<sup>18</sup>, the other<sup>19</sup> describes the effect in terms of an internal static d.c. field which alternates in sign and poles the material.

In both cases the end result is the breakdown of symmetry in the material which then results in the formation of an internal grating structure providing the necessary phase matching for efficient SHG.

In the first model<sup>20</sup> the weak second harmonic signal arising from electric quadrupole and magnetic dipole effects *and* the high intensity infra-red pump wavelength form a periodic intensity pattern along the waveguide with a coherence length  $\Lambda_c$ . This excites the colour centres or defects in the material, forming dipoles and thus breaking the material symmetry and giving rise to an enhanced second order non-linear susceptibility  $\chi^{(2)}$ . This provides automatic phase matching, since the excitation will occur at the points where the second harmonic intensity is greatest which occurs when the pump and second harmonic signal are in phase, leading to a grating structure whose period is equal to the coherence length,  $\Lambda_c$ .

In the second model<sup>21</sup> the pump wavelength mixes with the second harmonic signal via an allowed third order process involving  $\chi^{(3)}$ . This gives rise to a d.c. field with a periodically alternating sign, which orientates defect centres within the material. With this defect orientation comes the breakdown in material symmetry and the growth of a periodic  $\chi^{(2)}$ , having the same period as the alternating d.c. field. This process once again provides the necessary phase matching automatically.

The exact nature of the defects which are aligned or excited in the material is not clear, although it is believed to involve the germanium dopant used in the waveguide fabrication<sup>21</sup>.

## 8.3.2 METHOD AND RESULTS OF SHG IN PLANAR RIDGE WAVEGUIDES.

### 8.3.2.(1) WAVEGUIDE FABRICATION

Ridge waveguides were fabricated using the processes outlined in chapters 5,6 and 7, and involved a standard deposition using halide flow rates and fusing conditions as outlined in figure 8.2.

Halide	Flow rates	Fusing Temp. /°C	Fusing time /mins
SiCl <sub>4</sub>	150	1270	85
PCl <sub>3</sub>	160		
GeCl <sub>4</sub>	60		

Figure 8.17 Summary of conditions of film fabrication

The film index was measured using the prism coupler procedure as outlined earlier and was found to be 1.477. This compares reasonably well with the value of index expected from doping level considerations.

Standard photolithographic and etching techniques as outlined in chapter 7 were used to fabricate the ridge waveguides. These consisted of a series of 1 to 5  $\mu\text{m}$  wide lines with an etch depth of 2.2  $\mu\text{m}$ . Figure 8.18 shows the resulting etch quality of one of the waveguides.

### 8.3.2(2) EXPERIMENTAL ARRANGEMENT FOR SHG

The experimental arrangement used in the SHG experiments is detailed in figure 8.19. It consists of a Nd<sup>3+</sup>:YAG laser operating in a Q-switched mode delivering 150 ns pulses at 1.06 microns. This pulse is passed through a series of optical elements consisting of a polariser, focussing lenses at each side of a KDP frequency doubling crystal, a half-wave plate and a second polariser to allow rotation of the plane of polarisation. This light was then end-fire launched into the waveguide, the sample having been previously bonded to a 1" thick glass block to prevent local thermal effects. The output was then passed through a beam rejection mirror to remove the pump wavelength. The green light could be viewed through a four-port telescope to observe the mode pattern. A calibrated photomultiplier tube was used to collect the output signal which was subsequently displayed on an oscilloscope.

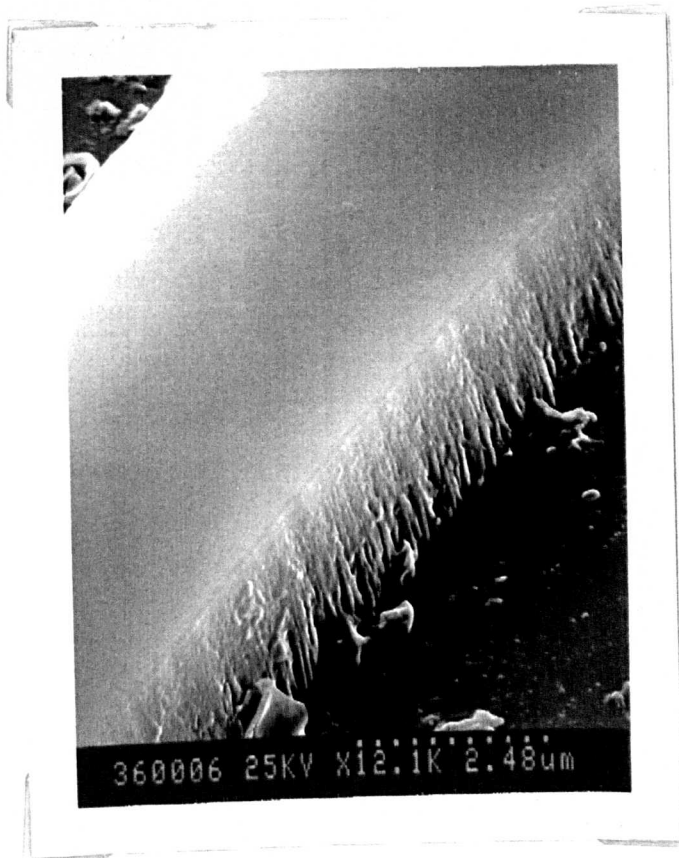


Figure 8.18 SEM photograph of etch quality  
156

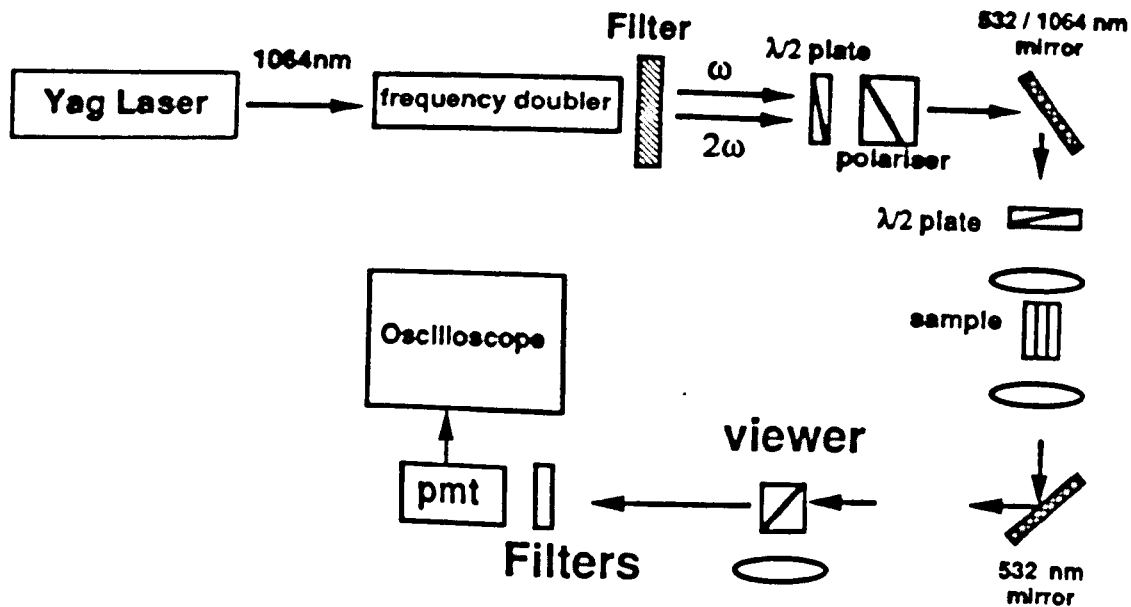


Figure 8.19 Experimental Arrangement used for SHG

### 8.3.2(3) EXPERIMENTAL RESULTS

Two experiments were performed on the sample. They were:-

- (1) Unseeded SHG, and
- (2) Seeded SHG

In the first experiment, 25mW of pump power (2kW peak power) was launched into the waveguide. A weak second harmonic signal was observed, which

amounted to 240nW, and appeared to be in the TE<sub>10</sub> mode, although confirmation was difficult due to the low signal levels. The second harmonic signal level was monitored over a period of an hour, but no signal increase was observed.

The second experiment entailed 'seeding' the waveguide using 0.532 $\mu$ m light generated from a KDP frequency doubling crystal placed at the focii of two objective lenses in the path of the IR pump beam. Problems were encountered both with crystal deterioration and efficient launching of both wavelengths into the waveguide. However a compromise solution was achieved whereby 65mW of the second harmonic seed was launched simultaneously with 80mW of 1.064 $\mu$ m pump. These power levels were maintained for the hour long seeding experiment. After this time, the seed wavelength was removed and the generated second harmonic signal measured. This was found to have increased to 32 $\mu$ W for an output power of 20mW pump, (1.33kW peak). The pump power was then varied and the generated green signal power levels were measured. See figure 8.20.

Experiment	Av. Pump Power /mW	Av. SHG Power / $\mu$ W
Unseeded	25	0.24
Seeded	2	0.26
	3.2	0.53
	4.7	1.07
	13.4	10.69
	19.2	26.73
	20	32.85

Figure 8.20 Measured power levels of SHG.

Measurements of the second harmonic signal using higher pump powers had to be curtailed due to the catastrophic failure of the waveguide itself. The damaged area extended over approximately 0.8mm of waveguide which is much greater than the wavelength of light used, and is believed to be due to self-propelled self-focussing damage<sup>22</sup> encountered in optical fibres. Figure 8.21 illustrates a plot of the results obtained, and figure 8.22 shows the damage sustained by the waveguide for higher pump powers.

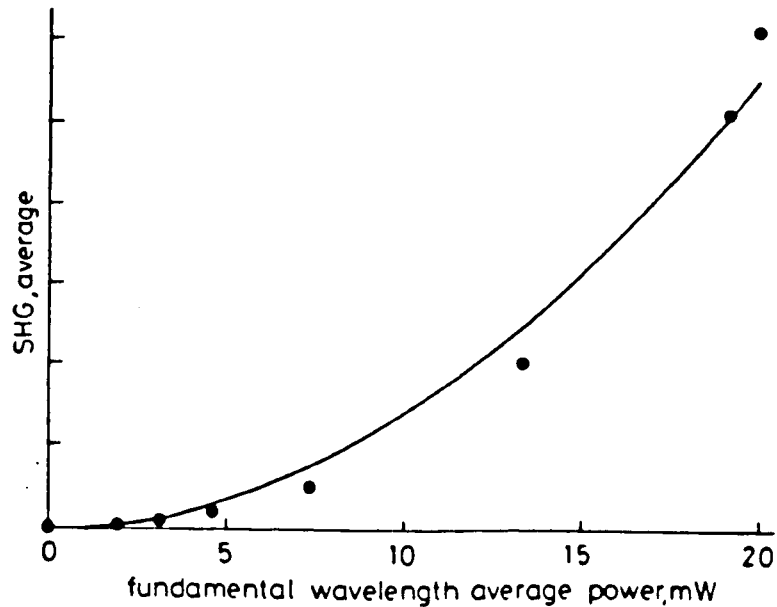


Figure 8.21 Plot of SH power versus input power

#### 8.3.2(4) DISCUSSION OF RESULTS

The results of the previous section indicate that second harmonic generation is possible in silica structures other than optical fibres. Since the material is the same in both cases, it is not unreasonable to suppose that the same mechanism is responsible for the SHG observed. The possible mechanisms have already been outlined and involve the optical writing of a grating structure of some form within the waveguide.

Further experiments are required to ascertain whether or not improvements in SHG efficiency are possible. Such experiments could take the form of looking at the effects of doping levels as well as the effect of greater seeding times. Moreover it may be worthwhile to use clad waveguides in such experiments as this may allow the use of higher pump powers. A further area of interest would be to look at the effect on optical loss of 'writing' such grating structures since the mechanism appears to involve the generation of defects in the glass structure which are known to increase attenuation<sup>23</sup>.

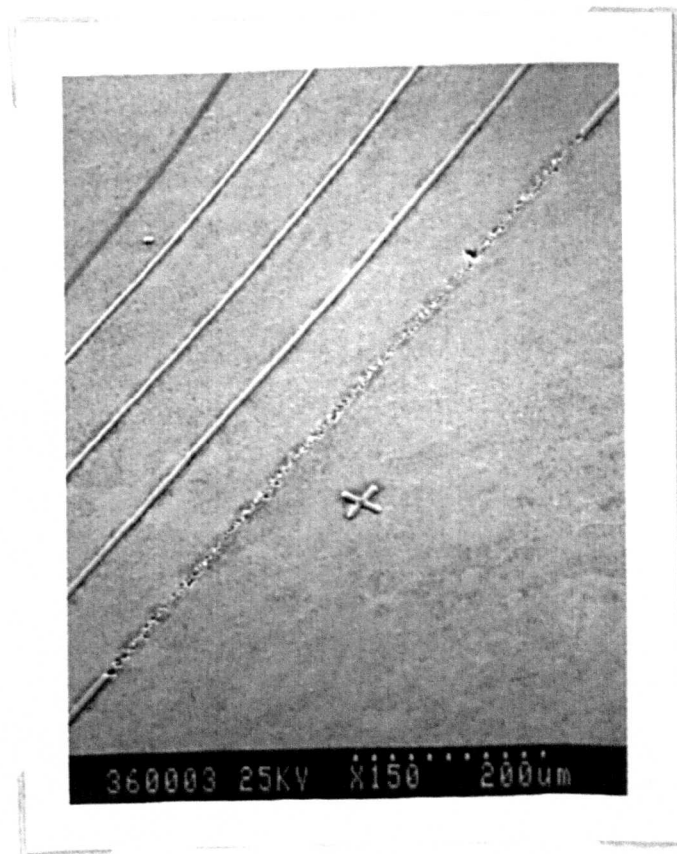


Figure 8.22 SEM photo illustrating waveguide damage

## 8.4 REFERENCES

1. S.B. POOLE, D.N. PAYNE, M.E.FERMANN  
Electronics Lett., Vol. 21, No.17, pp737-738, 15th Aug. 1985  
Fabrication of low-loss optical fibres containing rare-earth ions
2. H. NAMIKAWA, K. ARAI, K. KUMATA, Y. ISHII, H. TANAKA  
Jap. J. Appl. Phys., Vol. 21, No. 6, June 1982, ppL360-L362  
Preparation of Nd-doped silica glass by plasma torch CVD
3. J. STONE, C.A. BURRUS  
Appl. Phys. Lett., Vol. 23, No. 7, 1st Oct. 1973, pp388-389  
Neodymium doped silica lasers in end pumped fiber geometry
4. R. J. MEARS, L. REEKIE, S.B. POOLE, D.N. PAYNE  
Electr. Lett., Vol. 21, No. 17, 15th Aug. 1985, pp738-740  
Neodymium doped silica single mode fibre lasers
5. B.J. AINSLIE, S.P. CRAIG, S.T. DAVEY  
J. Lightwave Tech., Vol. 6, No.2, Feb. 1988, pp287-292  
The Absorption and Fluorescence spectra of Rare-Earth Ions In Silica Based Monomode fibre
6. J. ZARZYCKI, M. PRASSAS, J. PHALIPPOU  
J. Mat. Sci., Vol. 17, 1982, pp3371-3379  
Synthesis of glasses from gels: the problem of monolithic gels
7. K. ARAI, H. NAMIKAWA, K. KUMATA, T. HONDA, Y. ISHII, T. HANDA  
J. Appl. Phys., Vol.59, No.10, 15th May 1986, pp3430-3436  
Aluminium or phosphorus co-doping effects on the fluorescence and structural properties of neodymium doped silica glass.
8. Y. KIMURA, K. SUZUKI, M. NAKAZAWA  
Electr. Lett., Vol. 25, No. 24, 23rd Nov. 1989, Vol.25, No. 24, pp1656-1657
9. L. REEKIE, R.J. MEARS, S.B. POOLE, D.N. PAYNE  
J. Lightwave Tech., Vol. LT-4, No. 7, July 1986, pp956-960  
Tunable single-mode fibre lasers
10. J.E. BJORKHOLM & C.V. SHANK  
IEEE J. Quant. Elect., Vol. QE-8, No. 11, Nov. 1972, pp833-838  
Distributed-feedback lasers in thin-film optical waveguides
11. A. YI-YAN, J.A.H. WILKINSON, C.D.W. WILKINSON  
IEE Proc., Vol. 127, Pt. H, No. 6, Dec. 1980 pp335-341  
Optical waveguide filters for the visible spectrum
12. D.G. DALGOUTTE, & C.D.W. WILKINSON  
Appl. Opt., Vol. 14, No. 12, Dec. 1975, pp2983-2997  
Thin grating couplers for integrated optics: An experimental and theoretical study

13. U. OSTERBERG, W. MARGULIS  
 Digest of the XIV Int. Quant. Elect. Conf., Opt. Soc. Am., Washington DC,  
 paper WBB2, p102, 1986
14. R. KASHYAP, B.J. AINSLIE, G.D. MAXWELL  
 Electr. Lett., Vol.25, No.3, 2nd Feb. 1989, pp206-208  
 Second Harmonic Generation In GeO<sub>2</sub> Ridge Waveguides
15. R.W. TERHUNE, D.A. WEINBERGER  
 J. Op. Soc. Am. B, Vol. 4, No.5, May 1987, pp661-674  
 Second harmonic generation in fibres
16. V. MIZRAHI, J.E. SIPE  
 J. Op. Soc. Am. B, Vol. 5, March 1988, pp660-667  
 Phenomenological treatment of surface second harmonic generation
17. F.P. PAYNE  
 Electronics Lett., 5th Nov. 1987, Vol.23, No. 23  
 Second Harmonic Generation In Single-mode Optical Fibres
18. M. C. FARRIES, P. St. J. RUSSELL, M.E. FERMANN, D.N. PAYNE  
 Electronics Lett., 26th Mar. 1987, Vol. 23, No.7  
 Second Harmonic Generation In an Optical Fibre By Self-written  $\chi^{(2)}$  grating
19. R. H. STOLEN, H.W.K. TOM  
 Opt. Lett., Aug. 1987, Vol. 12, No. 8  
 Self-organised phase-matched harmonic generation in optical fibres
20. R.H. STOLEN  
 NATO ASI, Nonlinear waves in Solid State Physics, Summer School, Erice  
 July 1st - 15th 1989  
 Second Harmonic Generation In Optical Fibres
21. T.E. TSAI, M.A. SAIFI, E.J. FRIEBELE, D.L. GRISCOM, U. OSTERBERG  
 Opt. Lett., Vol. 14, No.18, Sept. 15th 1989, pp1023-1025  
 Correlation of defect centres with second harmonic generation in Ge-doped and  
 Ge-P doped silica-core single mode fibres.
22. R. KASHYAP, K.J. BLOW  
 Electr. Lett., Vol. 24, No. 1, 1988, pp47-49  
 Observation of Catastrophic Self-Propelled Self-focussing In Optical Fibres
23. M.C. FARRIES, M.E. FERMANN, P. St. J. RUSSELL  
 IGWO 1989, Vol. 2, Feb. 6-8, Houston, Texas  
 Second Harmonic Generation in Optical Fibres

## CHAPTER 9 CONCLUSIONS AND FUTURE WORK

This chapter gives a general conclusion to the work carried out for this thesis and describes a number of areas which in the author's opinion would merit further research.

Conclusions have been included at the end of most of the earlier chapters. However a broad conclusion is included here for completeness.

With regard to future work, the areas are broadly split into two categories: one concerns work on material aspects, the other on waveguiding or optical aspects. Some areas have been suggested in the relevant chapters.

### 9.1 CONCLUSIONS

This thesis has described a method for fabricating doped silica waveguides using Flame Hydrolysis deposition. Dopants used include  $P_2O_5$ , to lower the required sintering temperature and  $GeO_2$  or  $TiO_2$  to raise the refractive index of the material. Doping levels have been measured using Energy Dispersive Analysis with X-rays (EDAX). Prism coupling has been carried out on the planar films, and no out-of-plane scatter has been observed.

Ridge waveguides have been fabricated using photolithography and Reactive Ion Etching. The loss of these waveguides has been assessed using a scanning video camera technique, and also by a Fabry-Perot technique.

Such ridge waveguides have also been doped with Neodymium and Erbium and fluorescence has been obtained for both species from these waveguides.

Holographic gratings have been fabricated with a view to their incorporation as feedback elements in a laser structure.

Second Harmonic Generation (SHG) has been observed *for the first time* in ridge waveguides in Germanium and Phosphorus doped silica.

### 9.2 MATERIAL ASPECTS FOR FUTURE WORK

The areas for future work will be suggested as a series of questions which it is hoped will stimulate their investigation.

More in depth analysis on chemical structure/ composition of deposited soot would be useful in an attempt to answer the following:—

Q/ Are the dopant oxides, e.g.  $P_2O_5$ ,  $GeO_2$ ,  $TiO_2$  chemically bonded to the silica particles during deposition ?

This will be important when depositing a buffer layer at the same time as a waveguide, since one would then expect some diffusion of the dopant species. Interestingly enough, in the  $TiO_2$  waveguides fabricated with a buffer layer, the observed mode lines were not equally spaced, suggesting a graded index profile, which in turn would suggest species diffusion.

If this is the case, then it leads to the question of at what point are the dopants bonded to the network? This then leads to two areas of interest:-

Q/ Can the dopant oxides be lost by evaporation during sintering ?

Q/ Which sintering scheme is most suitable ? That is, a ramped temperature profile, or isothermal sintering ?

Answers to these questions will then become more important when one wished to dope rare-earth materials into the partially fused films. As was pointed out in chapter 8, the solubility of rare-earth material can be improved by co-doping with  $P_2O_5$ . If this dopant is not chemically bonded to the silica after the partial fusing stage, then the solution used to dissolve the rare-earth material may also dissolve away some of the dopant. This could limit the doping levels of rare-earths obtained.

### 9.3 OPTICAL ASPECTS FOR FUTURE STUDY

By far the most important area for further optical work is the measurement of the optical loss in both planar and ridge waveguides. The technique ideally should be quick and non-destructive. This requirement becomes more important when one is dealing with rare-earth doped waveguides, since after assessing the loss, one would then wish to continue with further experiments on the waveguide. This is why the cut-back method is less appealing.

Once one has addressed this problem, one can answer questions like:-

Q/ How does the doping level of rare-earth effect the loss?

Q/ At what point does this loss become prohibitive for laser/ amplifier applications ?

With answers to these questions, one can then optimise designs for lasers and amplifiers.

The other optically interesting area would be in the area of Second Harmonic Generation and the study of the non-linear behaviour of the doped silica. Immediate areas of interest can involve answering questions like:-

Q/ What is the maximum level of SHG possible from such small structures?

Q/ What is the loss induced with such structures?

Q/ What effect does the doping level have on SHG levels?

Such areas could quite easily be addressed with the film fabrication facility constructed by the author.

There are obviously a number of areas not mentioned here, suitable for further study, and it is hoped that the reader of this thesis will have his or her own ideas on the subject.